CRANFIELD UNIVERSITY

JAIME POLO BERMEJO

A Very High Resolution X- and Ku-band Field Study of a Barley Crop in Support of the SWINTOL Project

Cranfield Defence and Security
November 2015

MSc
Academic Year: 2014 - 2015

Supervisor: Keith Morrison
November 2015

CRANFIELD UNIVERSITY

Cranfield Defence and Security

MSc

Academic Year 2014 - 2015

JAIME POLO BERMEJO

A Very High Resolution X- and Ku-band Field Study of a Barley Crop in Support of the SWINTOL Project

Supervisor: Keith Morrison
November 2015

This thesis is submitted in partial fulfilment of the requirements for the degree of Master of Science by Research

ABSTRACT

SAR Wave INteraction for Natural Targets Over Land (SWINTOL) is a project funded by the European Space Agency. The study's goal is to better understand the interaction of high frequency radar (> X-band) with vegetation and soils, in order to drive the development of a high-frequency electromagnetic model to simulate SAR imagery at high resolution (< 1 m). Existing models work well at C and X band frequencies, but do not work properly at higher frequencies.

Cranfield University's role in this project was to provide the field data necessary for model validation and development. Radar imagery was taken of a barley crop over an entire growing season. The portable outdoor GB-SAR system used the tomographic profiling (TP) technique to capture polarimetric imagery of the crop. TP is a scheme that provides detailed maps of the vertical backscatter pattern through a crop canopy, along a narrow transect directly beneath the radar platform.

Fully-polarimetric imagery was obtained across overlapping 6.5 GHz bandwidths over the X- and Ku-band frequency range 8-20 GHz. This gave the opportunity to see the detailed scattering behaviour within the crop at the plant component level, from emergence of the crop through to harvesting. In combination with the imagery, full bio-geophysical characterisation of the crop and soil was made on each measurement date. Surface roughness characterisation of the soil was captured using a 3D optical stereoscopic system.

This work details the measurements made, and provides a comparative assessment of the results in terms of understanding the backscatter in relation to biophysical and radar parameters.

Keywords:

Synthetic Aperture Radar, SAR, tomographic Profiling, tomography, X-band, Ku-band, barley, soil moisture.

ACKNOWLEDGEMENTS

I am grateful to everyone that helped me during this period.

TABLE OF CONTENTS

LIST OF FIGURES

LIST OF TABLES

LIST OF EQUATIONS

LIST OF ABBREVIATIONS

ESA	European Space Agency
SAR	Synthetic Aperture Radar
InSAR	Interferometric Synthetic Aperture Radar
TP	Tomographic Profiling
SWINTOL	SAR Wave Interaction for Natural Targets over Land
GB-SAR	Ground Based SAR
VNA	Vector Network Analyzer
CW	Continuous Waveform
CCD	Change Coherent Detection
δ	Range resolution of a real antenna
δ_r	Range resolution of a SAR
δ_{cr}	Cross-range resolution of a SAR
B	Bandwidth
c	Velocity of propagation of the signal
λ	Wavelength
R	Range or distance
Θ_B	Beamwidth of a real antenna
Θ_S	Beamwidth of a SAR
L_e	Effective length aperture
L_{max}	Maximum length aperture
DEM	Digital Elevation Model
DLR	German Aerospace Center
JAXA	Japan Aerospace Exploration Agency
ONERA	Office National d'Etudes et de Recherches Aérospatiales
ASI	Agenzia Spaziale Italiana
MDA	MacDonald Dettwiler Associates Ltd. of Richmond
RF	Radio Frequency
SfM	Structure from Motion

1 INTRODUCTION

At high spatial resolution (i.e. <1 m) and/or for short wavelengths (i.e. < 3 cm) there is still a gap in the understanding and the interpretation of SAR backscatter of vegetation and soils. The existing models are insufficient to address high resolution and short wavelength interaction over land surfaces [1]. By increasing the frequency and resolution, it is hoped new information and knowledge may be also extracted to provide a better understanding and characterisation of the targets.

The development of an electromagnetic model at higher frequencies will be beneficial for the study of the radar images taken from aircraft and satellites, allowing us to obtain a better knowledge from radar images in forest, crop and vegetation areas. This model will help to extract important environmental parameters such as crop state, height, biomass, stress, health, yield prediction, soil moisture and so on.

For the first time, simultaneous sets of high frequency X and Ku band imagery 8-20 GHz radar data was acquired in the field of crops and soils covering the complete growing season of crops, from its emergence through the senescence. In addition to the radar measurements, crop samples were collected and measured in order to perform a study of its characteristics to provide reliable data. The data acquired is presented, analysed and studied in this work.

To accomplish this task, a Consortium between Cranfield University, ONERA and NOVELTIS was set up. Each company has a team with expertise in the field and a specific task has been designated according to their knowledge as shown in the Figure 1-1. NOVELTIS also oversaw management of the project. A close collaboration between the members of the Consortium is necessary for the success of the project.
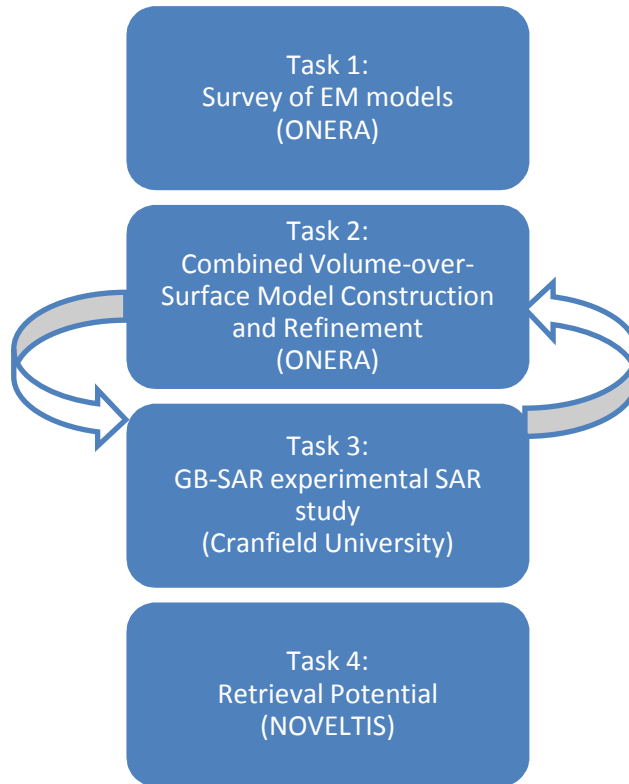
Figure 1-1: Planning of the SWINTOL project.

Cranfield University was in charge of the acquisition of field data and its analysis with the microwave measurement facilities explained in chapter 7 [2]. Outdoor measurements at different bandwidths, polarizations, and imaging geometries were performed.

2 Radar-Target interaction

In this chapter, a basic explanation about how the radar wave interacts with different scene targets depending on their characteristics is presented with emphasis in the interaction of the signals over natural geophysical targets like vegetation and soils. A radar system is an active system; that means that a signal is generated by the radar in order to interact with the target, and depending on the properties of this target (roughness, moisture, or shape) a certain backscattered signal will be returned to the radar system [3].

The radar sends out a signal from the antenna with a certain amplitude, polarization, wavelength, phase, bandwidth, which arrives at the target at a certain incidence angle. Some backscattered signal will come back in the same direction of the radar and it will be measured, and this signal has suffered modification indicative of the interaction between the radar wave and the target. It is important to notice that by measuring the travel time of the signal, the distance between the radar and the target can be known.

The parameters of the signal returned will depend on the size, orientation and the distribution of scattering surfaces, the roughness, the dielectric constant or the orientation of the target. As shown in the Figure 2-1, the roughness of the surface governs the scattering pattern of the signal. When the signal from the radar hits a smooth surface, like water, the signal usually gets scattered in a single forward direction and just a small part of it is returned to the radar.
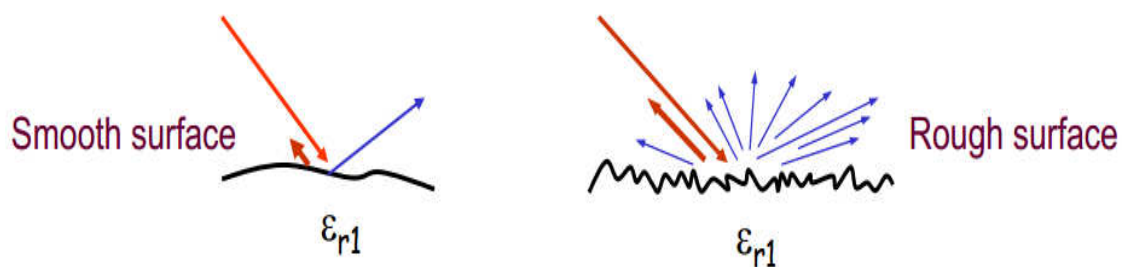
Figure 2-1: Interaction of the signal depending on the roughness of the surface.

When the same signal encounter a rough surface with the same dielectric constant, the signal is scattered in random multiple directions depending on the roughness and a backscattered signal with bigger amplitude than in the previous case is returned to the radar.

The dielectric constant of the medium, which for vegetation and soils is strongly dependent on the moisture content, governs the strength of the backscatter. With the same scenario, if the dielectric constant of a material is changed the signal scattered is going to change its amplitude. Note the difference between the Figure 2-1 and the Figure 2-2, where for a larger dielectric constant but the

same surface roughness, the signal backscattered to the radar (red) is bigger than before.
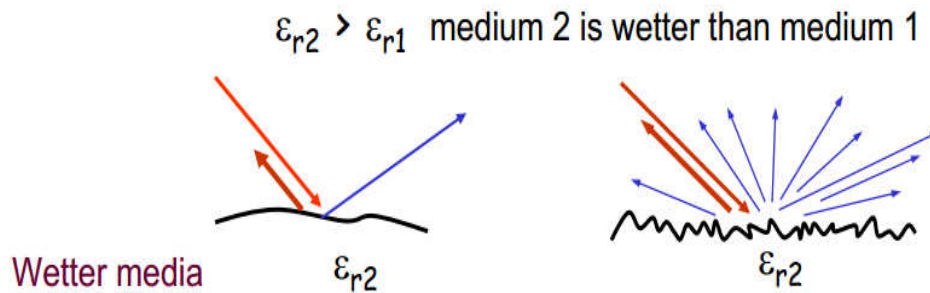
Figure 2-2: Interaction of the signal depending on the roughness of the surface and the dielectric constant.

Another important parameter to take into the account is the polarization of the signal. Every electromagnetic signal has a certain polarization; the most common polarizations are vertical linear (V) and horizontal linear (H).

The radar antennas are designed electrically and mechanically to transmit and receive electromagnetic waves of a specific polarization. Over a vegetation area, there can be depolarization of the incident wave. When a signal is sent to a certain scenario, the measured signal with an antenna with vertical polarization is different than the measured signal with a horizontal antenna due the different target features (leaves, branches, trunks and so on). The geometry of these obstacles scatters the signal in different directions creating different paths for the signal during its flight and changing the polarization of the signal as is explained later in this chapter. The Table 2-1 summarizes the different configurations that are commonly used in radar systems.

Denomination	Transmit polarization	Receive polarization
HH	Horizontal	Horizontal
VV	Vertical	Vertical
HV	Horizontal	Vertical
VH	Vertical	Horizontal

Table 2-1: Different polarization configurations with antennas in a radar system.

When an electromagnetic signals moves from a medium of a given dielectric properties, i.e. air, into another one with different dielectric properties, i.e. water, one part of the signal is reflected and other part is refracted. When the surface of the medium is smooth, there is no change of polarization in the signal. But when some roughness is present on the surface some depolarization occurs. Due the structure of the vegetation and the different paths that the signal can take due the geometry and the numerous elements on it (leaves, branches, trunks, stems, etc), depolarization is likely to occur in the signal [3].

Figure 2-3: Polarization in surface scattering (image credits: T. LeToan).

Depolarization occurs mainly over vegetation and it is unlikely to see it over open ground. The named cross polarization (HV or VH) is very sensitive and quite often used to measure over vegetation.

The signal parameters have to be chosen wisely depending on the target and the properties that want to be measured and observed. Over vegetation, the backscattered signal will be strongly dependent on the wavelength of the signal used as shown in the Figure 2-4. The signal is likely to interact with the primary

scatterers in a tree canopy like leaves, branches, and stems with a size on the order of the wavelength or larger and an orientation similar to that of the incoming signal polarization. So depending on the wavelength of the signal, different views of the same object can be obtained. By reducing the wavelength, for example, up to the X band (with a frequency around 10 GHz), the leaves of a tree due its complicated structure, roughness and geometry are going to scatter the signal in multiple directions and the radar antenna will receive a part of this signal. Like it was mentioned before in this chapter, the multiple scattering due the vegetation is likely to change the polarization of the signal. By increasing the wavelength, the structure of the tree can be seen where the branches and the trunks of the trees can be observed. It also has to take into account that elements smaller than the wavelength produce little backscatter and it can attenuate the amplitude of the signal.
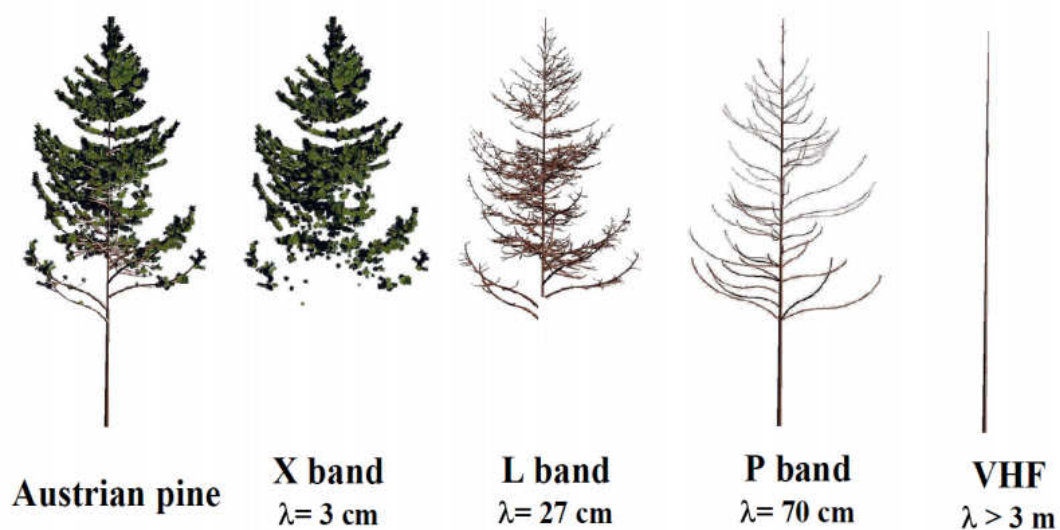
Figure 2-4: Reconstruction of an Austrian pine with the backscattered signal measured with different wavelengths on the emitted signal (image credit: Woods Hole Research Center).

In the Figure 2-5, a schematic of how the signal behaves depending on the signal polarization and wavelength used is shown. A signal is scattered by some elements around the same size of the wavelength of the signal, but depending on the polarization of the signal over the target different intensities are returned to the radar. For example, horizontal polarization is not

6

recommended to use when the trunks of the trees want to be detected clearly due the geometry of the trunk.
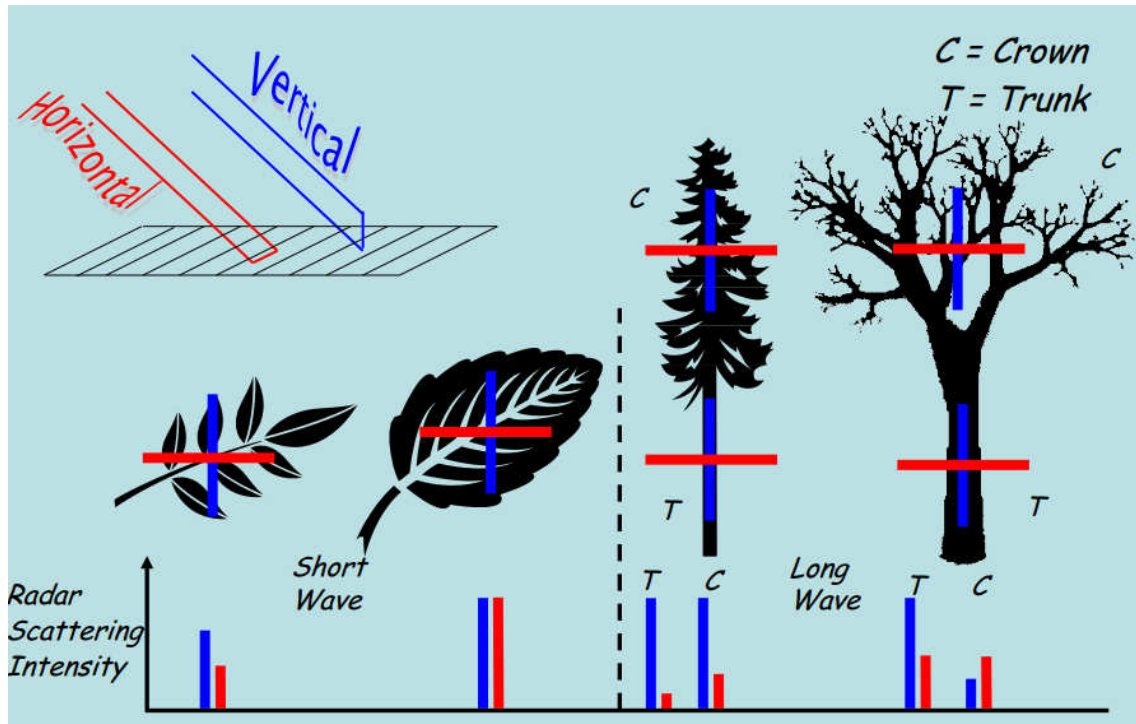
Figure 2-5: Signal intensity returned by different natural targets whit horizontal and vertical polarizations.

3 Synthetic Aperture Radar (SAR)

Synthetic aperture radar (SAR) imagery is the principal technique for gathering data globally. The goal of the SAR process is to improve the cross range resolution of a real antenna. The theory states that the properties of a long antenna can be simulated with a smaller one when a sufficient number of measurements are performed along its length [4]-[5].

In general, the larger the antenna, the better the cross range resolution in the image. The resolution of an image is defined as the separation between the two closest features that can still be resolved in the final image. SAR provides 2-D images with a slant range resolution δ_r and a cross range resolution δ_{cr}.

In most of the applications, it is not feasible to use big antennas due to the physical dimensions of the designs, so SAR techniques were developed to improve the resolution in the images.

SAR is a technique used to synthetise an extremely large antenna in order to provide a better resolution for side looking radar images. A typical SAR schematic is shown in the Figure 3-1. In order to produce a synthetic array, an antenna is moved and at different intervals a transmit/receive cycle is completed where each point measured constitutes one element of the synthetic array. By processing the data acquired in each measure and knowing the initial conditions of the measures performed (position of the antennas at each point and the characteristics of the signal transmitted), an antenna with the same characteristics as a real one with the size of the length aperture used in SAR can be synthetized. After processing the data, the synthetic beamwidth obtained with this is narrowed with respect the real footprint of the antenna, improving the cross range resolution.
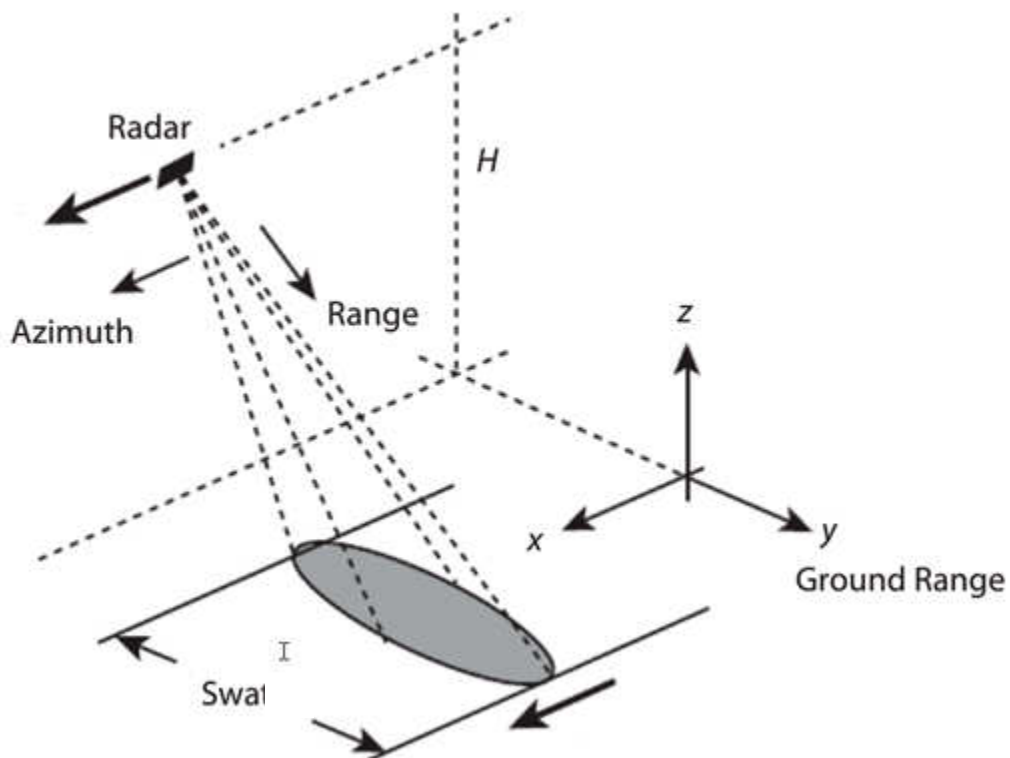
Figure 3-1: SAR schematic.

The slant range resolution δ_r of a SAR system, showed in the equation (3-1), is dependent of the pulse bandwidth used in the transmitted signal B where c represents the velocity of propagation of the signal.

$$\delta_r = \frac{c}{2B} \qquad \text{(3-1)}$$

The cross range resolution δcr of a real antenna depends on the distance between the antenna and the target R (also called range) and on the beamwidth produced by the antenna θ_B. The beamwidth of the antenna is a function of the wavelength of the signal λ, and the physical length of the antenna D. The equation for the cross range resolution of a real antenna is showed below:

$$\delta cr = R\theta_B = \frac{\lambda R}{D} \qquad \text{(3-2)}$$

According to (3-2), really big antennas with widths of kilometres would be needed to obtain a good resolution when a measure is performed in a range of kilometres using normal radar frequencies. These dimensions are not feasible in practice, and SAR systems are used to reduce the dimensions of the antennas.

As indicated before in this chapter, in SAR processing numerous low resolution cross-range looks are captured with a real antenna and processed to obtain a high resolution SAR image. The total synthetic array consists of all positions which an echo is received from a particular target.
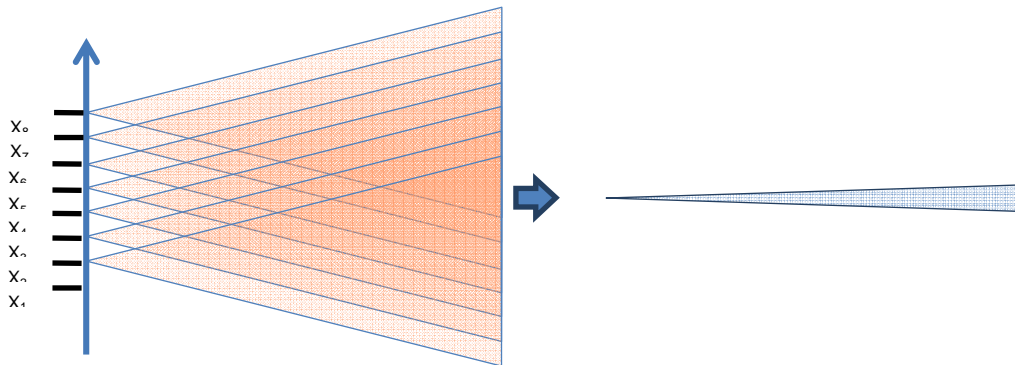
Figure 3-2: Coherent summation of a synthetic array.

A narrow beam is synthesized by processing the echoes acquired from each position of the synthetic array decreasing the beamwidth of the real antenna as shown in the Figure 3-2. This provides a much better cross range resolution than the one it would be obtained with a real antenna of the same size. The narrowed beamwidth θ_S is a function of the wavelength of the signal λ and of the effective synthetic aperture L_e.

$$\theta_S = \frac{\lambda}{2L_e} \tag{3-3}$$

Therefore, the cross range resolution of the SAR is:

$$\delta_{cr} = R\theta_S = \frac{\lambda R}{2L_e} \tag{3-4}$$

The maximum resolution is obtained when the effective aperture length synthesized with the SAR is equal as the maximum length aperture of the antenna.

$$L_{max} = L_e = \frac{\lambda R}{D} \rightarrow \delta_{cr} = \frac{\lambda R}{2(\frac{\lambda R}{D})} = \frac{D}{2} \tag{3-5}$$

The equation (3-5) shows the advantages of the SAR. The cross range resolution obtained with SAR is not anymore dependant on the range and the wavelength of the signal. Furthermore, the cross range resolution is only dependant of the physical size of the antenna and the smaller the antenna used in the radar; the better the resolution the SAR system has.

4 Interferometric Synthetic Aperture Radar (InSAR)

SAR is a coherent active microwave imaging method used to mapping the scattering properties of the Earth's surface. The use of this technique has the inconvenience that it does not provide resolution in the vertical direction, making impossible to distinct targets at different heights when the scatterers are often vertically distributed (i.e. buildings or vegetation). An image pixel therefore contains a superposition of several scattering contributions.

The Interferometric SAR (InSAR) is a technique that provides information of the apparent height in a SAR image. This is possible by measuring the phase differences of at least two complex-valued SAR images acquired from different positions and/or at different times [6]. The information obtained from these interferometric data sets can be used to measure several geophysical quantities, such as topography, deformations (volcanoes, earthquakes, ice fields), glacier flows, ocean currents, vegetation properties with high precision.

The SAR image is formed by a real part with the intensity or the amplitude of the backscattered signal and an imaginary part with the phase. For InSAR the phase information is taken into account to extract high precision digital elevation models (DEMs). The electromagnetic signal emitted by the radar is sinusoidal and due its periodicity, the phase value ϕ measured is proportional to the two-way travel distance divided by the transmitted wavelength as shown in the equation (4-1) and the Figure 4-1. In this way, travel distances that differ by an integer multiple of the wavelength introduce exactly the same phase change.
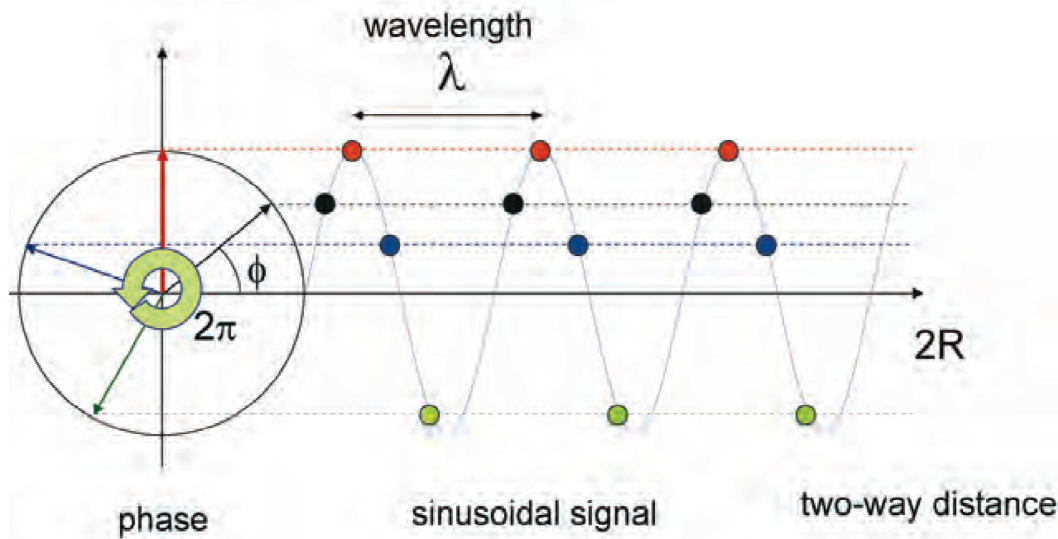
Figure 4-1: Phase values in a sinusoidal function sin φ periodic with a 2π radian period.

$$\phi = \frac{2\pi}{\lambda}2R = \frac{4\pi}{\lambda}R \qquad \textbf{(4-1)}$$

Figure 4-2 shows the typical InSAR geometry. A SAR system can observe the same area from slightly different look angles. This can be done either simultaneously with two radar system on the same platform or at different times by exploiting repeated measurements. The distance between the two satellites in the image in the plane perpendicular is called the interferometer baseline and its projection perpendicular to the slant range is the perpendicular baseline.

Since the wave is produced by the radar system, the phase created is known and can be compared to the phase of the return signals. When two image acquisitions varies slightly, the corresponding difference in the path means there is a phase shift between the two signals. The phase data of each of these acquisitions looks random, but when are subtracted the new image created shows a pattern. This difference gives the necessary information to obtain a vertical resolution in the SAR imagery.
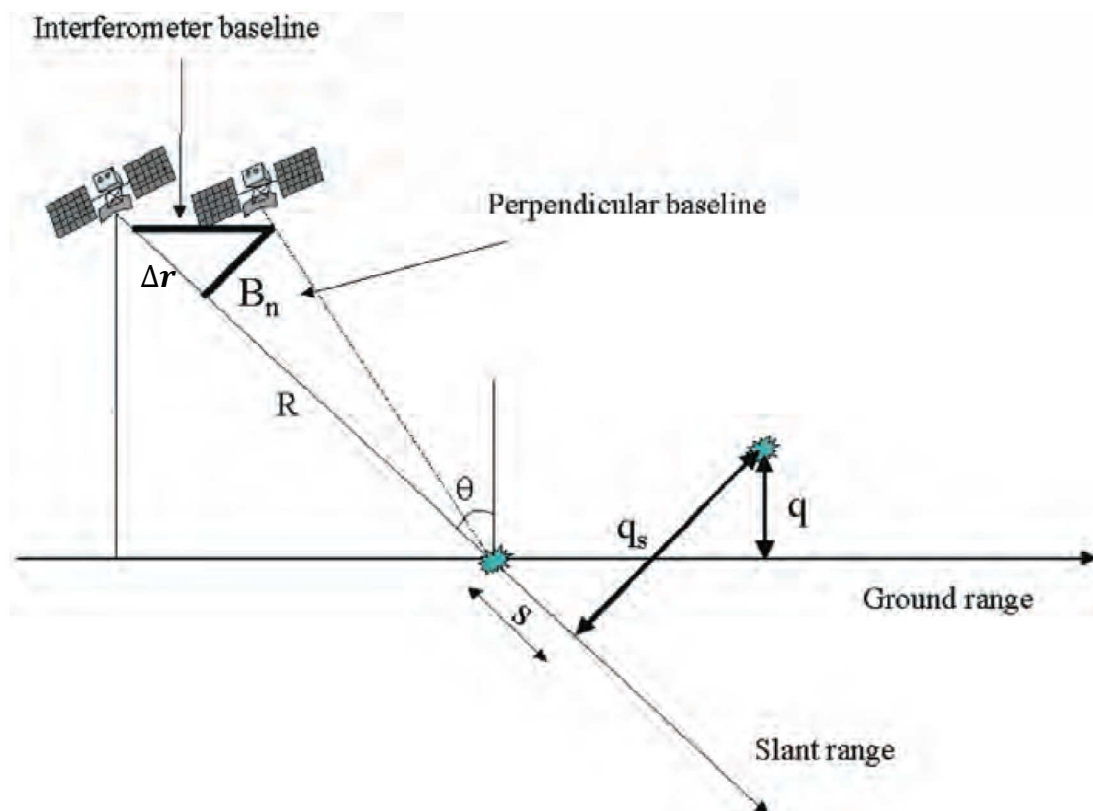
Figure 4-2: Geometry of a satellite interferometric SAR system (image credit: ESA).

In the Figure 4-2, the basic geometry of InSAR is shown to perform terrain altitude measurements. To understand better the concept, the reader has to suppose that there is only one dominant point scatterer in each ground resolution cell that does not change over time and the interferometric phase of each SAR image pixel would depend only in the travel paths.

The equation (4-2) shows the variation of the travel path difference Δr that results in passing from the reference resolution cell to another.

$$\Delta r = -2\frac{B_n q_s}{R\,sin\theta} \tag{4-2}$$

Where B_n is the perpendicular baseline, R is the range, θ is the radiation incidence angle with respect to the reference and the displacement between the resolution cells along the perpendicular to the slant range is represented by q_s.

The interferometric phase variation $\Delta\phi$ difference in the phase is shown in the equation (4-3) where the

$$\Delta\phi = \phi_1 - \phi_2 = \frac{2\pi}{\lambda}\Delta r = \frac{4\pi}{\lambda}\frac{B_n q_s}{R\,sin\theta} \tag{4-3}$$

Some image processing has to be done to obtain the final image [6]-[7]. To get an InSAR image, a called interferogram has to be created, then perform a flat earth removal, unwrap the phase values and see the coherence of the images.

5 SAR tomography

The SAR tomography is an evolution of the classical InSAR. The SAR tomography exploits the whole complex information and allows "scanning", with greater precision and robustness than classical interferometric techniques, the radar image pixels, and detecting different persistent scattering mechanisms even in each single pixel – or voxel – within a volume. This allows the reconstruction and monitoring of ground structures in high detail.

As shown in the Figure 2-4, the transmitted electromagnetic wave signal can penetrate through semi-transparent media making it possible to retrieve diverse characteristics of the target. Figure 5-1 represents the acquisition geometry for tomography acquisition, where it can be observed the cylindrical geometry of a SAR sensor makes these targets inseparable at the same range distance. Consequently, these targets appear at the same resolution cell. InSAR tries to deal with this problem with a second acquisition, but it makes only possible to retrieve a mean height of all backscattering contributions within the resolution cell. To retrieve the whole vertical distribution of the scatterers, tomography techniques are used. Tomography exploits the synthetic aperture concept, which requires the use of multiple passes of the SAR sensor over the same area but the sensor has to acquire the images from slightly different viewing geometries as shown in the Figure 5-1.

Tomography is really useful over vegetation areas. The estimation of the structural parameters, detection of objects hidden beneath the foliage or the study of the soils under the vegetation are some examples of possible applications that can be studied with this technique.
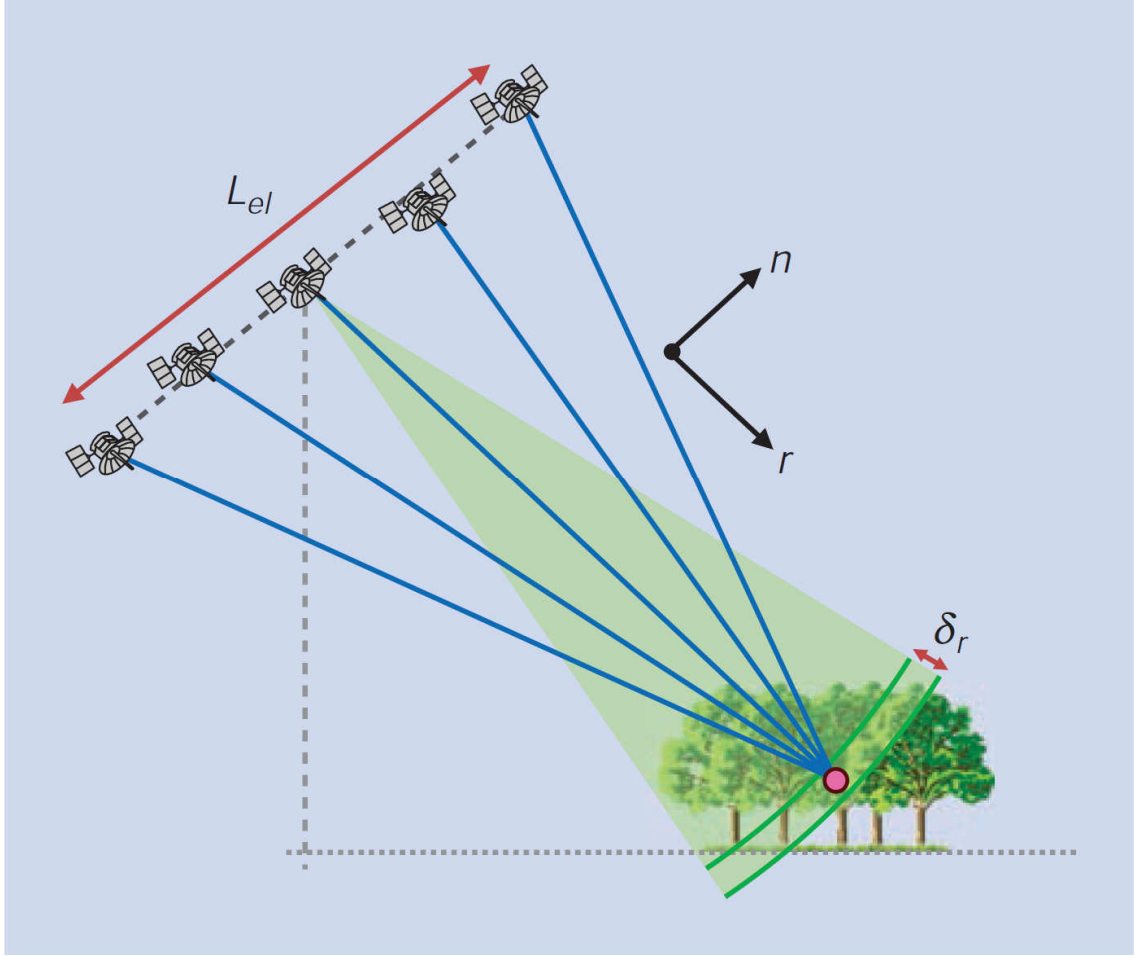
Figure 5-1: Acquisition geometry for tomographic imaging with a SAR sensor (image credit: ESA).

The resolution of the tomography is determined also by the length of the synthetic aperture in elevation, L_{el}, as shown in the equation (5-1).

$$\delta_n = \frac{\lambda R}{2L_{el}}$$

(5-1)

Where *n* represents the elevation axis, and a repeat-pass scenario is implicitly assumed.

In order to avoid high sidelobes and ambiguities, the sampling requirements of the tomographic aperture has to be taken into account. The minimum distance required between passes, μ, is shown in the equation (5-2).

$$\mu \leq \frac{\lambda R}{2h_v}$$

<div align="right">(5-2)</div>

Where μ depends on the total height of the volume in the direction perpendicular to the line of sight, h_v.

The more passes performed acquiring SAR images, the better the resolution it will be obtained with SAR tomography but the complexity of the acquisition geometry then will be increase.

An example of a polarimetric tomographic image of a forest area taken by DLR in 2006 [8] is shown in the next Figure 5-2. This image is made by processing 21 different SAR acquisitions with an average baseline of 20 m. This kind of images allows to distinct the contributions of the target by different colours. The image shows a blue component for the surface scattering, red for the dihedral ground-trunk interaction and green for the volume canopy.
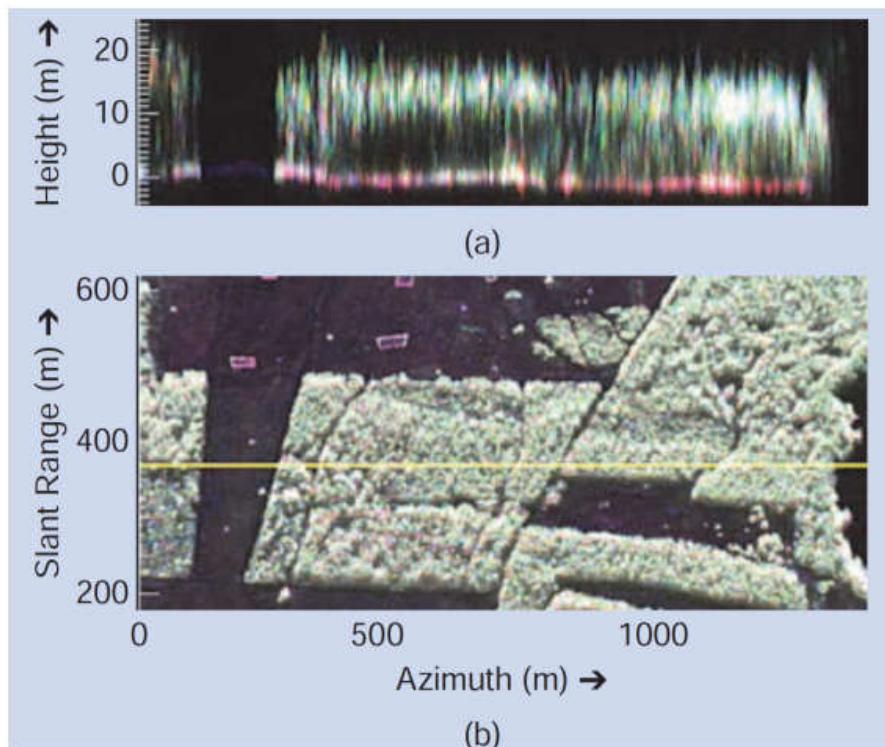
Figure 5-2: Polarimetric tomographic profile over a forested area using DLR's E-SAR system at L-band. (a) Vertical perspective (b) Horizontal perspective (image credit: DLR).

6 SAR Satellite measurements

Nowadays, there is a fleet of satellites equipped with SAR systems dedicated to civilian and military purposes.

The first part of this chapter gives an introduction to the most common operation modes of radar satellites. After this description, a second part with a listing of the satellites and missions is provided.

6.1 Operational modes

6.1.1 Stripmap

Probably this is the mode more used with SAR systems. The radar antenna points along a fixed direction with respect the flight trajectory. With the movement of the platform and sending a series of pulses, the antenna footprint covers a strip on the illuminated surface.
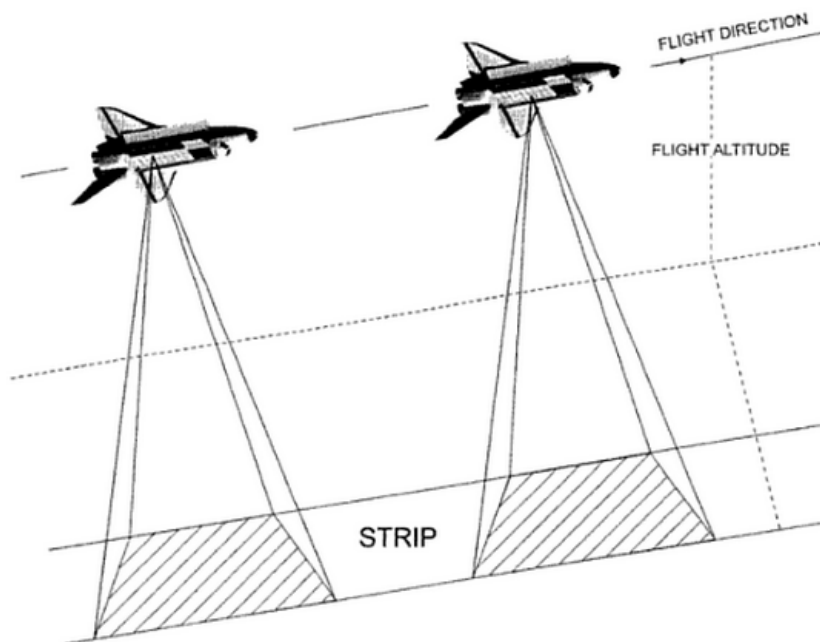
Figure 6-1: Schematic of the stripmap operation mode.

6.1.2 ScanSAR

Usually the resolution of this method is worse than the one used in the stripmap method, but the area covered is larger. In this method, different areas are illuminated by the radar at different positions.
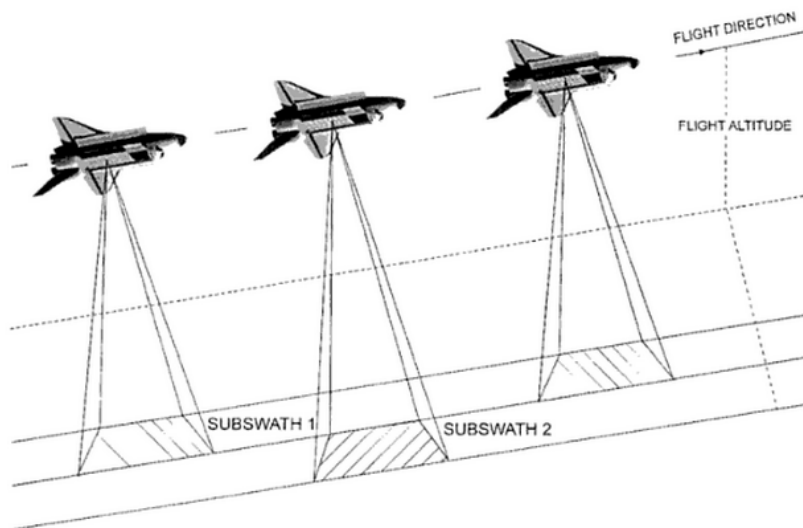
Figure 6-2: Schematic of the scan operation mode.

6.1.3 Spotlight mode

This method is used when a high resolution of a determined area is needed. The satellite continuously orientates the antennas to keep a target within the beam for a longer period than would otherwise be possible for linear SAR.
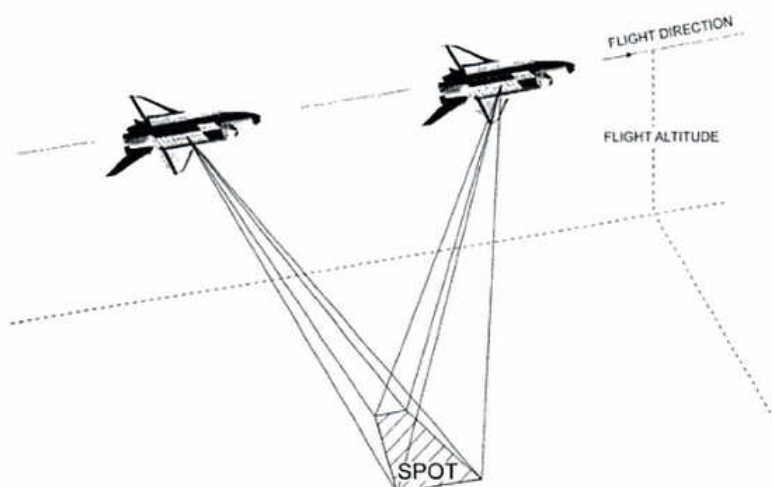
Figure 6-3: Schematic of the spot operation mode.

6.2 SAR satellites

Since the first satellite with a radar payload was launched in 1962, the Gemini radar, significant developments have been made in the technology and in the space-based radar systems. These developments have improved the knowledge that it can be extracted from radar imagery and numerous applications have arisen such as monitoring forest states, sea ice monitoring, natural disaster control or mapping with digital elevation models the Earth to give some examples.

During the last decades and depending on the mission of each satellite, diverse missions with different characteristics have been launched and working at different band radar wavelengths. All those missions together have provided and will provide the necessary information to provide an input to develop useful applications for humans.

Below, some satellites describing their main characteristics are shown.

6.2.1 Current satellites

6.2.1.1 TerraSAR-X Radar Satellite Imagery and TanDEM-X (TerraSAR-X add-on for Digital Elevation Measurement)

TerraSAR-X was developed under a partnership between the German Aerospace Center (DLR) and EADS Astrium and was launched on the 15th June 2007. This satellite is designed to acquire high-resolution and wide-area images with high accuracy [9].

The TerraSAR-X is equipped with an X-band antenna (wavelength 31 mm, frequency 9.6 GHz) to acquire high-quality radar images of the entire planet thanks to its polar orbit at 514 km of altitude. It can acquire images up to 1 m of resolution with an excellent radiometric accuracy. DLR offers the commercialization of the images and any point on the Earth can be acquired by request within 2.5 days.

On June 2010, a twin satellite of the TerraSAR-X, the TanDEM-X (**T**erraSAR-X **a**dd-o**n** for **D**igital **E**levation **M**easurement) was launched and it was designed to work in formation with TerraSAR-X to obtain digital elevation models of the Earth. With both satellites working, interferometry techniques can be used and discrimination in height can be obtained in the images [10].
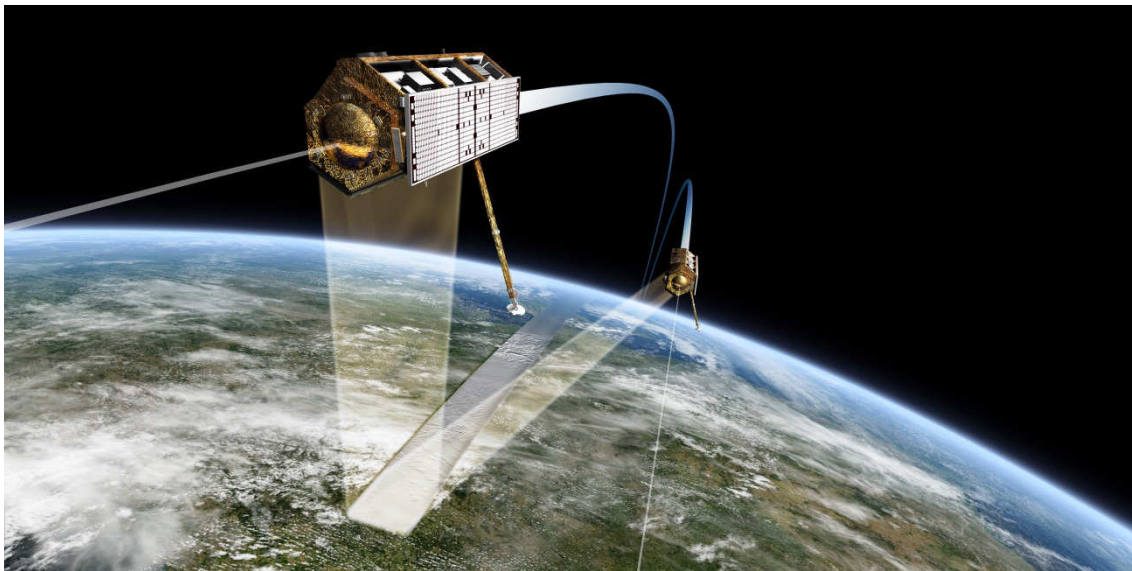
Figure 6-4: TanDEM-X and TerraSAR-X flying in formation (image credit: ESA).

The two satellites flight in a controlled close formation, between 250 and 500 m, and thanks to it and its unique configuration have allowed during the last years to acquire a collection of accurate DEM to create the WorldDEM^{TM} with images of the Earth.

6.2.1.2 COSMO-SkyMed (Constellation of small Satellites for the Mediterranean basin Observation)

COSMO-SkyMed consists of four identical medium-sized satellites equipped with SAR sensor to cover the planet. The great advantage of this system is that a certain area can be observed several times per day in all-weather conditions [11].

The first satellite of COSMO-SkyMed constellation was launched in June 2007, finishing the constellation in 2010 with the launched of the last satellite. The satellite constellation was developed in Italy and it was designed to provide services to civil and military users.
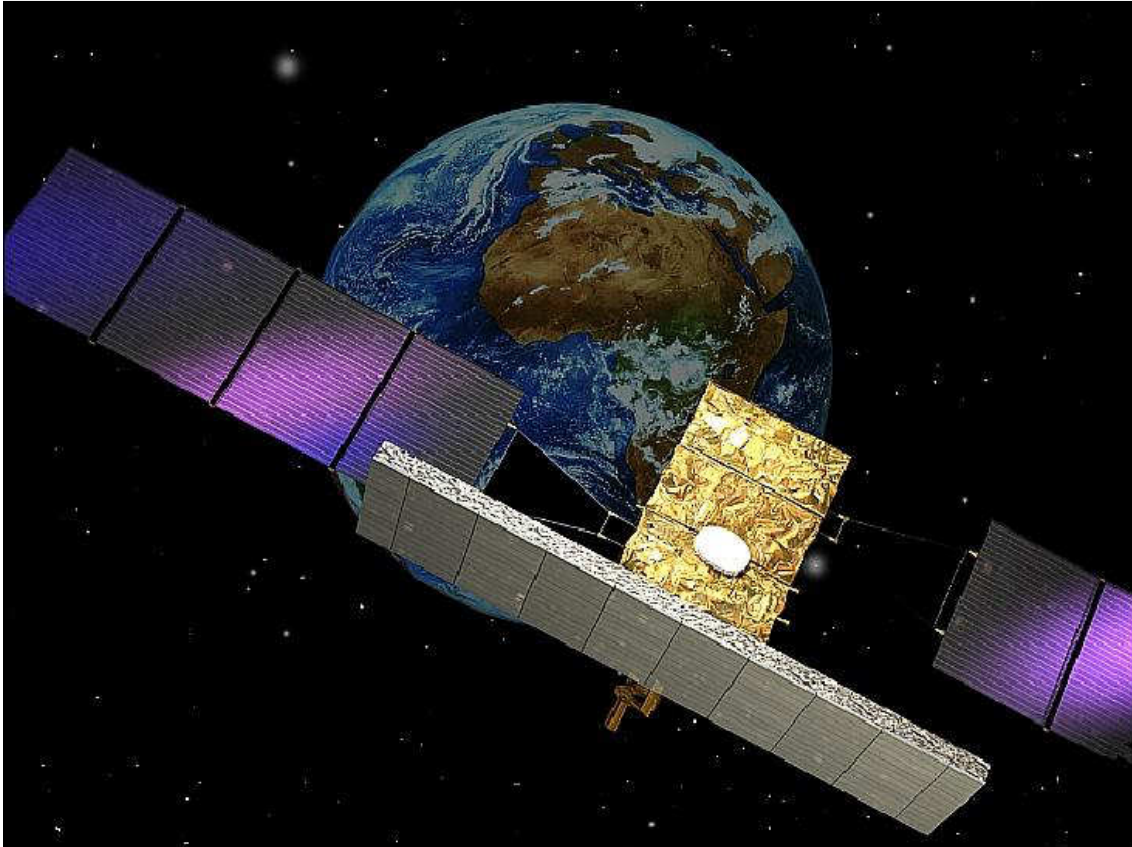
Figure 6-5: Artist's rendition of a COSMO-SkyMed spacecraft in orbit (image credit: ASI)

6.2.1.3 Sentinel-1A

SENTINEL is an ESA project to launch different satellites to create the next-generation Earth observation fleet to replace the satellites that are not working anymore or are currently at the end of their operational life.

Nowadays, Sentinel-1A is part of a constellation of two satellites and it is the only one that was launched and working in its orbit. Sentinel program will offer a global monitoring programme in order to manage the natural resources, understand and tackle the effects of climate change, and safeguard everyday lives.
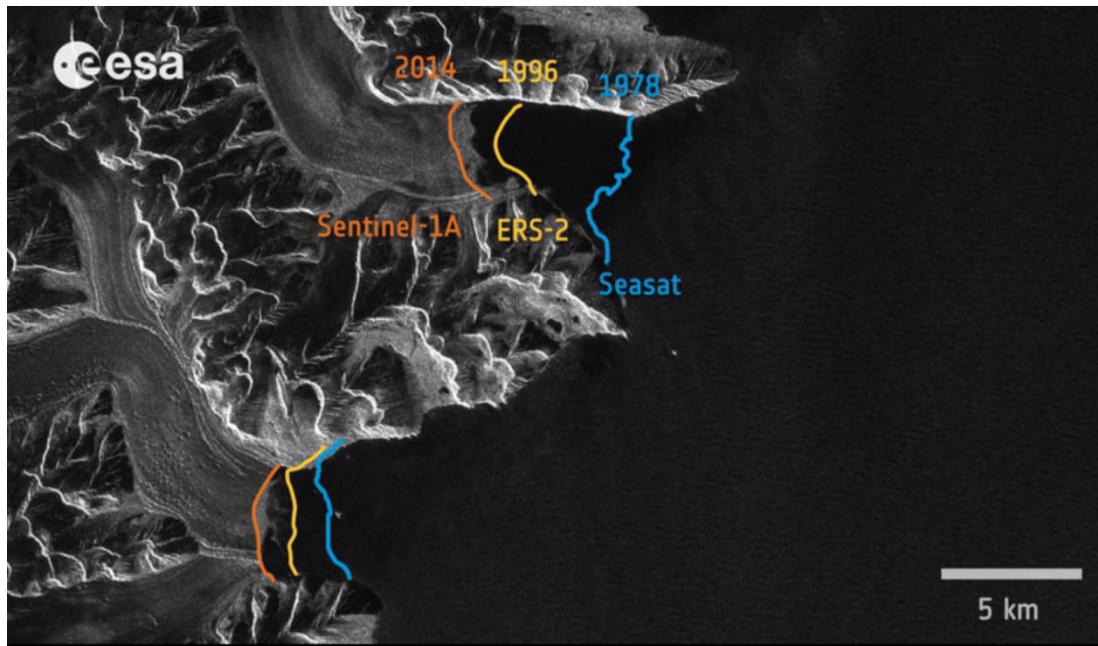
Figure 6-6: Comparison of the Greenland glaciers between three different generations of radar missions (image credit: ESA).

Sentinel-1A carries an advanced C-band SAR instrument to provide an all-weather, day-and-night supply of imagery of Earth's surface. This C-band SAR is a heritage of different systems from previous satellites such as ERS-1, ERS-2, Envisat and Radarsat [12].

One of the applications that Sentinel can offer is to monitoring the Artic sea-ice extent and appreciates their variations along the time, as showed in the Figure 6-6. In this image, the comparison of three data sets acquired on the same area with different instruments and different years can be seen. The borders of the glacier are painted according with the radar images that were acquired at each year allowing performing a study of the area.

Sea-ice mapping, surveillance of the marine environment, detection of oil-spill and ship detection for maritime security, monitoring land-surface for motion risks, mapping for forest, water and soil management are some of the numerous services that the Sentinel project will provide.

Each mission will increase the capability of Earth observation and will provide the necessary data to be used in different applications.

6.2.1.4 RADARSAT-2

RADARSAT-2 is the continuation of the RADARSAT-1 work, which finished its life in 2013. RADARSAT-2 has the objectives of monitoring the environment; obtain information to manage natural resources and performing coastal surveillance [13].

Figure 6-7: Artist's rendition of the RADARSAT-2 satellite in orbit (image credit: MDA).

RADARSAT-2 is a Canadian satellite working at C-band with a fully polarimetric antenna funded by the CSA (Canadian Space Agency) and MDA (MacDonald Dettwiler Associates Ltd. of Richmond, BC). This satellite has a unique capability unlike any other satellite; its left looking capability allows imaging the Antarctic on a routine basis providing data in support of scientific research.

6.2.1.5 ALOS-2 (Advanced Land Observing Satellite-2)

The ALOS-2 is a follow-on mission from the "Daichi" (ALOS) and both of them were developed by the JAXA (Japan Aerospace Exploration Agency). The main

mission of the ALOS satellites is to cartography, perform regional observation, disaster monitoring and resource surveys. Due the location of Japan in the middle of a seismic area, JAXA has thought about the social needs and has improved ALOS to improve the detail of the images that the satellite can obtain from damage areas due natural disasters. It also updates continuously the data archives related to the national land and infrastructure information, monitors effectively cultivated areas and perform a global monitoring of tropical rain forest to identify carbon sinks.

Aboard in the ALOS-2, an L-band SAR system called PALSAR-2 can be found. This L-band SAR works using a 1.2 GHz frequency range in al weather conditions [14].

Figure 6-8: Artist's rendition of the ALOS-2 satellite in orbit (image credit: JAXA).

6.2.2 Future satellites

6.2.2.1 Biomass

In 2013, the Biomass mission concept was selected to become the next in the series of satellites developed to further our understanding of Earth.

The main goal of this satellite is to take measurements of forest biomass to assess terrestrial carbon stocks and fluxes. To achieve the objectives of the mission, this satellite will have a P-band SAR radar operating at 435 MHz with a 6 MHz bandwidth [15]. With this wavelength the signal penetrates the leafy canopy to see the big branches and trunks. The use of this new sensor will also allow provide new information on ice-sheet thickness and internal structures in cold regions, subsurface geology in arid regions, as well as data on soil moisture, permafrost and sea-surface salinity.

This mission will provide information really important like the status of the forests and the distribution of biomass and how it changes.
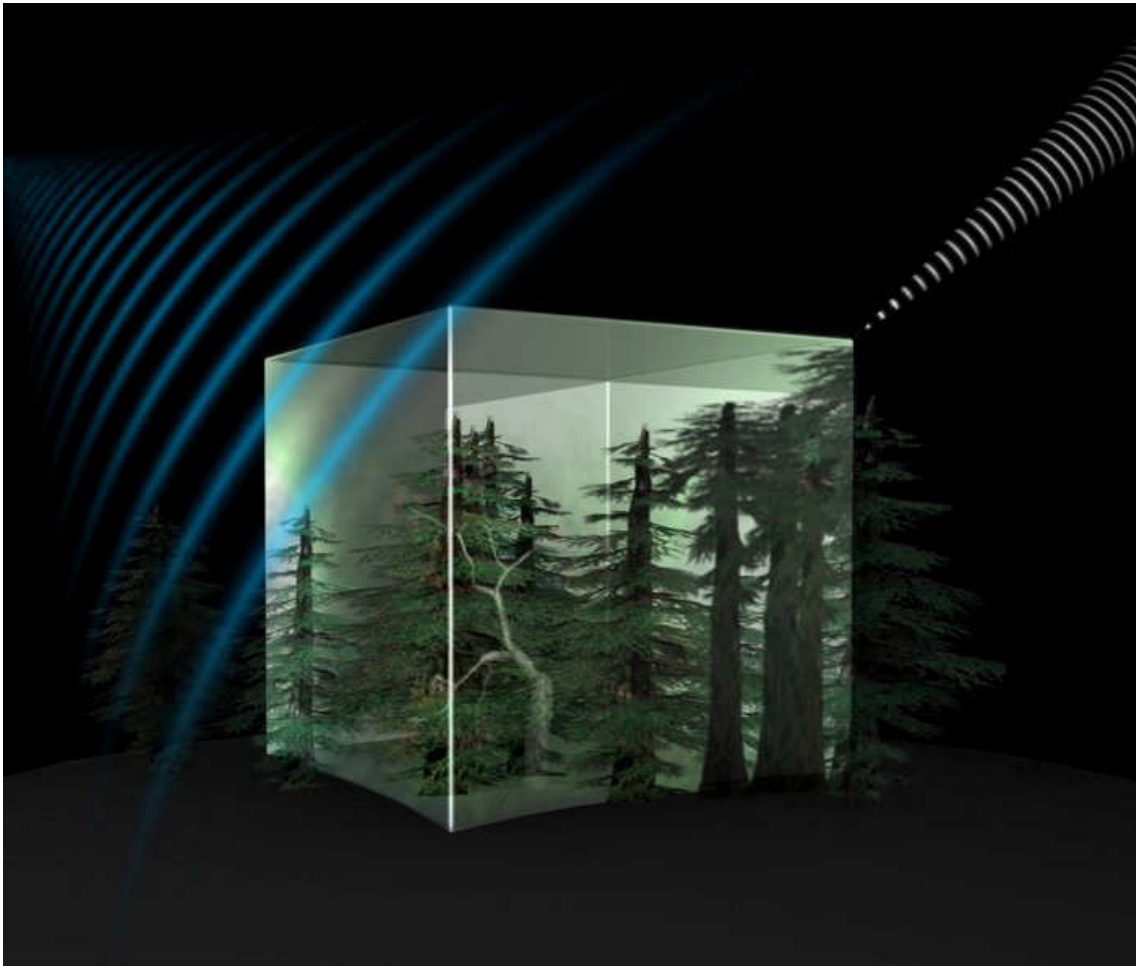
Figure 6-9: Artistic representation of the measurements of the future satellite Biomass (image credit: ESA).

Satellite	Launched	Band/Polarizations	Remarks

TerraSAR-X	15 Jun 2007	X – Different configurations for the polarization of the antenna	• Three main imaging modes:
			
			  o SpotLight (up to 1 m resolution - scene size 10 km x 5 km)
			
			  o StripMap (up to 3 m resolution - scene size 30 km x 50 km)
			
			  o ScanSAR (up to 16 m resolution - scene size 100 km x 150 km)

TanDEM-X	21 Jun 2010	X – Different configurations for the polarization of the antenna	• It is almost a twin satellite of the TerraSAR-X. • Designed to fly in formation with TerraSAR-X and acquire DEM of the Earth.

RADARSAT-2	14 Dec 2007	C at 5.405 GHz / Full polarimetric configuration.	• Its left looking capability allows the spacecraft the unique capability to image the Antarctic on a routine basis providing data in support of scientific research.
			
			• Imaging modes:
			
			  o SpotLight (up to 1 m resolution with 100 m positional accuracy requirement. - scene size 10 km x 10 km)
			
			  o ScanSAR Wide Beam (100 m resolution - scene size 500 km x 500 km)

Satellite	Launched	Band/Polarizations	Remarks
COSMO-SkyMed	8 Jun 2007	X – Single and dual polarization collection depending on the imaging modes.	- Four medium-sized satellites - Central frequency 9.6 GHz with a maximum bandwidth of 400 MHz. - Three main imaging modes: - SpotLight (up to 1 m resolution - scene size 10 km x 10 km) - StripMap: Two modes. - HIMAGE (3 m resolution - scene size 40 km x 40 km) - Ping Pong (15 m resolution – scene size 30 km x 30 km) ScanSAR: Two modes. - Wide Region (30 m resolution - scene size 100 km x 100 km) - Huge Region (100 m resolution – scene size 200 km x 200 km)
ALOS-2	24 May 2014	L / Depending on the imaging mode	- Main target areas: forest, sea ice, river, rice field monitoring, deformation, volcanos, change detection, resource finding. - Imaging modes: - Spotlight (up to 1 m x 3 m resolution – swath 25 km) - Stripmap (3 m resolution – swath 50 km) - ScanSAR (100 m resolution –swath 350 km)

Satellite	Launched	Band/Polarizations	Remarks
Sentinel-1A	3 Apr 2014	C	• Earth observation, emergency mapping on natural disaster, sea ice and iceberg monitoring, sea vessel and oil detection. • Imaging modes: ○ Strip Map Mode (80 km Swath, 5 m x 5 m spatial resolution) ○ Interferometric Wide Swath (250 km Swath, 5 m x 20 m spatial resolution) ○ Extra-Wide Swath Mode (400 km Swath, 25 m x 100 m spatial resolution) ○ Wave-Mode (20 km x 20 km, 5 m x 20 m spatial resolution)
Biomass	Expected in 2020	P	• Future mission to improve the knowledge and the understanding of the Earth: perform measurements of forest biomass, ice-sheet thickness and internal structures in cold regions, subsurface geology in arid regions, as well as data on soil moisture, permafrost and sea-surface salinity. • Equipped with a P-band SAR radar operating at 435 MHz with a 6 MHz bandwidth.

Table 6-1: List of satellites mentioned with SAR systems aboard and their mains characteristics.

7 The Ground-Based SAR System (GB-SAR)

As described in [2], Cranfield University's Ground-Based SAR (GB-SAR) System is a continuous waveform (CW) portable system developed to acquire SAR images. During the years, it has been used to perform multiple tests and investigate radar backscatter from soils and vegetation.

An off-road vehicle is used to tow the whole system. The microwave sub-system is comprised of an RF circuit based around a vector network analyzer (VNA, the radar unit), feeding to a set of polarimetric antennas; formed by four similar antennas with two of them in a horizontal position and the other two in a vertical position, through runs of coaxial cable. An electromechanical sub-system is used to control mechanical movement and positioning of the system. The system is computer-controlled, which also acts as a data-logger.

Figure 7-1: GB-SAR mounted at full height and ready to measure barley at Colleymore Farm. Photograph took on 15th of June of 2015.

The acquisition of measurements is controlled by the user by means of the laptop. A cluster of interchangeable antennas is installed on the rail of the GB-SAR and connected to the VNA. Via software, the user can control all the RF and mechanical parameters of the data acquisitions; scan length and sampling interval along the scanning boom, initial and final bandwidth of the transmitted signal, polarization of the signal, manage the data acquired, control of the stepper motors and so on. Once the user has introduced the parameters and has launched the measurement, the whole system is controlled automatically by the software moving the antennas to the different points selected by the user, where a signal is transmitted by an antenna and the scattered signal is received by another antenna. The two antennas are closely positioned so as to allow a monostatic assumption. The data acquired at each position of the antenna with the VNA then is saved in a file.

The flexibility of the GB-SAR allows putting in practice various imaging scenarios. The position and the setup for each test can be easily changed, so the system offers the possibility to acquire sets of single SAR images, interferometric SAR (InSAR), or tomographic Profiling (TP) [16]. Bistatic SAR and multistatic SAR are also possible with some modifications on the system. The repeatability that the system offers in the measurements allows detecting in a controlled area changes on the scene using a change coherent detection (CCD) technique.

7.1 Tomographic Profiling (TP)

An in-house imagery scheme has been developed specifically as a diagnostic imaging tool to look at the scattering pattern through biophysical and geophysical volumes such as forest canopies, ice, snow or vegetation. Data is acquired in the same way as a SAR but instead of setting the antennas in a side-looking point of view with respect the target, they are aligned in the along-track direction (i.e. rotated 90 degrees). The data processing is also different. In a single scan, TP captures detail on the vertical backscattering through a target volume over a continuous range of incidence angles [3].

A schematic of the TP imaging process with the GB-SAR is shown in Figure 7-2. In the along-track direction, the use of a wide beam is advantageous, as broader beams can be employed to cover a bigger range of incidence angles. As it can be seen in the schematic of the TP imaging process, the real beam is too wide to obtain a good resolution in height. In order to solve this problem and obtain a much better resolution, a SAR-like process scheme is performed. The antenna moves along the scanner and performs a radar measurement at each interval, d_X, to build up a synthetic aperture. The data acquired is processed to produce a narrowed synthetic beam that can be steered over a range of inclination angles within the wider real beam. This processing gives as a result an improvement of the horizontal and vertical resolution.

In the same way as SAR image doesn't have any height discrimination because all the vertical topography is projected onto the horizontal plane, the TP image doesn't have any discrimination in the across-track direction (out and in of the page). This is due the change of the plane that it has to be done to perform the TP technique. For the use of the TP, a narrow beamwidth in the across-track direction (ϕ value in Figure 7-4) would be an advantage to have a better resolution of the target because this technique does not allow any discrimination in this direction. The final image of the TP will be an overlay of the scattered signal within the beamwidth in the across-track, ϕ, onto the central slice. The image in Figure 7-2b shows the beamwidth in the along-track direction of the measurements. In the same way SAR images do not have resolution in the vertical plane; the TP images do not separate targets in the along-track direction of the measurements. As shown in the image, the 2D TP image is formed in the vertical plane of the antennas marked by a red line, but this also receives contributions from the scatterers in the scene within the real beamwidth of the antennas in the across track direction that are in the same range slice from the antennas. In this way, the areas marked in the image as a, b, c and d, will add to a pixel in the middle that will have the contributions of these different areas. In the same way, the pixel below this one will be formed with the backscattered signal precedent of the areas e, f, g, and h. Due the geometry of the schematic it can be observed that depending on the

configuration and the beamwidth of the antennas in this direction, the upper part of the plants that are further from the centre of the antennas makes its contribution in the 2D image as they were shifted down.
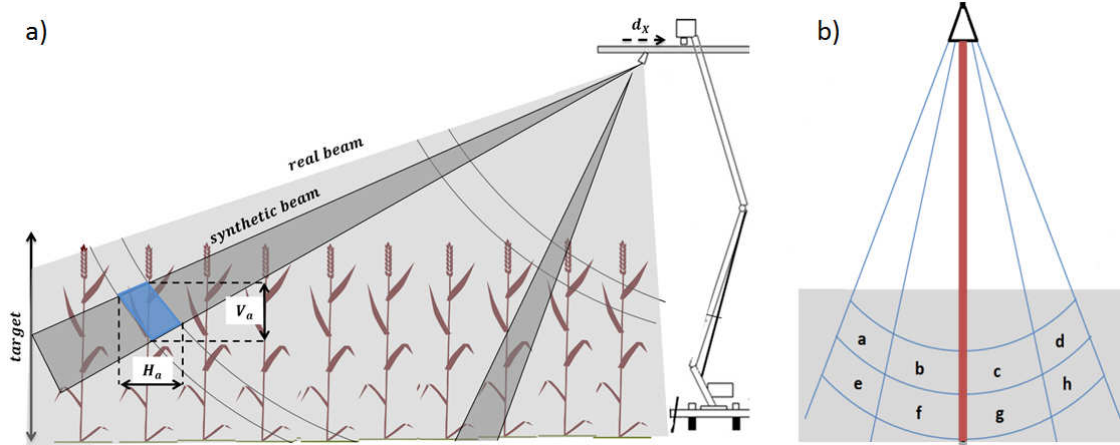
Figure 7-2: Schematic of the TP process. a) Vertical view of a standard setup for a TP on the field. In practice, the hoist was used at around half height or lower. b) View of the TP process in the along-track direction of the measurement.

As shown in Figure 7-3, processing the data and sliding a sub-aperture (D) along the total aperture (L) measured with the radar, the synthetic beam can be steered. This is really an advantage because with only one set of measurements the synthetic beam can be steered through the volume target to study; retrieving views of the scene from different incidence angles.

Each point generated in the image P is obtained processing the data obtained at each of the points measured within its sub-aperture D. To obtain the image of a point next to the point P at a distance d_X inside the volume target in the Figure 7-3, a new sub-aperture with the same D length and displaced the same distance d_X has to be selected. In this way, by processing the data acquired at the different points within each sub-aperture D generated across the total aperture L, each point of the image can be generated.
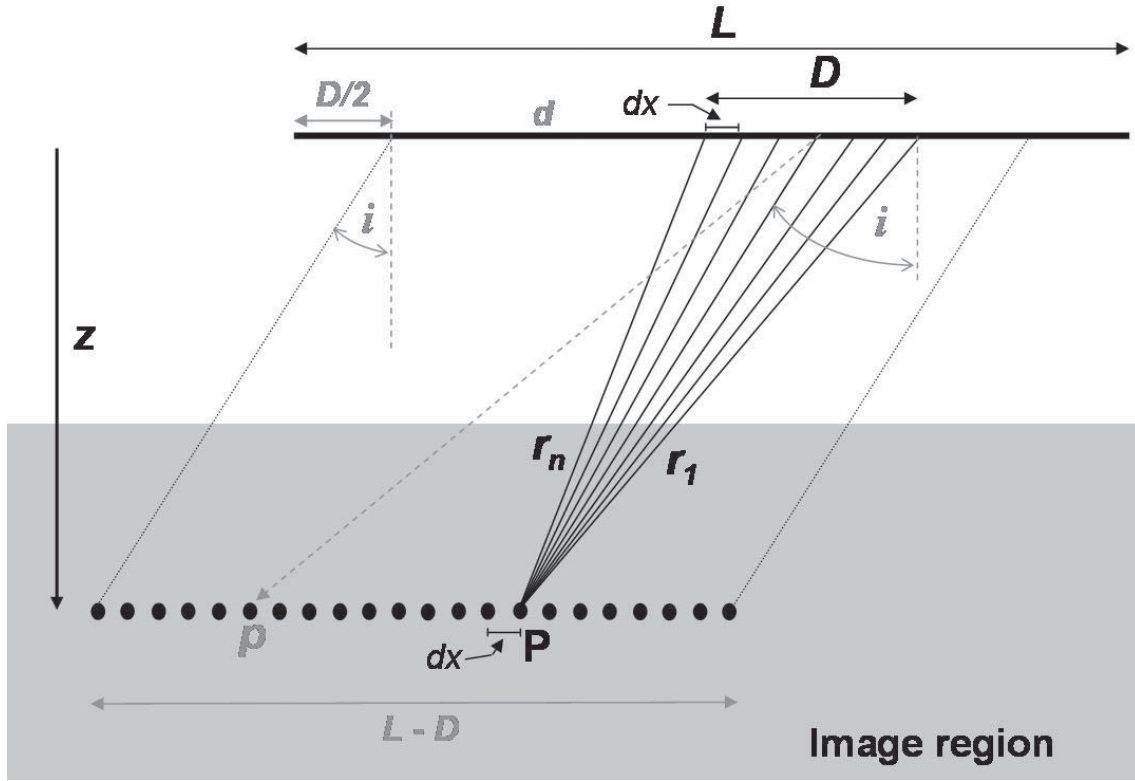
Figure 7-3: Schematic of the principle of the TP imaging technique.

The next part of this chapter will describe the resolution of the TP technique and its dependence of the different parameters used during the measurements. The resolution in the slant range direction res_R showed in the Figure 7-4 is dependent on the bandwidth used in the radar signal following the next equation.

$$res_R \ = \ \frac{c}{2B}$$ (7-1)

Where B is the bandwidth of the signal.

The resolution in the cross-slant range direction, res_X, behaves following the next equation (7-2).

$$res_X = \theta_{syn}R = \frac{\lambda R}{2Dcos(i)}$$ (7-2)

Where the value of θ_{syn} is fixed by the antenna used and it is the -3dB width of the synthetic beam. D is the length of the synthetic subaperture used, i is the look angle away from the normal to the aperture, R is the slant range or the distance between the antenna and the point to measure and λ is the wavelength of the signal.
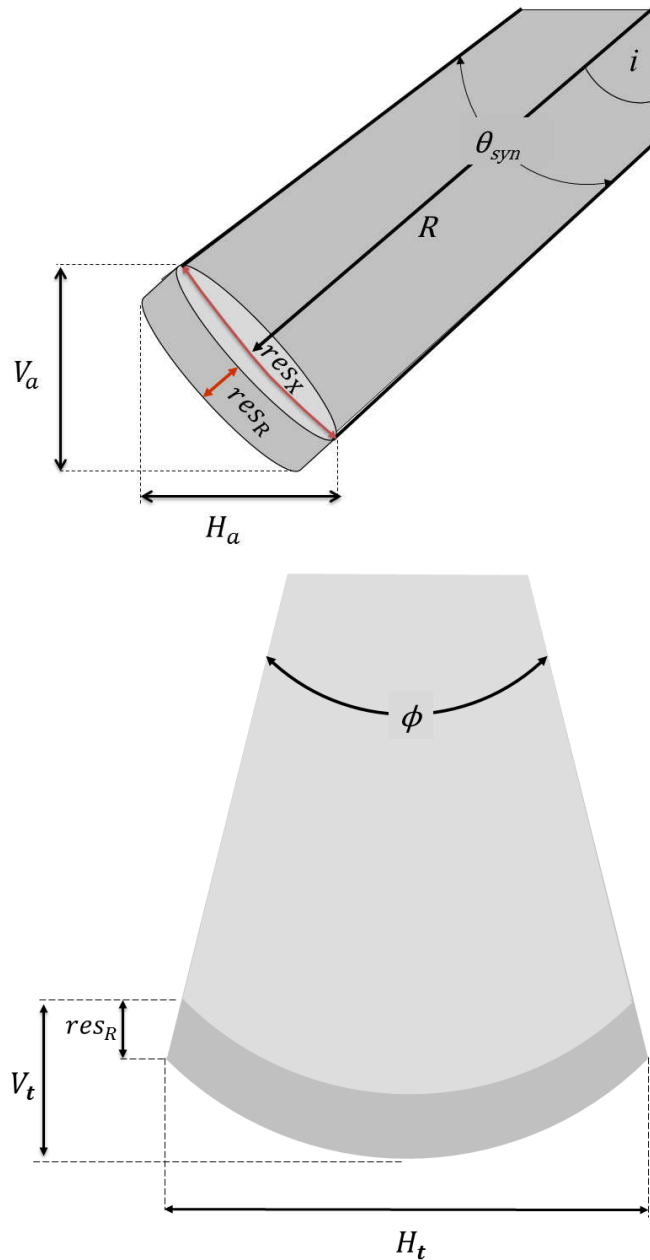
Figure 7-4: Schematic of the vertical and horizontal resolution present in the Tomographic Profiling technique.

On the top image of the Figure 7-4, the vertical resolution, V_a, can be calculated by trigonometry once that the resolution in the slant range and the cross-range are known.

$$V_a = res_R \cos i + res_X \sin i \qquad \textbf{(7-3)}$$

In the same way, the horizontal resolution H_a is given by the next expression.

$$H_a = res_R \sin i + res_X \cos i \qquad \textbf{(7-4)}$$

The TP is a technique that allows obtaining information from a volume target. The resolution in the transverse across-track real beam has to be taken into the account. On the bottom of the Figure 7-4 a view of the scene on the left is rotated 90º. In this direction, the resolution H_t showed is given by the next equation.

$$H_t = \phi R \qquad \textbf{(7-5)}$$

Where ϕ is the width of the effective transmit-receive beam in the across-track direction. The value of ϕ is determined by the design of the antenna used during the measurement, as equal as the previous factor θ_{syn}.

The vertical resolution in the transverse across-track direction V_t, is given by the following equation.

$$V_t = \left[R(1 - \cos \phi_{\frac{1}{2}}) + res_R \cos \phi_{\frac{1}{2}} \right] \cos i \qquad \textbf{(7-6)}$$

Where $\phi_{\frac{1}{2}}$ is the halfwidth of ϕ. The vertical resolution of any point of the image is determined by the maximum value between V_a and V_t, and the horizontal resolution will be determined by the maximum value between H_a and H_t.

$$V(p) = \max\{V_a(p), V_t(p)\} \qquad \textbf{(7-7)}$$

$$H(p) = \max\{H_a(p), H_t(p)\} \qquad \textbf{(7-8)}$$

In the Figure 7-5, it can be observed a graph with the resolution of the TP technique in a specific case working at X-band with three different heights (2, 5

and 9 m) representing a typical case using the GB-SAR system. The final resolution obtained is dependent on the incidence angle where the image wants to be reconstructed.
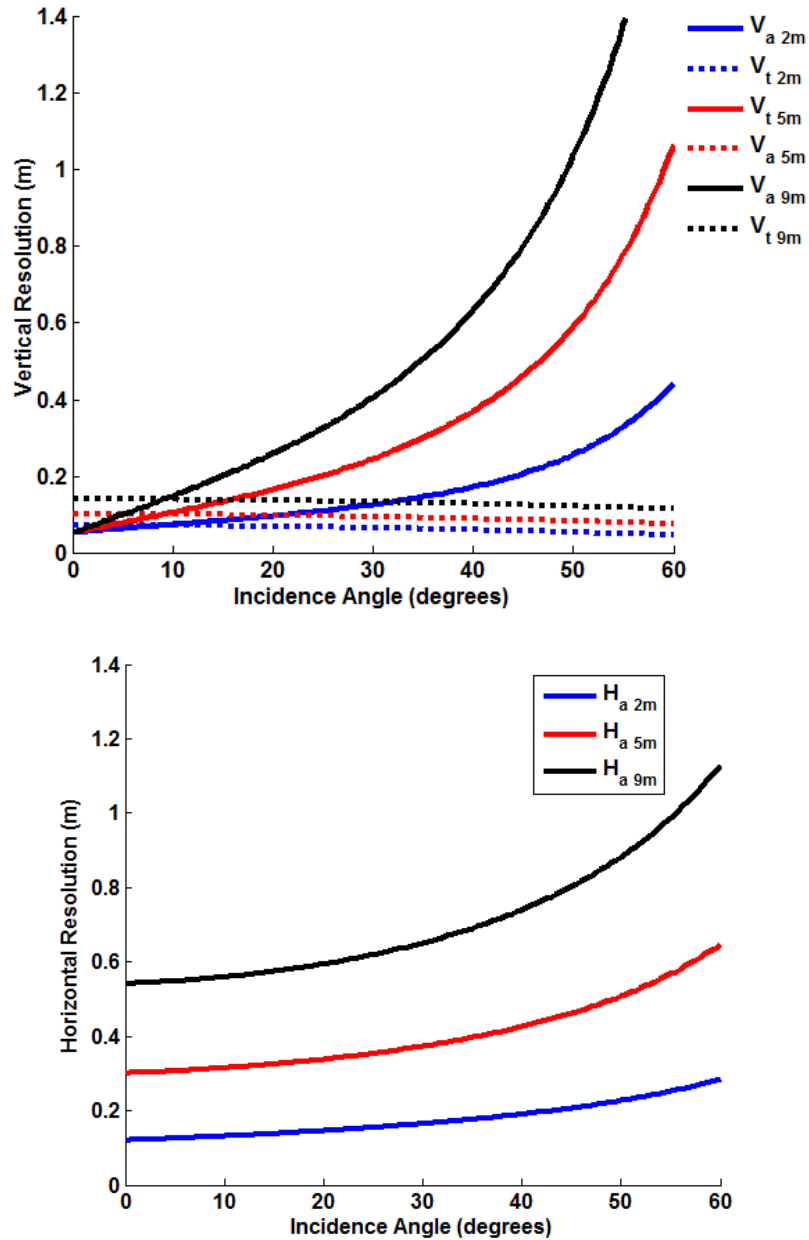
Figure 7-5: Graph of the vertical and horizontal resolution using the Tomographic Profiling technique with the GB-SAR at 10.125 GHz, bandwidth 3.75 GHz at different heights (2, 5 and 9) using a subaperture D of 0.32 m and with a Φ of the antenna of 16º.

Unfortunately, this technique loses resolution with the range. This makes it unavailable to obtain a good resolution measuring with satellites but it can be used with unmanned aerial vehicle (UAV) flying with a low attitude flight from the area of interest that want to be studied obtaining resolutions in the order of 1 or 2 m.

8 Field experiments: Barley.

A series of radar and biological measurements have been performed to study the iteration of radar signal over vegetation. These measurements have been done in a farm through the growing season of the barley, from April to the end of July. A detailed description of the radar measurements is provided in this chapter.

8.1 Location: Colleymore Farm

An exhaustive investigation was undertaken of the different crops and plants that could be available locally around the campus. Local farmers were contacted but were reluctant to be involved. Eventually, Colleymore Farm offered access to a barley field site to perform a campaign of measurements during the growing season, nominally every two weeks. The measurements were done depending always on the weather conditions (wind speeds nominally lower than 4 mph and absence of rain). The close proximity of the farm to the laboratory at Cranfield University made this place ideal to run this campaign.

Figure 8-1: Photo of the barley field at Colleymore Farm on the 04/06/2015.

Figure 8-2: Location of the Colleymore Farm (51º 36'59.5ºN 1º39'05.3''W) (red square) and Cranfield University in Shrivenham (blue square).

8.2 Radar measurements

In order to perform a complete study of the radar images over barley, diverse radar measurements with different configurations have been performed on the field with the GB-SAR system; described in the chapter 7, through the growing season of the crop.

The measurements were done under two weather conditions: absence of rain and very low wind speed. Experience indicated the choice to undertake field measurements was based on predicted wind speeds 0-4 m/s. Still conditions are required to obtain radar images over vegetation to avoid changes of the physical scene due the movement of leaves, branches or any other part of the plants that could be easily moved by the wind. Accordingly, the measurements were restricted to the days marked on green in the calendar of the Figure 8-3. The ideal campaign would have been to measure every two weeks to cover the different growing stages of the crops, but the weather conditions during some of these months were not favourable to measure with the GB-SAR [2], especially when the growing speed of the crops was higher during the spring months of April and May.

		April								May				
S	M	T	W	T	F	S	S	M	T	W	T	F	S
			1	2	3	4						1	2
5	6	7	8	9	10	11	3	4	5	6	7	8	9
12	13	14	**15**	16	17	18	10	11	12	13	14	15	16
19	20	21	22	23	24	25	17	18	19	20	21	22	23
26	27	28	29	30			24	25	26	**27**	28	29	30
							31						

		June							July				
S	M	T	W	T	F	S	S	M	T	W	T	F	S
	1	2	3	**4**	5	6				1	2	3	4
7	8	9	10	11	12	13	5	6	7	8	9	10	11
14	**15**	16	17	18	19	20	12	13	14	15	16	17	18
21	22	**23**	24	25	26	27	19	20	21	22	23	24	25
28	**29**	30					26	27	28	29	30	**31**	
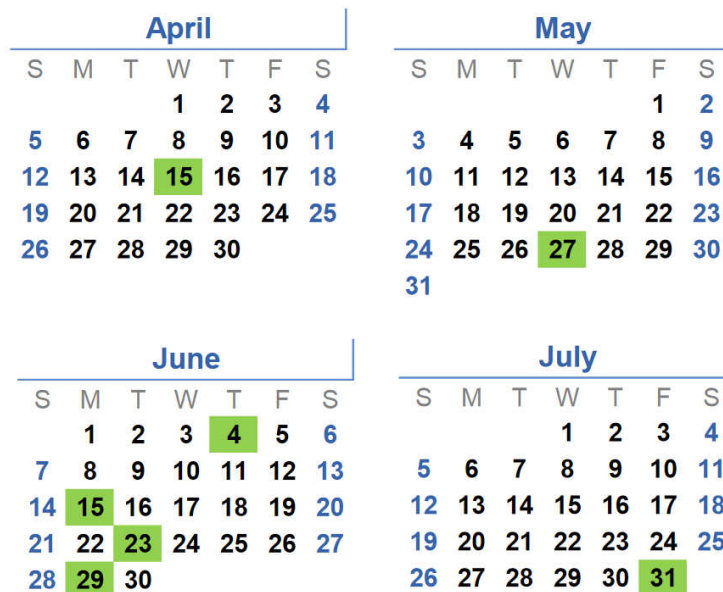
Figure 8-3: On green, days when radar measurements were done during the campaign.

In support of the SAR and TP imagery, measurements of trihedrals and dihedrals on site were also performed on each day to calibrate the system. In order to cover the specifications of the projects and the needs of the partners of the project, different frequencies and polarizations were used. Table 8-1 gathers together the different measurements performed during this campaign.

Day	Type	Band / Frequencies	Polarization
15/04/2015	SAR	X / 8-12 GHz	VV, VH, HH
		Ku / 9-20 GHz	VV, VH, HH
	TP	X / 8-12 GHz	VV, VH, HH
		Ku / 12-20 GHz	VV, VH, HH
27/05/2015	SAR	X / 8-12 GHz	VV, VH, HH
		Ku / 9-20 GHz	VV, VH, HH
	TP	X / 8-12 GHz	VV, VH, HH
		Ku / 9-20 GHz	VV, VH, HH
04/06/2015	SAR	X / 8-14.5 GHz	VV, VH, HH
		Ku / 13.5-20 GHz	VV, VH, HH
	TP	X / 8-13.5 GHz	VV, VH, HH
		Ku / 13.5-20 GHz	VV, VH, HH
15/06/2015	SAR	X / 8-14.5 GHz	VV, VH, HH
		Ku / 13.5-20 GHz	VV, VH, HH
	TP	X / 8-14.5 GHz	VV, VH, HH
		Ku / 13.5-20 GHz	VV, VH, HH
23/06/2015	SAR	X / 8-14.5 GHz	VV
		Ku / 13.5-20 GHz	VV, VH, HH
	TP	X / 8-14.5 GHz	VV, VH, HH
		Ku / 13.5-20 GHz	VV, VH, HH
29/06/2015	SAR	X / 8-14.5 GHz	VV, VH, HH
		Ku / 13.5-20 GHz	VV, VH, HH
	TP	X / 8-14.5 GHz	VV, VH
		Ku / 13.5-20 GHz	VV, VH
31/07/2015	SAR	X / 8-14.5 GHz	VV, VH, HH
		Ku / 13-20 GHz	VV, VH, HH
	TP	X / 8-14.5 GHz	VV, VH, HH
		Ku / 13.5-20 GHz	VV, VH, HH

Table 8-1: List of the radar measurements performed during the campaign. Only the TP measurements were the subject of study in this thesis.

To cover the frequencies of the table, two sets of antennas were used: X band antennas operating 8 to 14.5 GHz, and Ku low band antennas operating 13.5 to 20 GHz Because of the reference targets used to calibrate, the imagery was only valid over the ranges 8.0-12.5 GHz and 15.5-20 GHz, smaller bandwidths were generally used in the analysis.

To account for the characteristics of the GB-SAR system, a calibration is needed to obtain the calibrated backscatter values necessary for the inter-comparison of radar images acquired with different systems, or with the same system when the data is acquired in different modes or processed with different algorithms. Cables are used to connect the VNA (the radar unit) to the antennas. These cables are shown in green in Figure 8-4 and they add an extra distance to the acquired data by the VNA. If a correction is not applied in this data, the images will show a shift in the distance on the images that does not correspond with the distances in the scene that wants to be processed. In the following paragraphs a description is provided of the steps needed to apply the calibration to the system to obtain correct intensities and spatial placement.
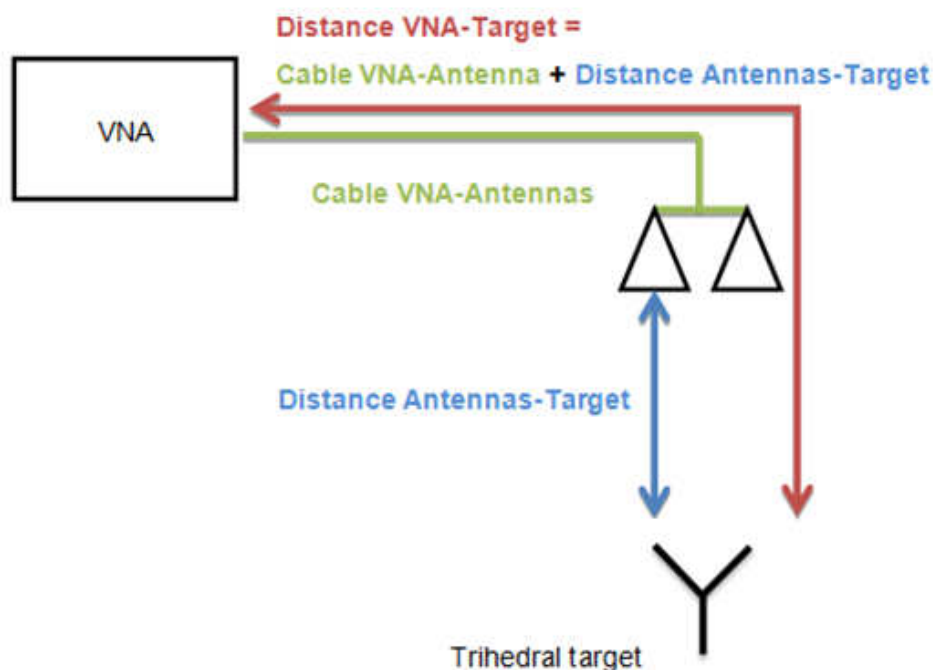
Figure 8-4: Schematic of interconnection between the VNA, antenna cluster and reference target.

One of the most common methods to calibrate radar systems involves the use of metallic trihedrals, spheres, and dihedrals because their returns are well-characterised [17]. The schematic of the Figure 8-5 shows the different steps and the data involved in the calibration of the system.
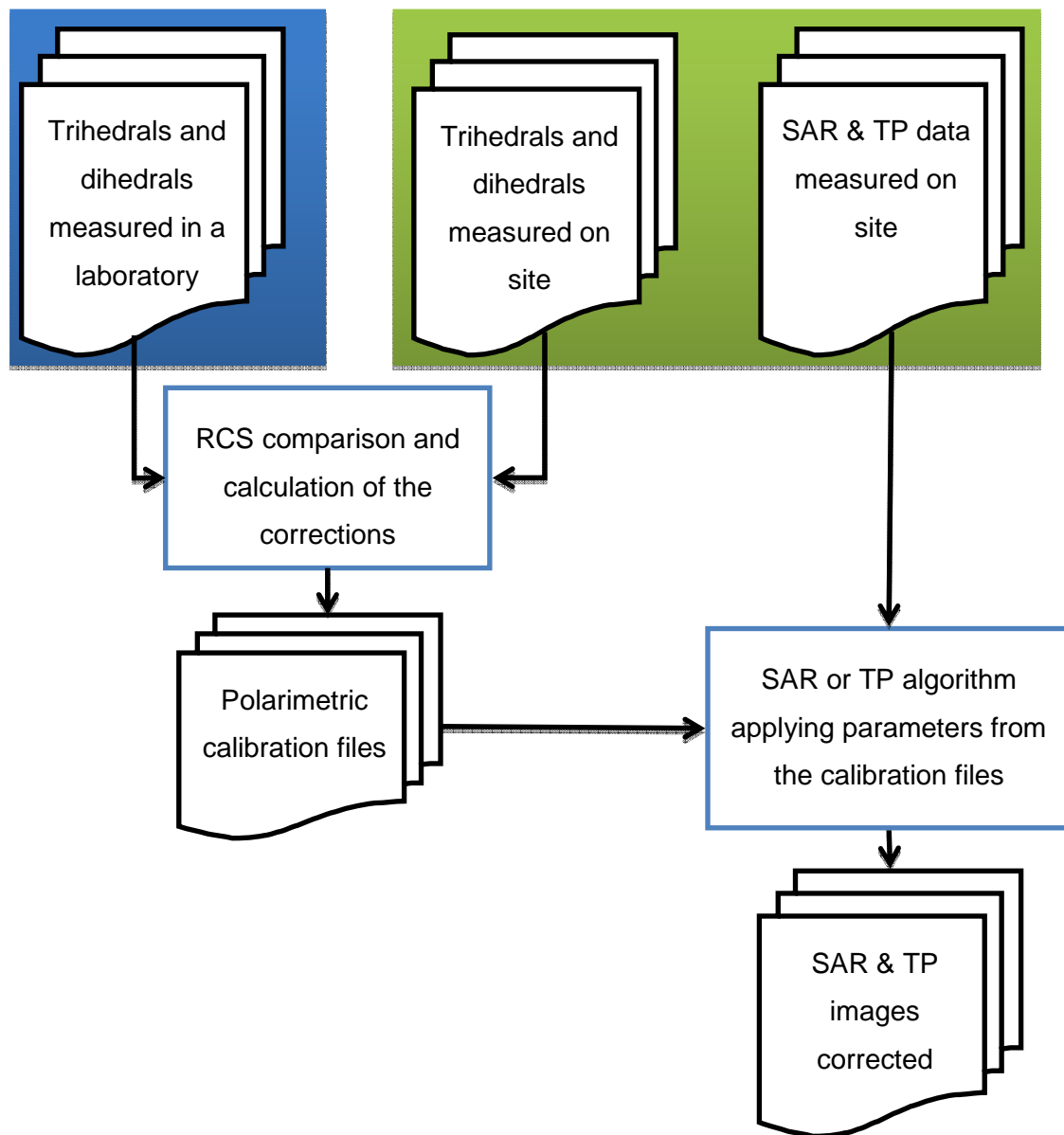
Figure 8-5: Schematic of the calibration procedure.

The reference trihedrals used in the field calibration have previously been absolutely characterised for amplitude and phase response with frequency

against reference 'gold-standard' spheres in the laboratory. Additionally, a strongly depolarising reference target is also measured in the field. An absolute calibration of this is not required as it is referenced to the co-polar trihedral targets. Thus, a calibration data set collected in the field is composed of six different files: reference trihedral, target trihedral, dihedral at 0°, 22.5° and 45°, and a sixth file measuring the empty field without any object below the antennas. Processing proceeds with an initial subtraction of the empty field from each file to remove unwanted clutter. Clutter is further reduced by applying time gates to better isolate just the target returns. The known response of the reference trihedral is used to correct for the non-ideal response of the GB-SAR, and to provide an absolute calibration of the data. The derived reference target response is then used to predict the target trihedral response, which has been previously characterised against the reference trihedral. This provides an error measurement of the calibration process and hence of the imaging process. Because the initial laboratory calibration of the reference trihedrals used in the process was done using a different frequency range, frequency step interval, and number of frequencies, then from the field study, it was necessary to resample them onto a common frequency grid.

8.2.1 Tomographic Profiling images

A set of images with different polarizations and frequencies is provided in this chapter. In order to improve the visualization of the images, the values in the images have been normalized to 0 dB with a dynamic range of 20 dB, 25 dB or 30 dB. In addition to the TP images, a graph with the mean values extracted from the TP images by height has been added to observe the differences between the different polarizations and to compare the images with the status of the crop when measurements were done. Dashed red lines have been added to the images to indicate where the soil level was in each image.

8.2.1.1 Tomographic Profiling: 15th April 2015

Figure 8-6: Tomographic profiling images of the 15/April/2015.

X band (8-12 GHz) with different polarizations: a) HH b) VH c) VV.

Figure 8-7: Tomographic profiling images of the 15/April/2015.

Ku band (15.5-20 GHz) with different polarizations: a) HH b) VH c) VV.
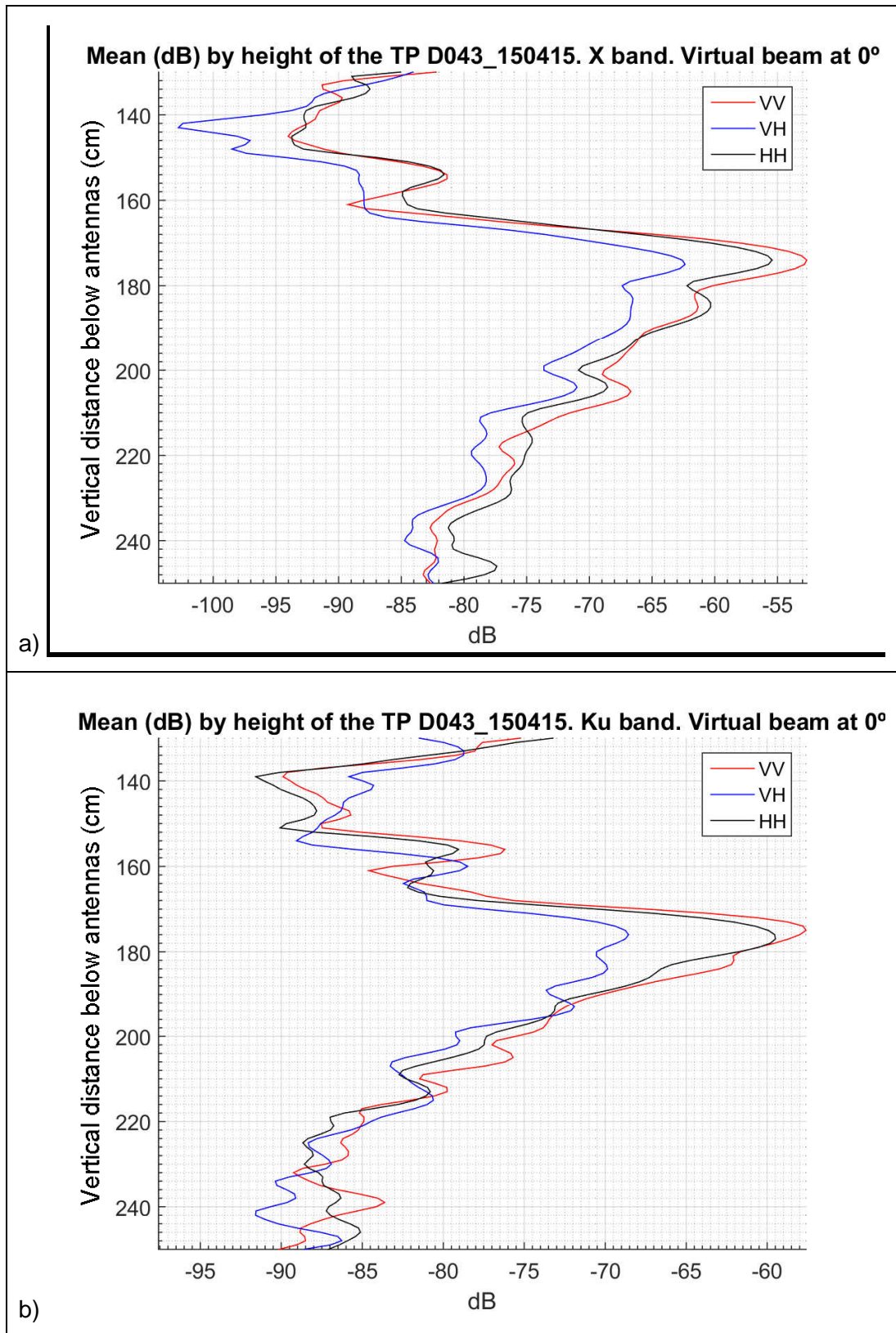
Figure 8-8: Tomographic profiling mean values by height on 15/April/2015.

a) X band 0º b) Ku band 0º.

Figure 8-9: Status of the barley on the 15th of April of 2015 at the farm.

On the 15th of April, the barley on the field was young and it was similar to a grass field with a height of around 10 cm from the soil as shown in Figure 8-9 and the antennas to obtain the TP images were placed at 1.75 m from the soil. The TP images show a big backscattered signal returned from the soil and on the right part of the images it can be seen over the height of the soil the contribution of other non identified objects as shown in Figure 8-10. These objects appear on the image even when they are not under the antenna path due the geometry of the across-track beamwidth. This effect was commented on the chapter 7.1 and illustrated in Figure 7-2b.
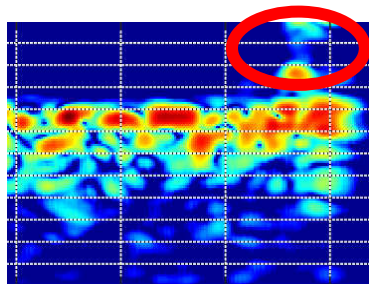
Figure 8-10: Detail of the X band VV TP image. Inside the circle it can be seen imaged some unexpected objects that were not under the antenna path.

8.2.1.2 Tomographic Profiling: 27th May 2015

Figure 8-11: Tomographic profiling images of the 27/May/2015.

X band (8-12 GHz) with different polarizations: a) HH b) VH c) VV.
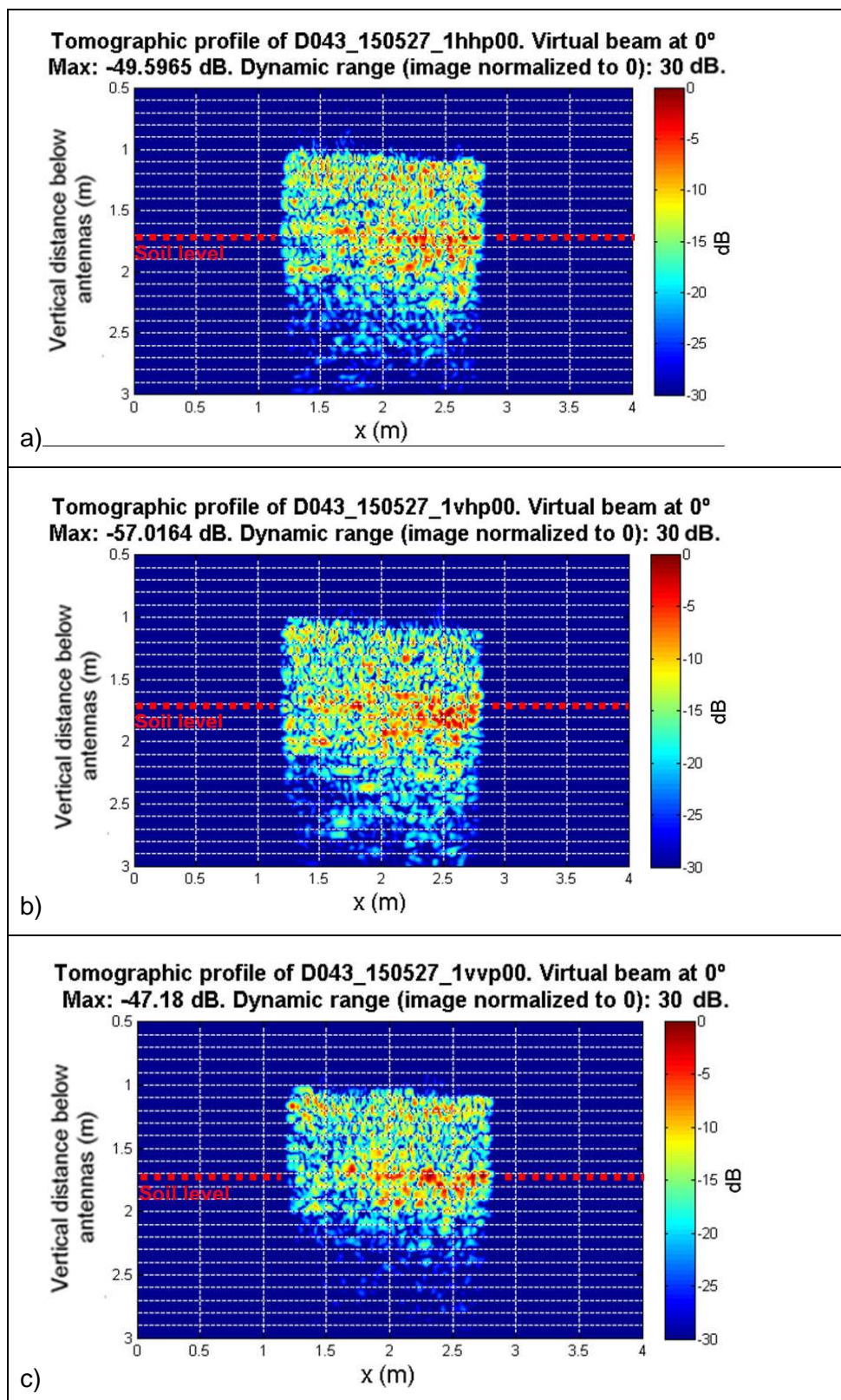
Figure 8-12: Tomographic profiling images of the 27/May/2015.

Ku band (11.5-16.5 GHz) with different polarizations: a) HH b) VH c) VV.
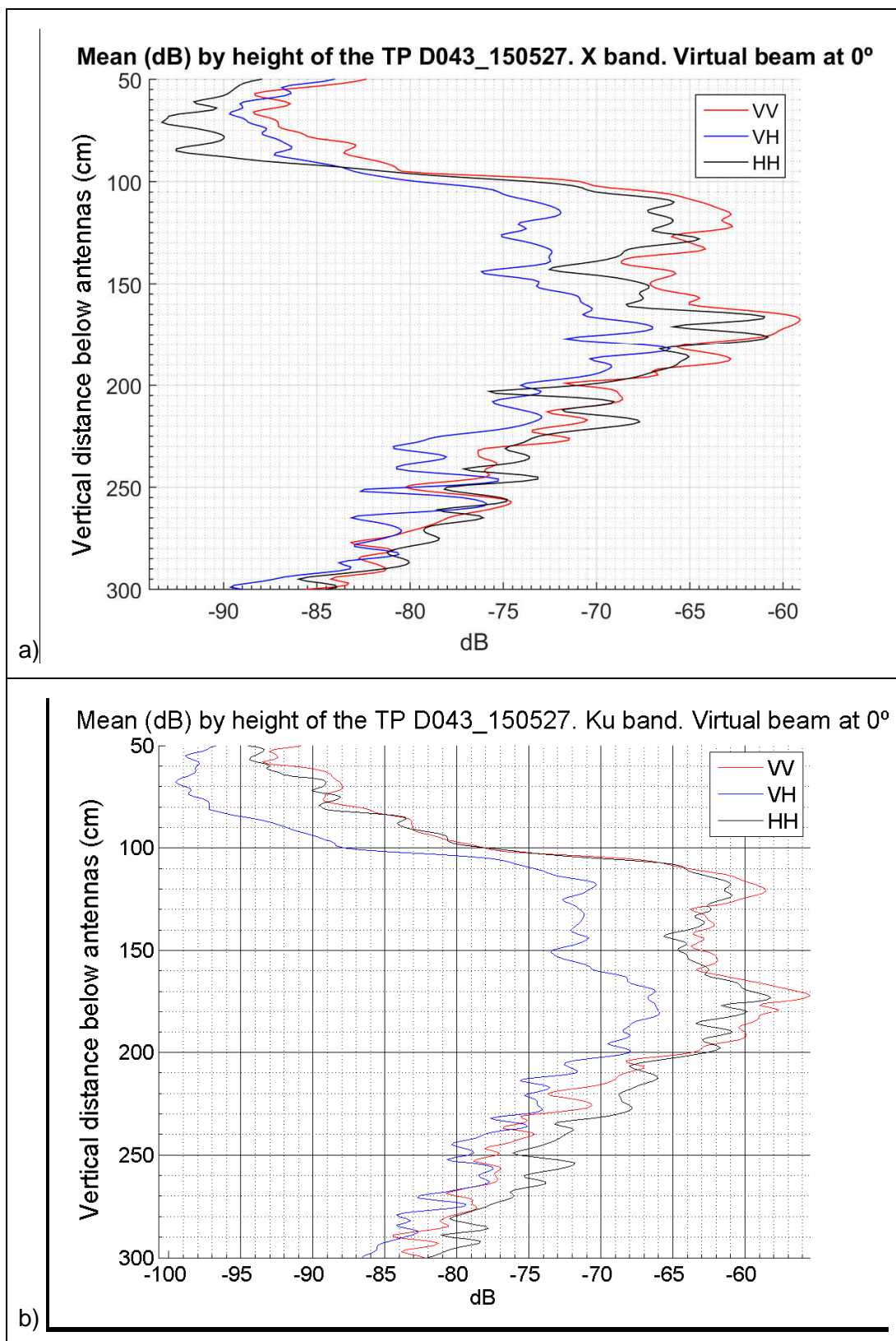
Figure 8-13: Tomographic profiling mean values by height on 27/May/2015.

a) X band 0º b) Ku band 0º.

Figure 8-14: Photograph of a TP scan on the 27/May/2015.

Figure 8-15: Status of the barley on the 27/May/2015.

8.2.1.3 Tomographic Profiling: 04th June 2015
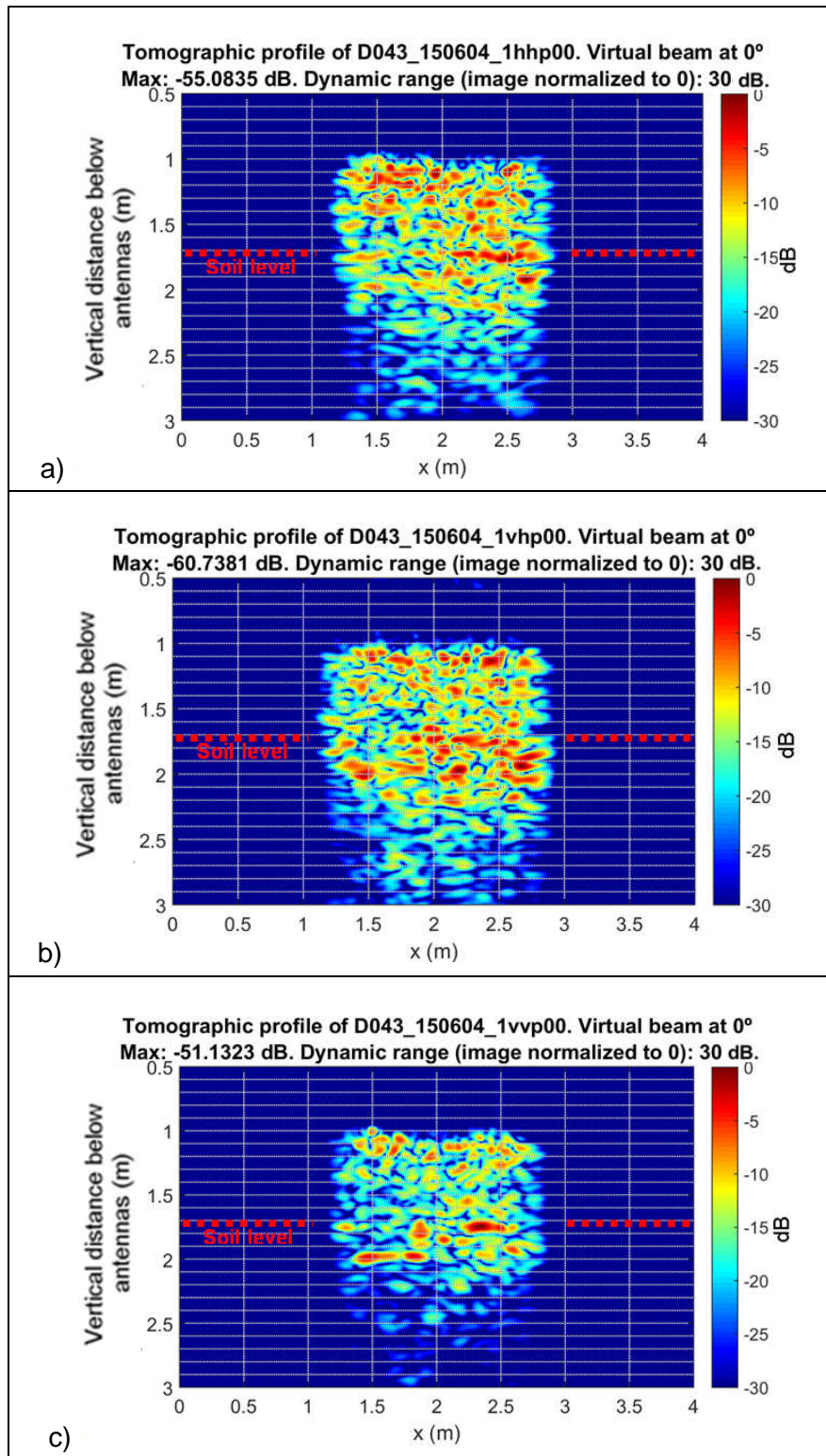
Figure 8-16: Tomographic profiling images of the 04/June/2015.
X band (8-12.5 GHz) with different polarizations: a) HH b) VH c) VV.
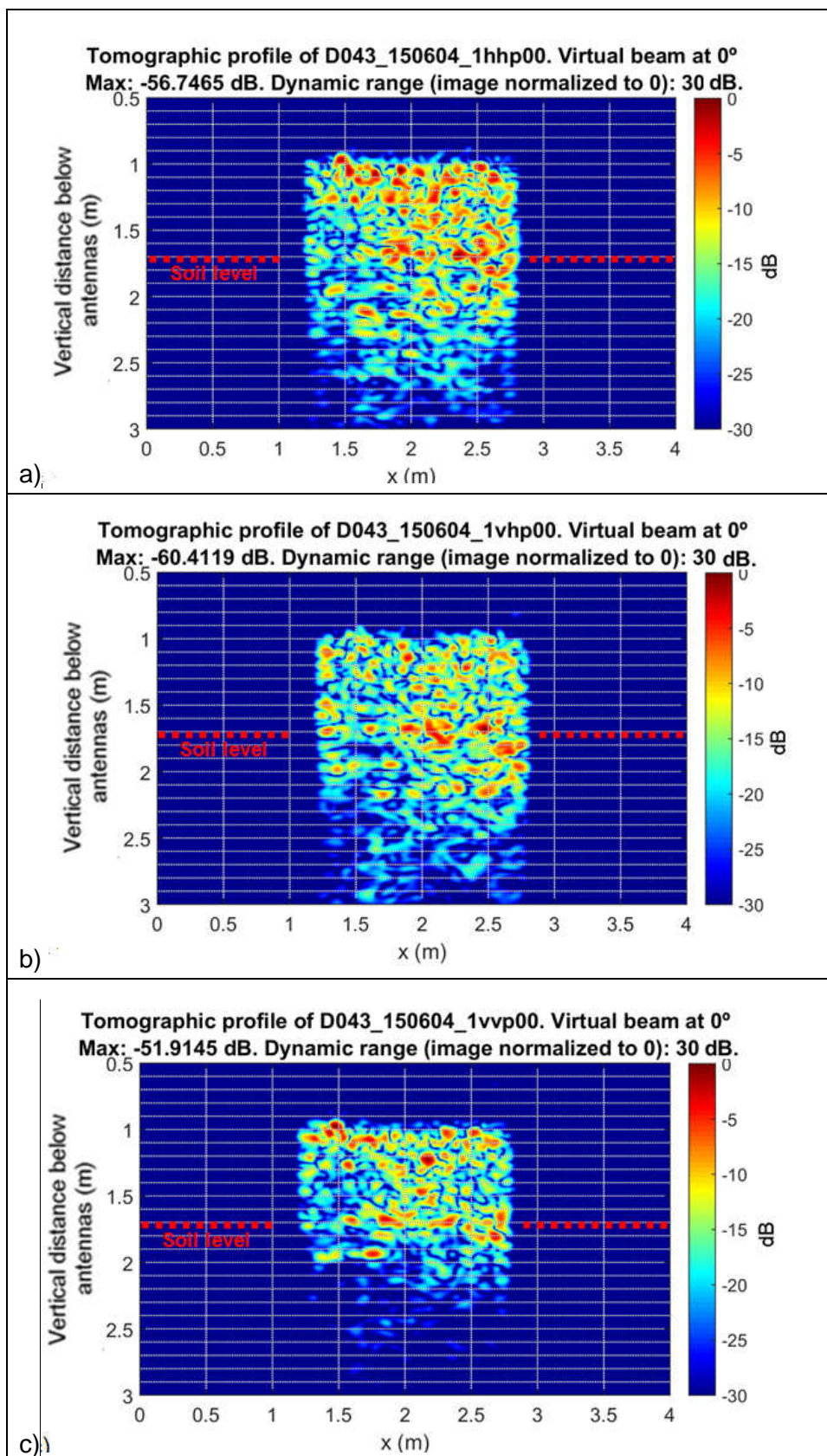
Figure 8-17: Tomographic profiling images of the 04/June/2015.
Ku band (15.5-20 GHz) with different polarizations: a) HH b) VH c) VV.

53
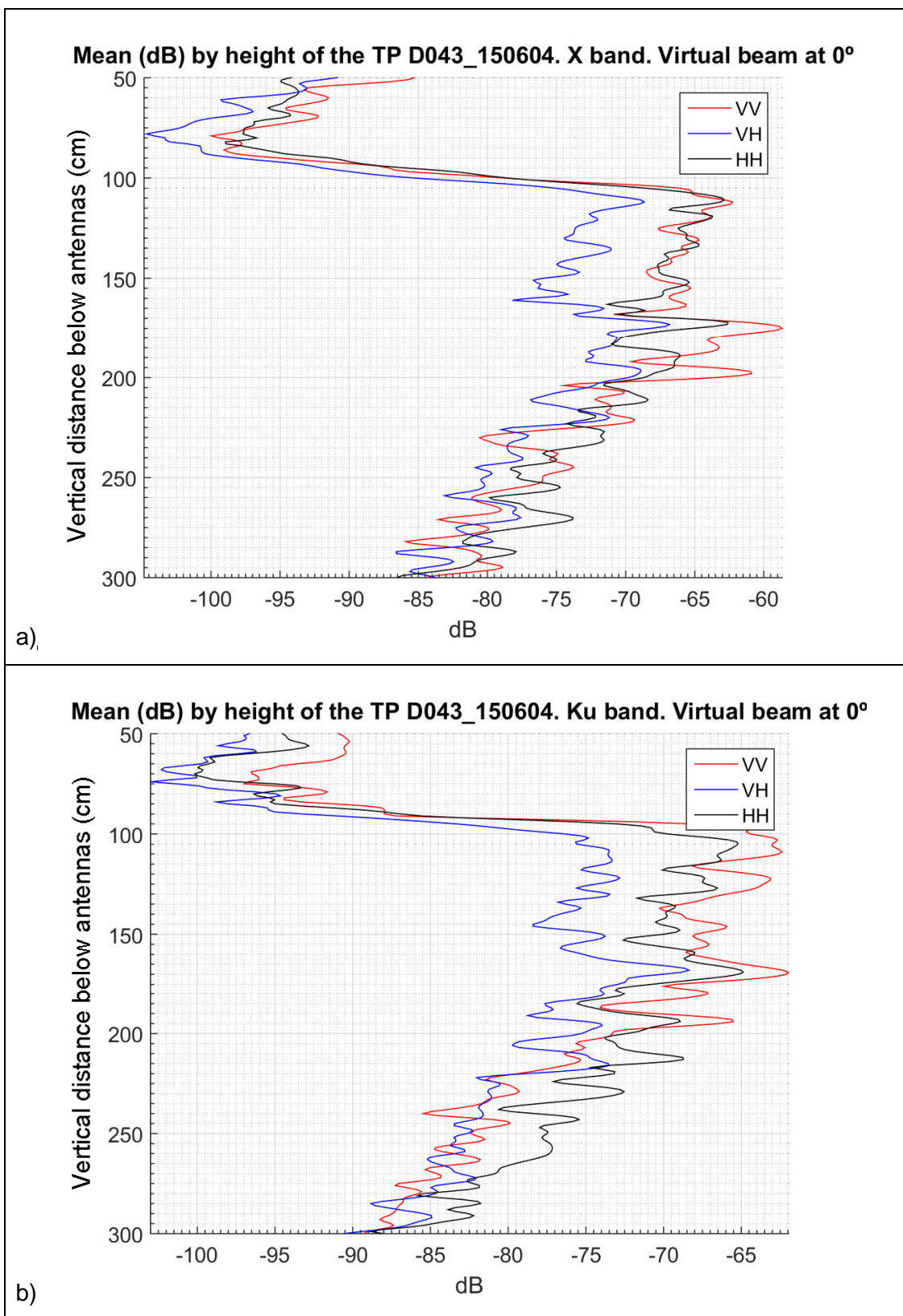
Figure 8-18: Tomographic profiling mean values by height on 04/June/2015.

a) X band 0º b) Ku band 0º.

Figure 8-19: Status of the barley on the 04/06/2015.

8.2.1.4 Tomographic Profiling: 15ᵗʰ June 2015
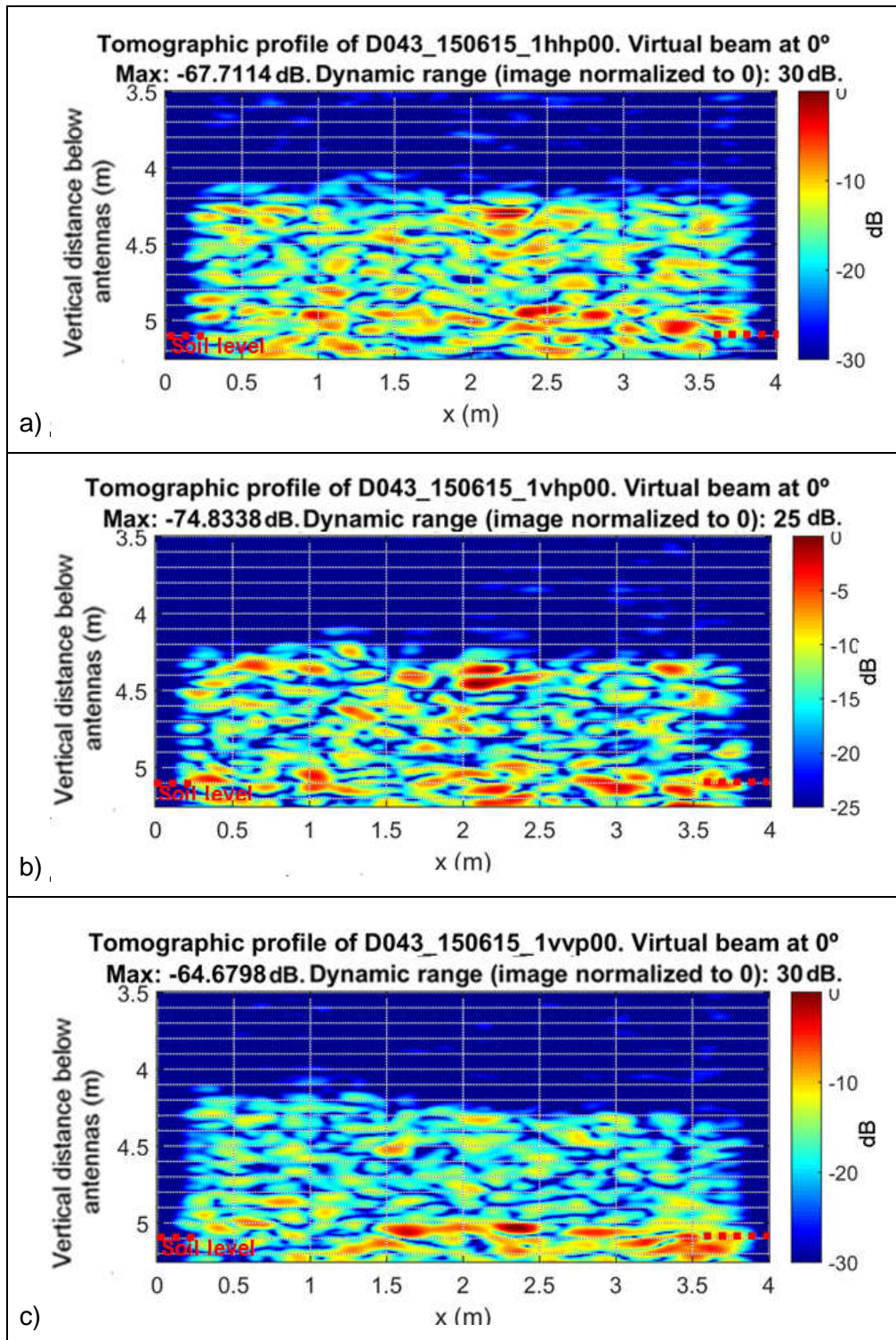
Figure 8-20: Tomographic profiling images of the 15/June/2015.
X band (8-12.5 GHz) with different polarizations: a) HH b) VH c) VV.
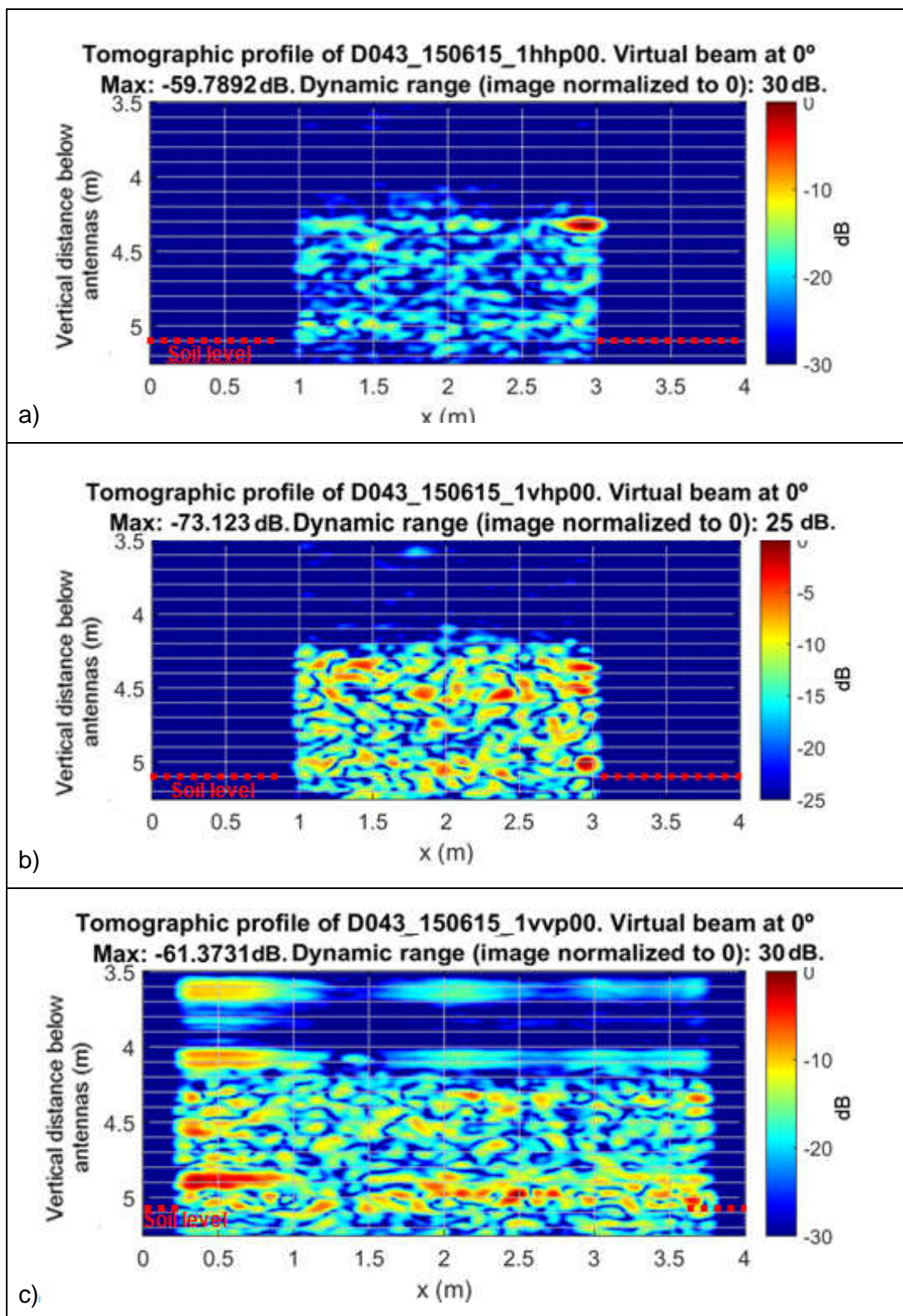
Figure 8-21: Tomographic profiling images of the 15/June/2015. Ku band (15.5-20 GHz) with different polarizations: a) HH b) VH c) VV.
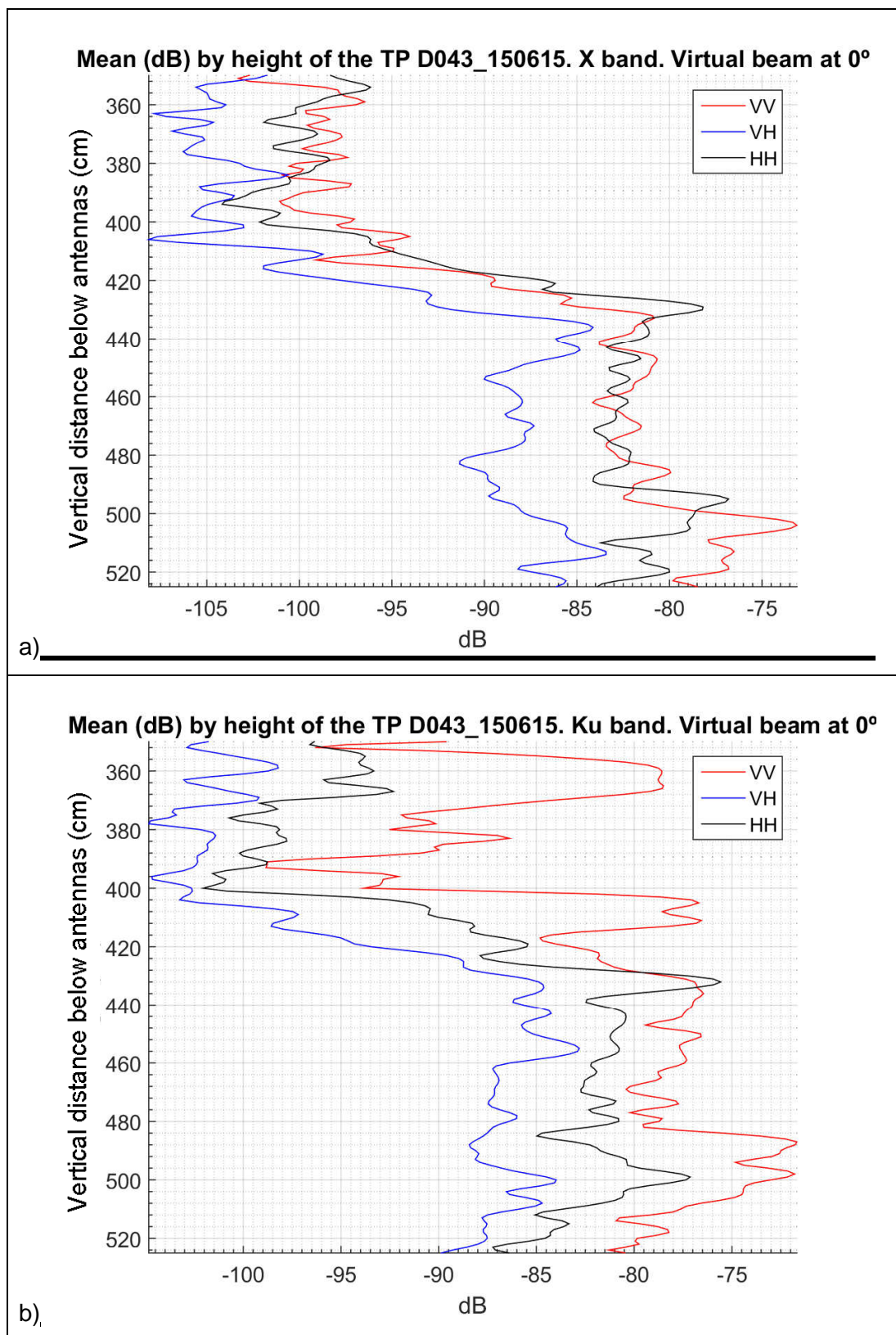
Figure 8-22: Tomographic profiling mean values by height on 15/June/2015. a) X band 0⁰ b) Ku band 0⁰.

Figure 8-23: Status of the barley on the 15/06/2015.

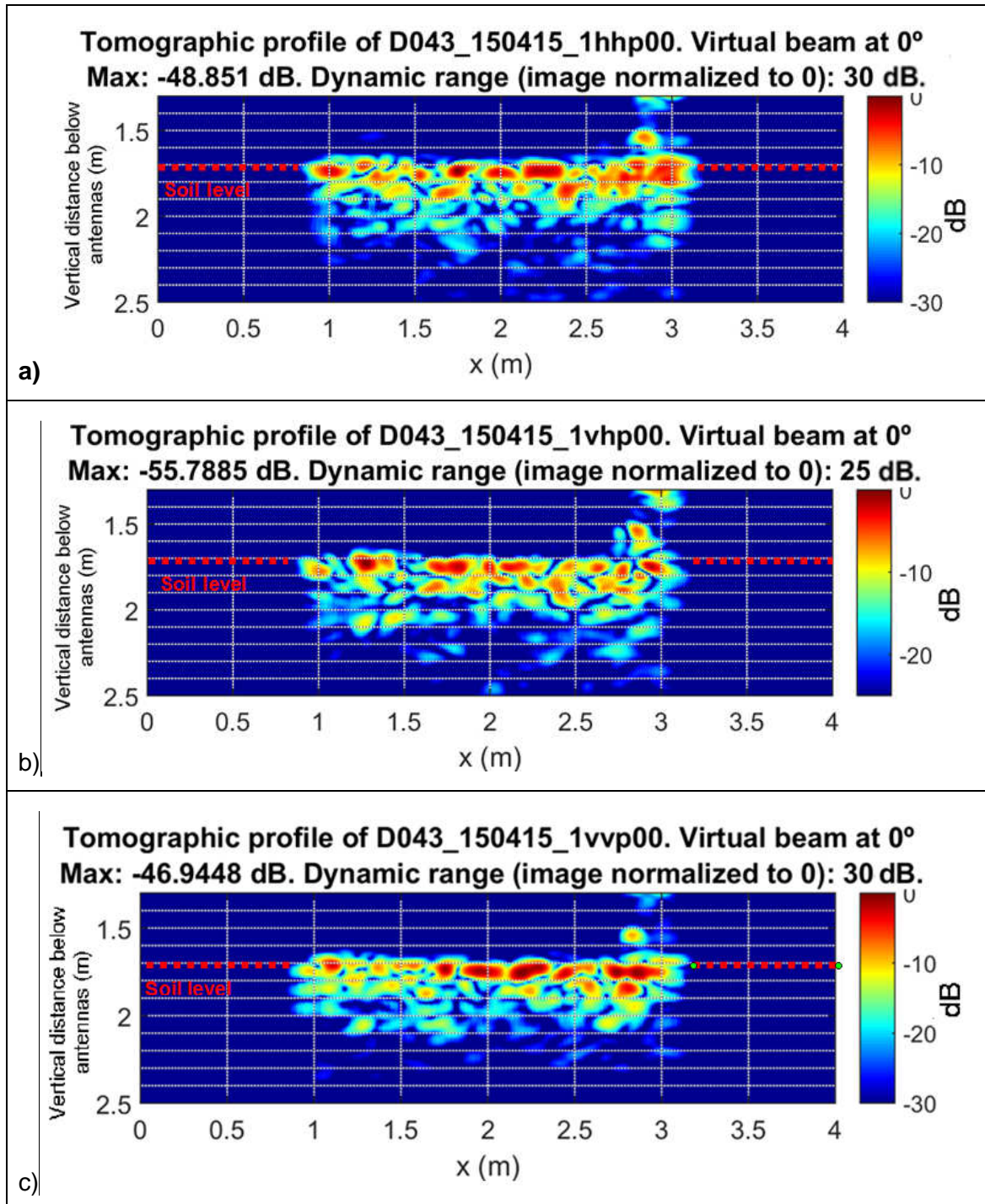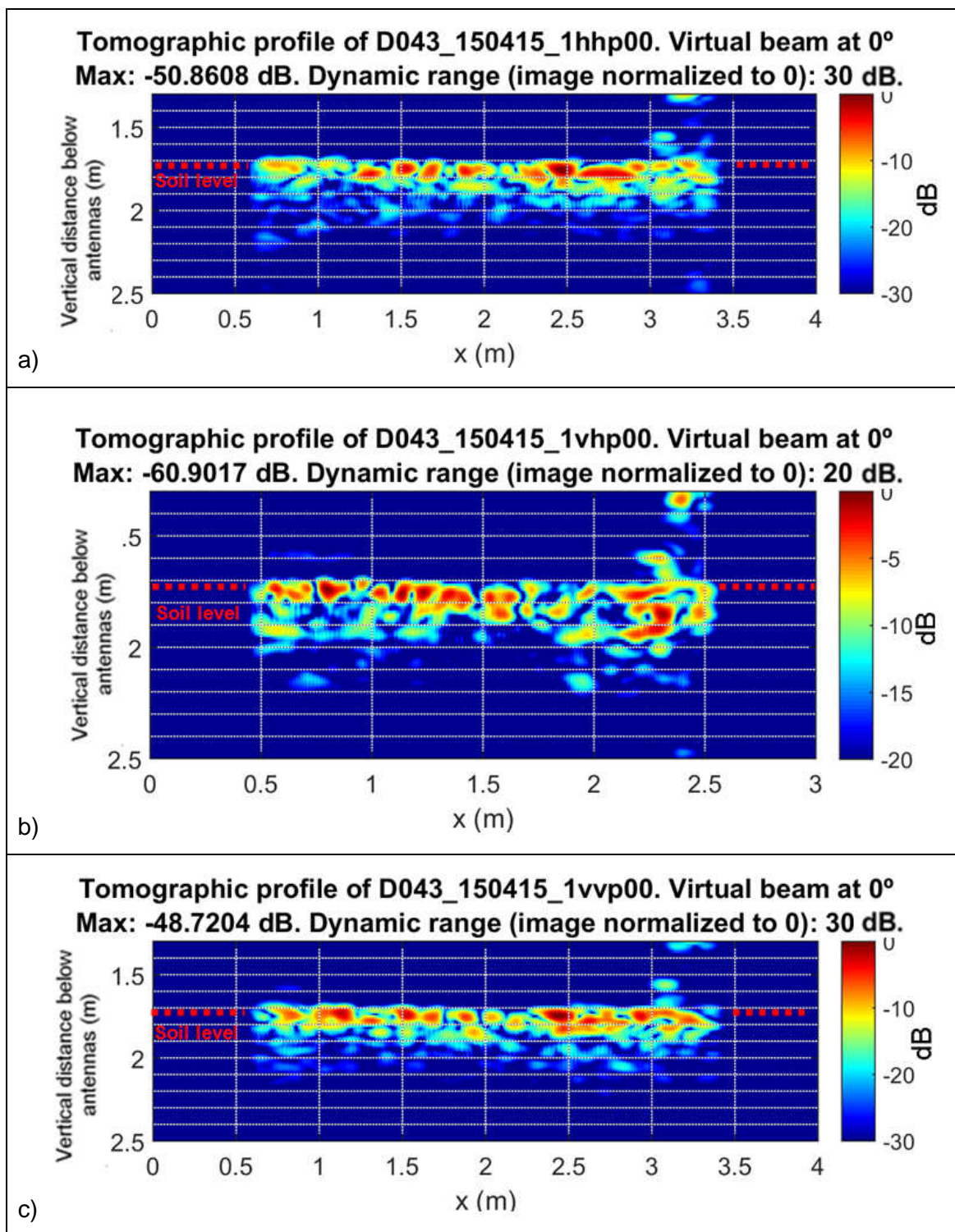## 8.2.1.5 Tomographic Profiling: 23rd June 2015
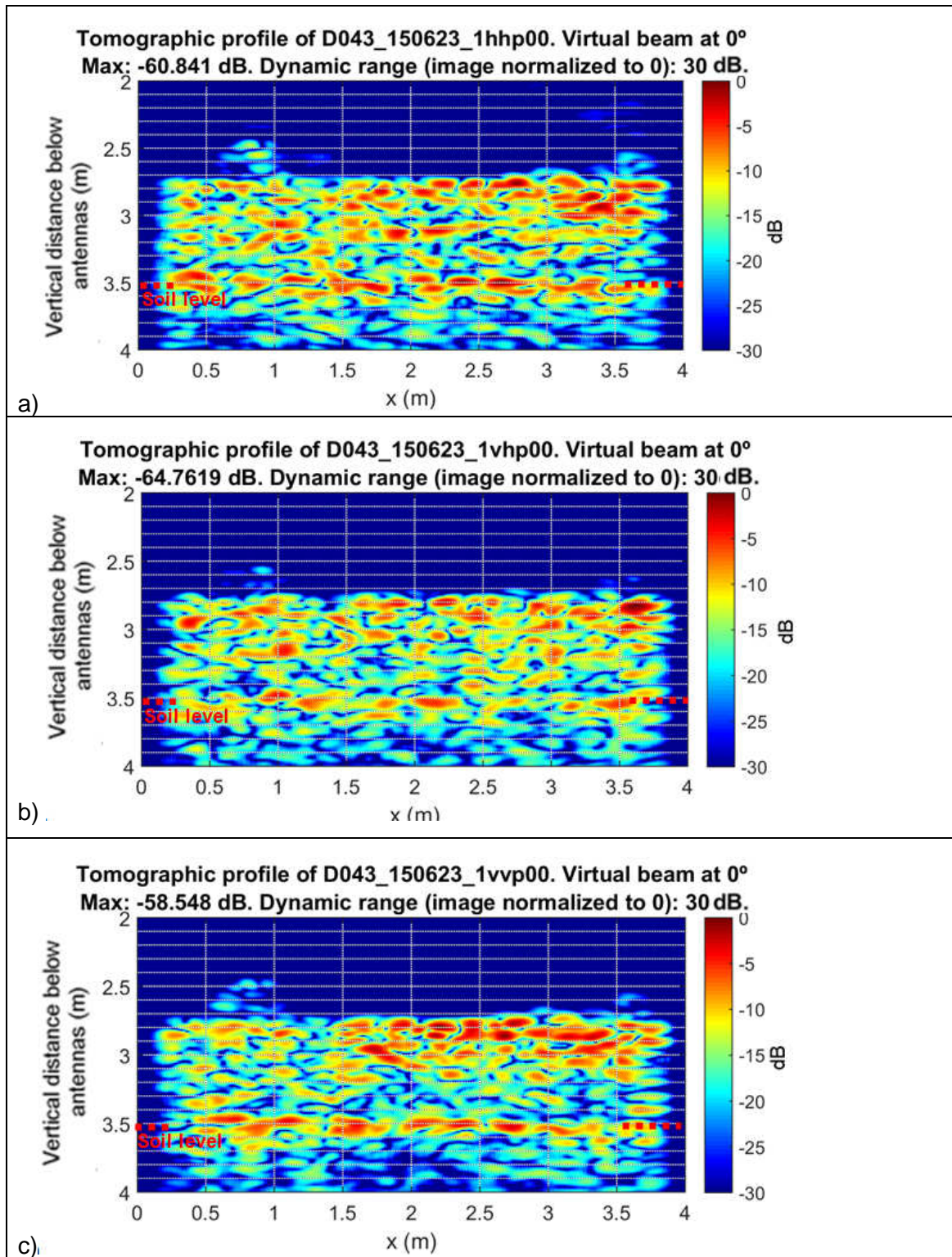
Figure 8-24: Tomographic profiling images of the 23/June/2015.

X band (8-12.5 GHz) with different polarizations: a) HH b) VH c) VV.
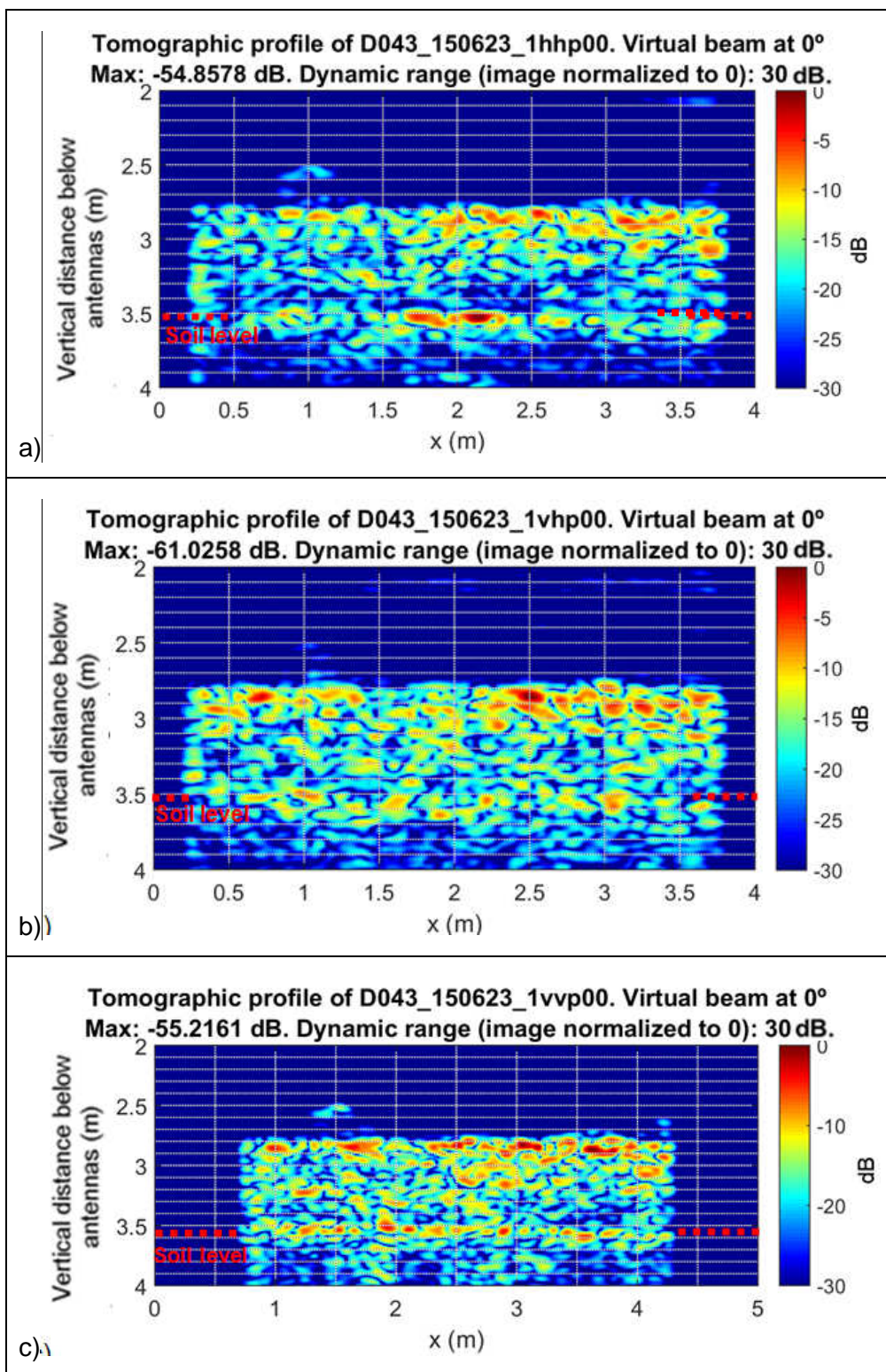
Figure 8-25: Tomographic profiling images of the 23/June/2015. Ku band (15.5-20 GHz) with different polarizations: a) HH b) VH c) VV.

Mean (dB) by height of the TP D043_150623. X band. Virtual beam at 0º

Mean (dB) by height of the TP D043_150623. Ku band. Virtual beam at 0º

a)

b)
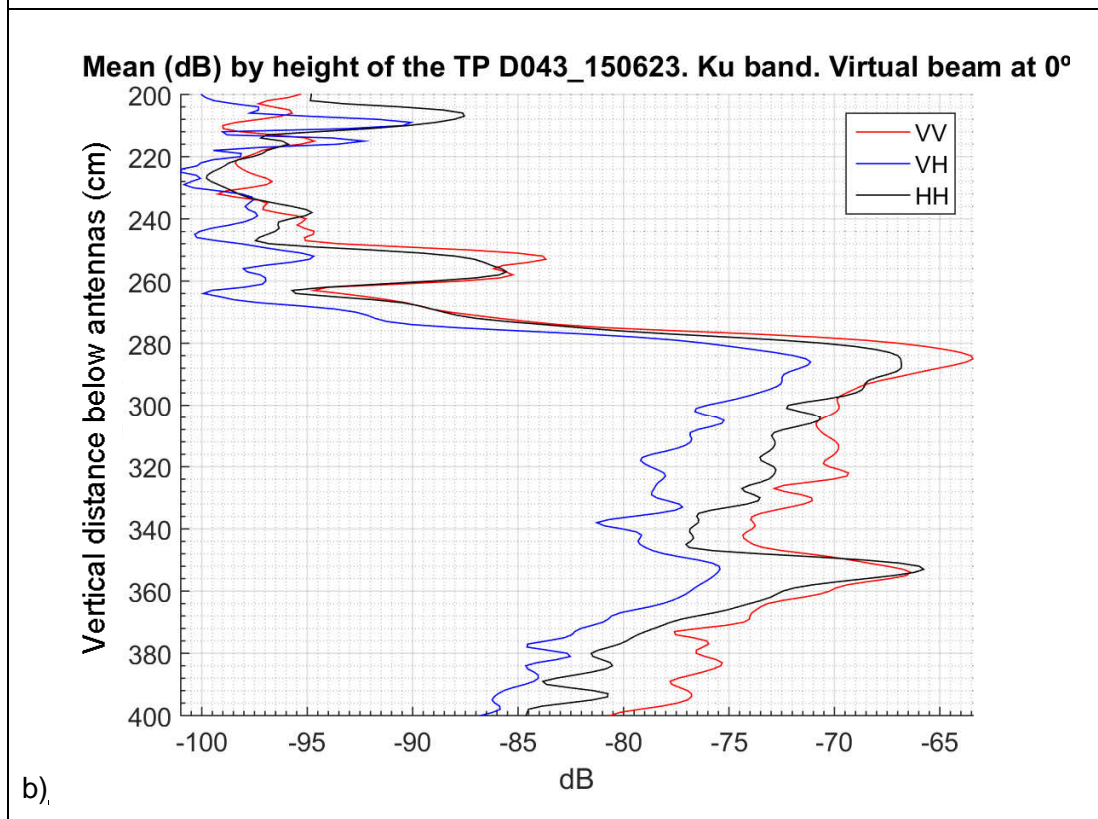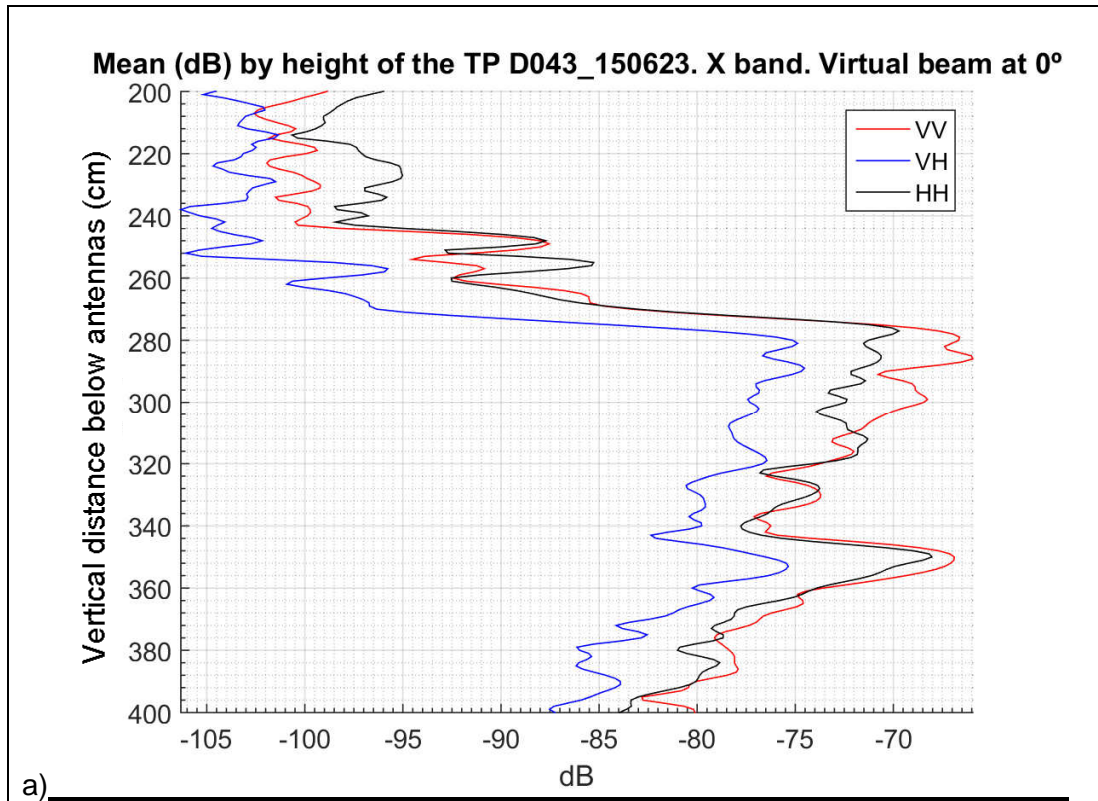
Figure 8-26: Tomographic profiling mean values by height on 23/June/2015.
a) X band 0º b) Ku band 0º.

Figure 8-27: Status of the barley on the 23/06/2015.

8.2.1.6 Tomographic Profiling: 29th June 2015
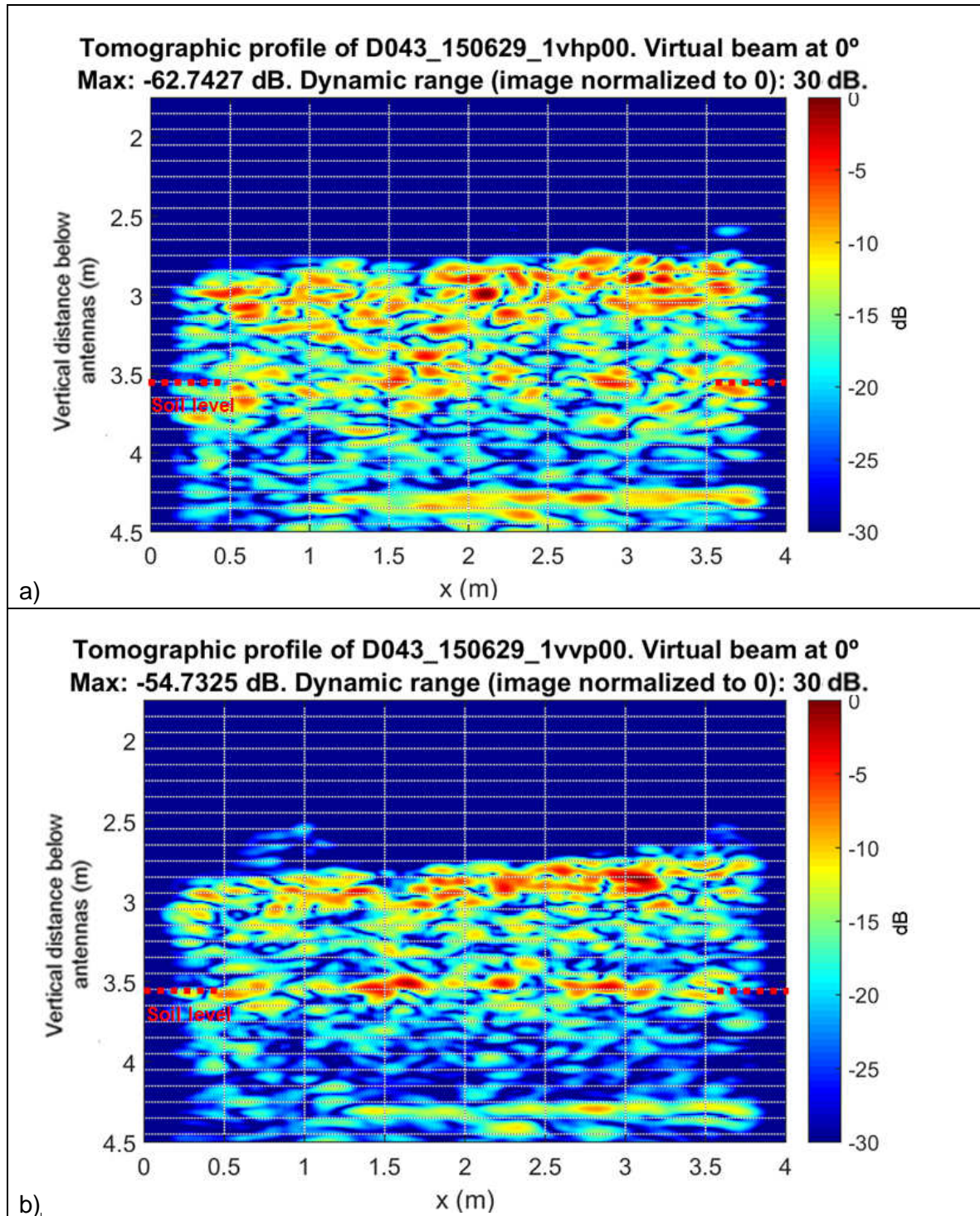
Figure 8-28: Tomographic profiling images of the 29/June/2015.
X band (8-12.5 GHz) with different polarizations: a) VH b) VV.
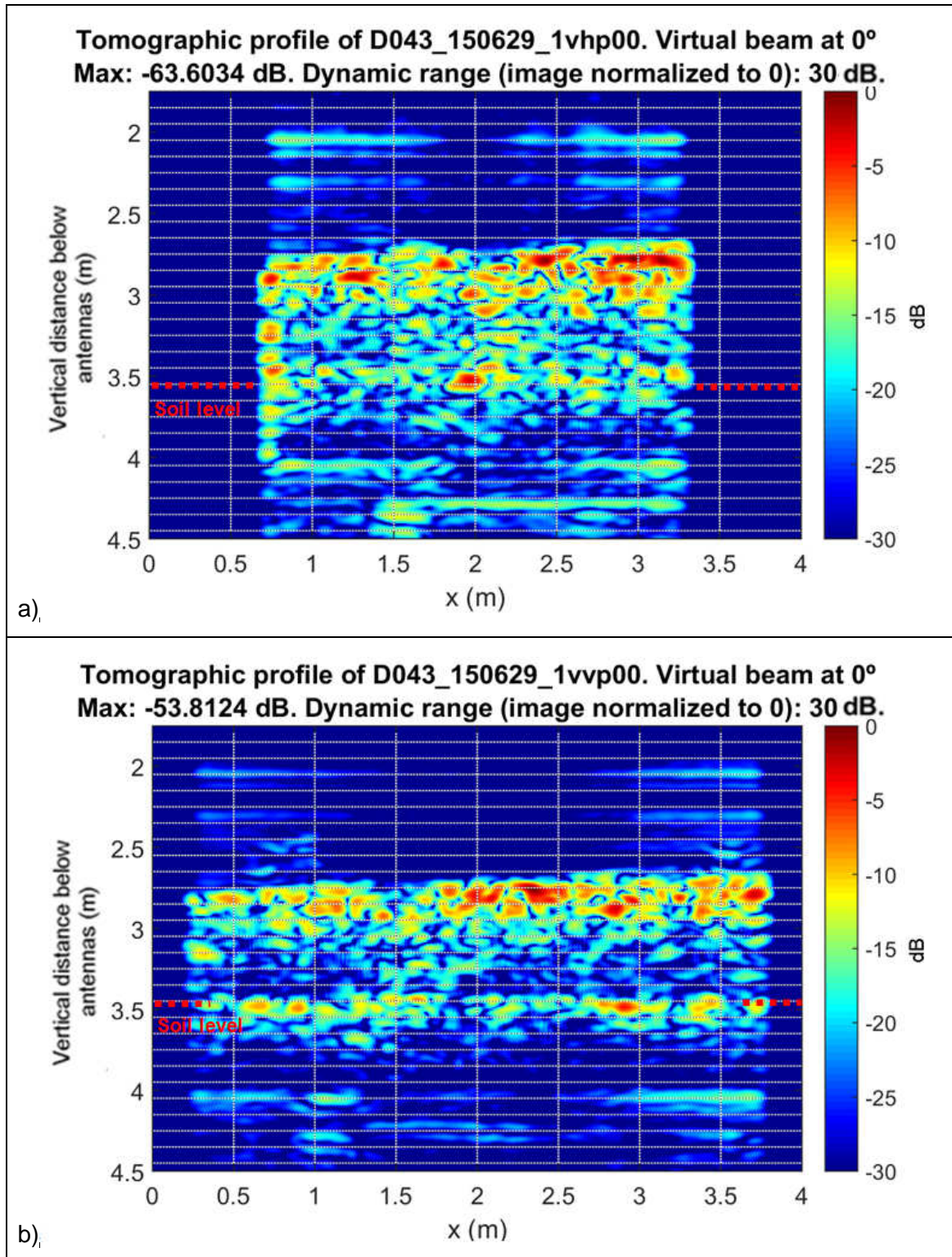
Figure 8-29: Tomographic profiling images of the 29/June/2015.

Ku band (15.5-20 GHz) with different polarizations: a) VH b) VV.
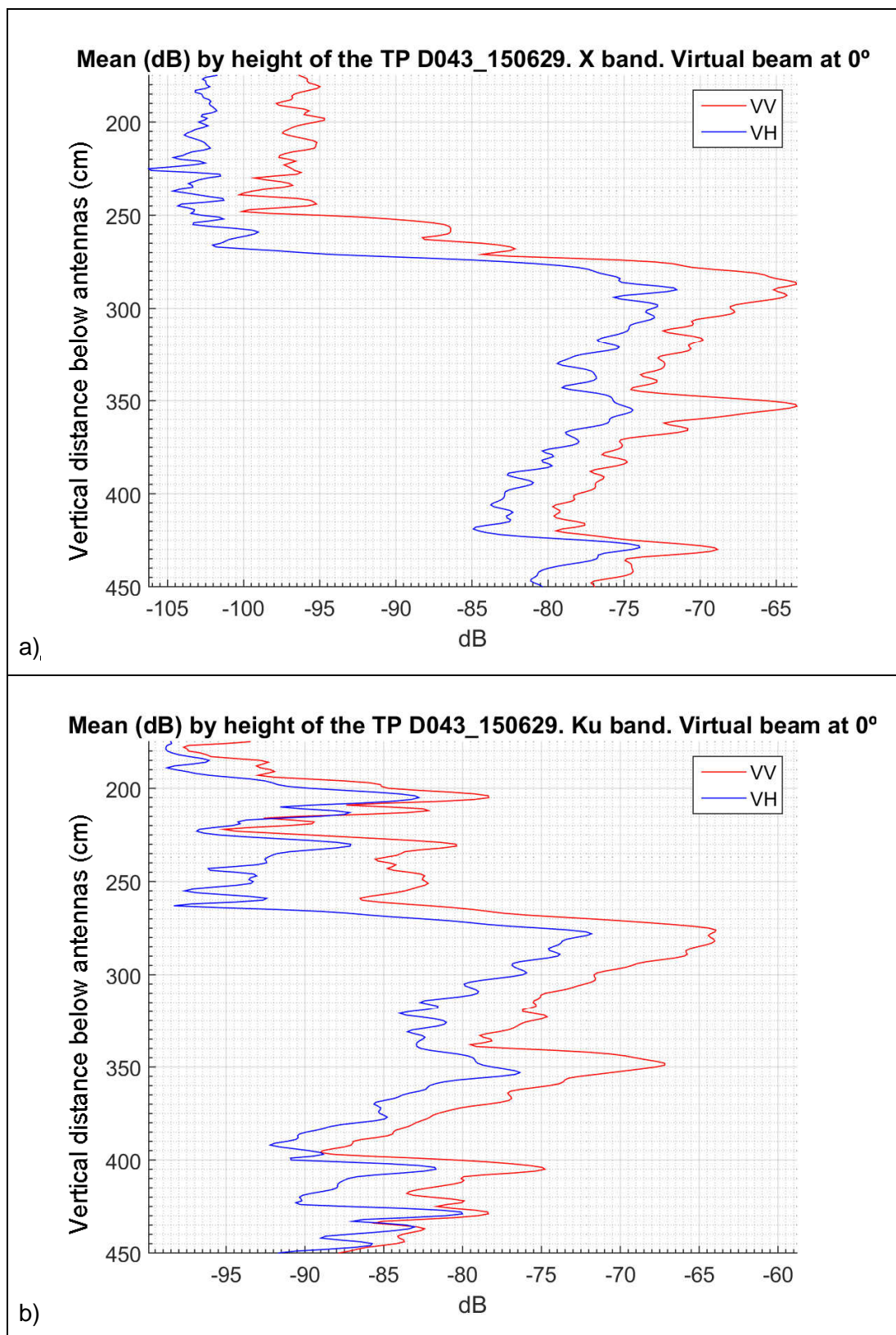
Figure 8-30: Tomographic profiling mean values by height on 29/June/2015.

a) X band 0º b) Ku band 0º.

Figure 8-31: Status of the barley on the 29/06/2015.

8.2.1.7 Tomographic Profiling: 31st July 2015
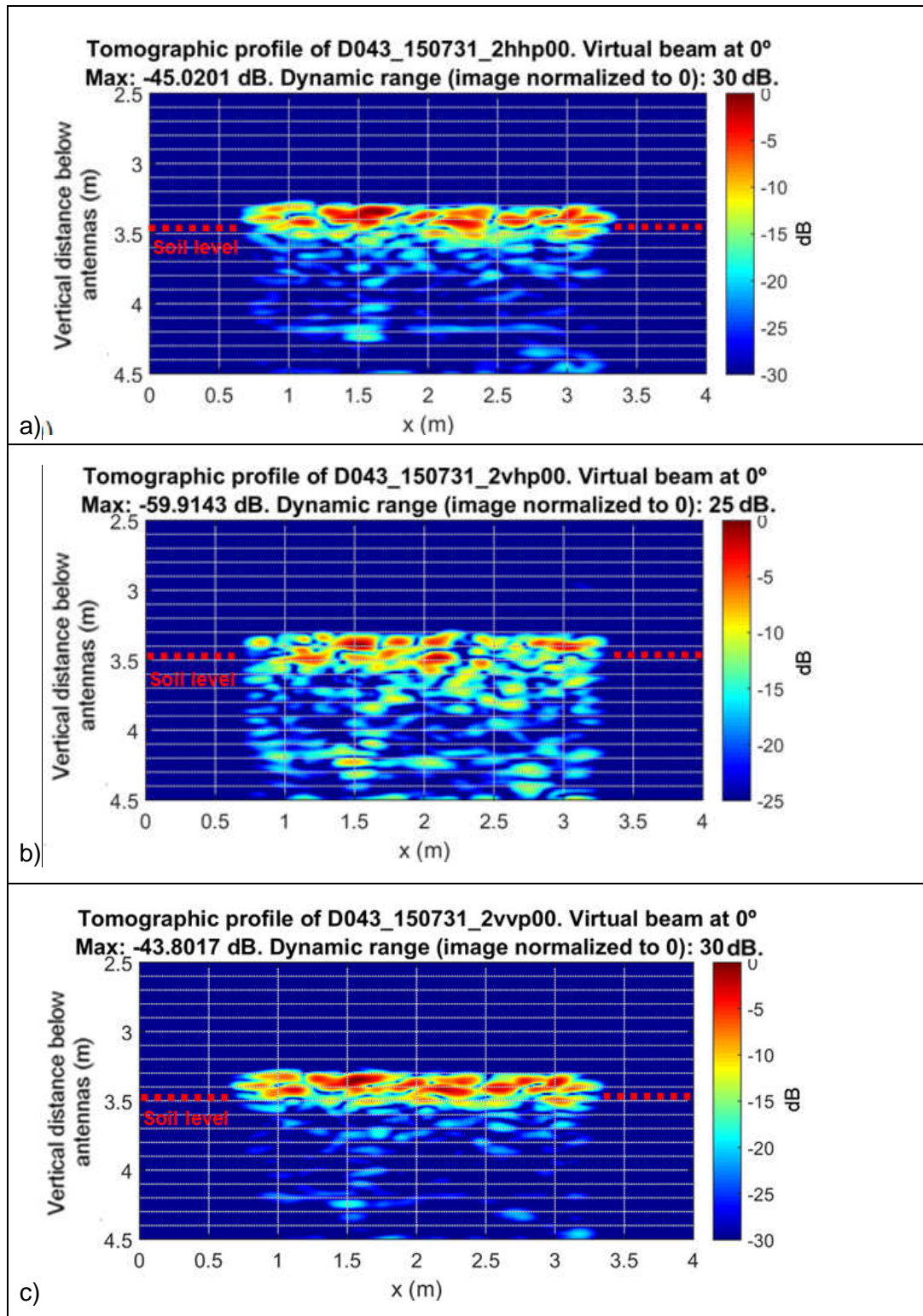
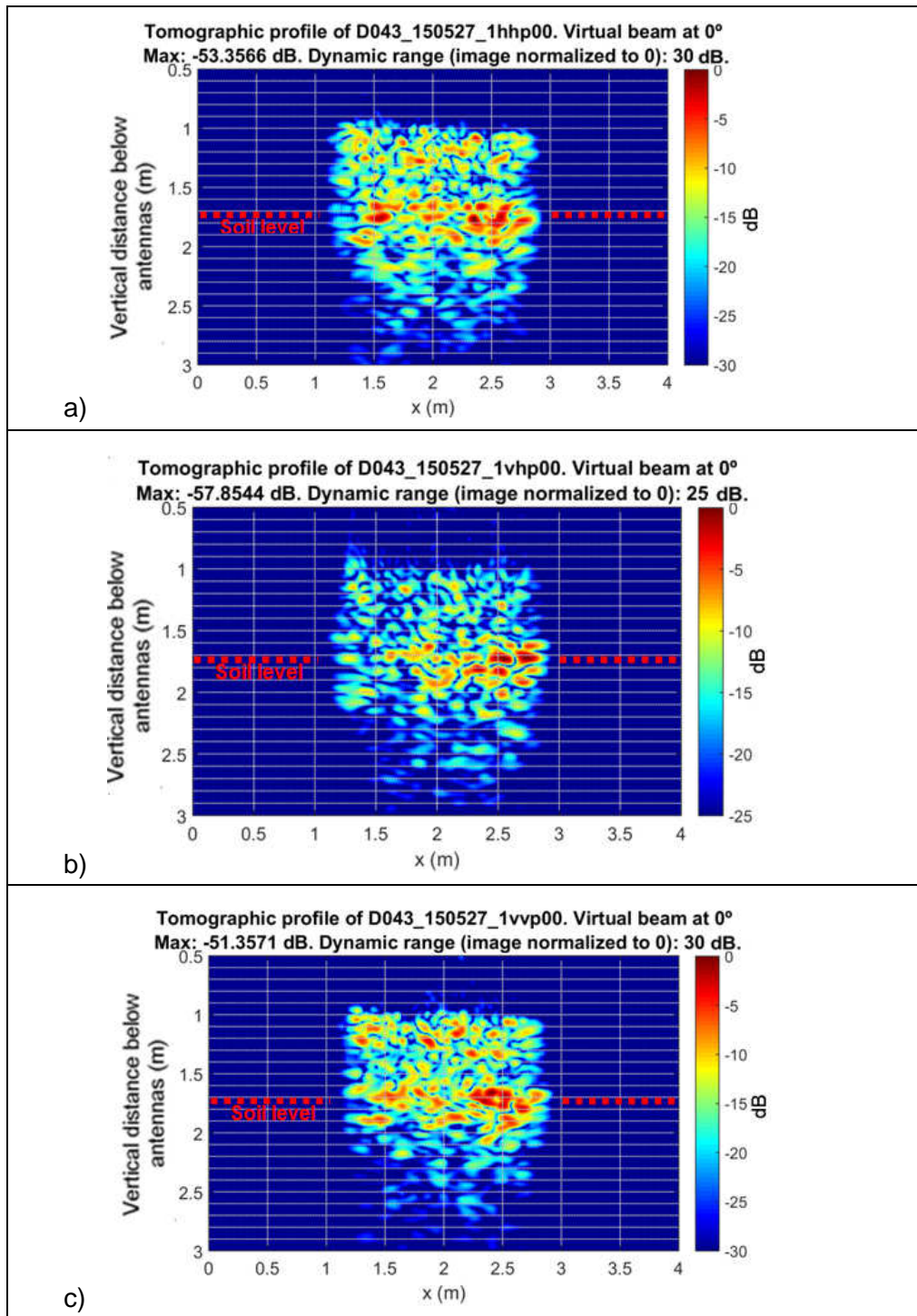**Figure 8-32: Tomographic profiling images of the 31/July/2015 X band (8-12.5 GHz) with different polarizations: a) HH b) VH c) VV.**

**Mean (dB) by height of the TP D043_150731. X band. Virtual beam at 0º**
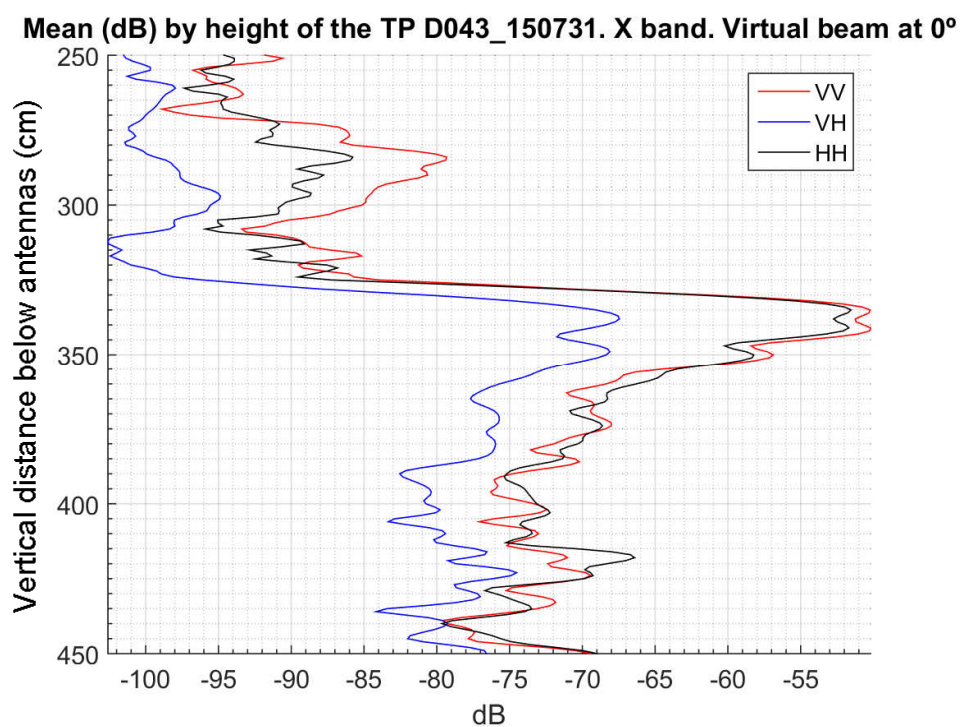
Figure 8-33: Tomographic profiling mean values by height on 31/July/2015. X band 0º.

Figure 8-34: Status of the field on the 31st of July of 2015.

9 Biological field measurements

In this chapter, the characterisation studies of the crop and soil are detailed.

9.1 Soil roughness

A study to obtain the roughness characteristics of the soil has been performed. There are different methods to quantify the soil roughness and previous multiple studies have been published detailing the differences between them [18]-[19]. After studying these different methods, a technique called Structure from Motion (SfM) was selected to measure the soil roughness on a field, as described in [20]. This technique was selected taking into account the economic aspects, the software available to process the images, the complexity of implementation, and the precision of the scheme.

This method consists on generating a digital elevation model (DEM) of an area using specialised software and collection of a set of images of the soil. To generate the DEM, an area of around a 1 x 0.75 m shown in Figure 3-1 was cleared of any vegetation and a set of photographs were taken at different positions and angles to cover the whole area of study.

A set of diverse objects whose dimensions and positions were known, were placed next to the area of study. The size and position of these elements was used as an input to provide distance references to retrieve the correct sizes and position of the complete scene.

Figure 9-1: Area selected to measure the soil roughness. Photograph took on 15th of April of 2015.

A 3D model based on a cloud of points of the same area shown in Figure 9-1 was generated and shown in Figure 9-2b. Once the 3D model has been generated, the cloud of point could be easily extracted to a file with the x, y and z position of each single point of the model. With the position of each point of the 3D model in this file, the different parameters of soil roughness can be calculated.
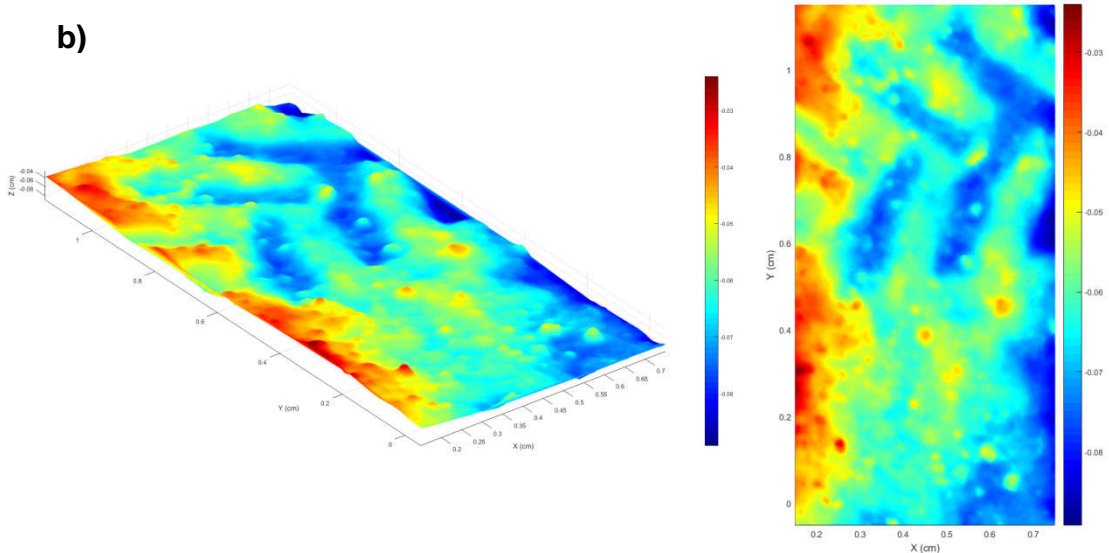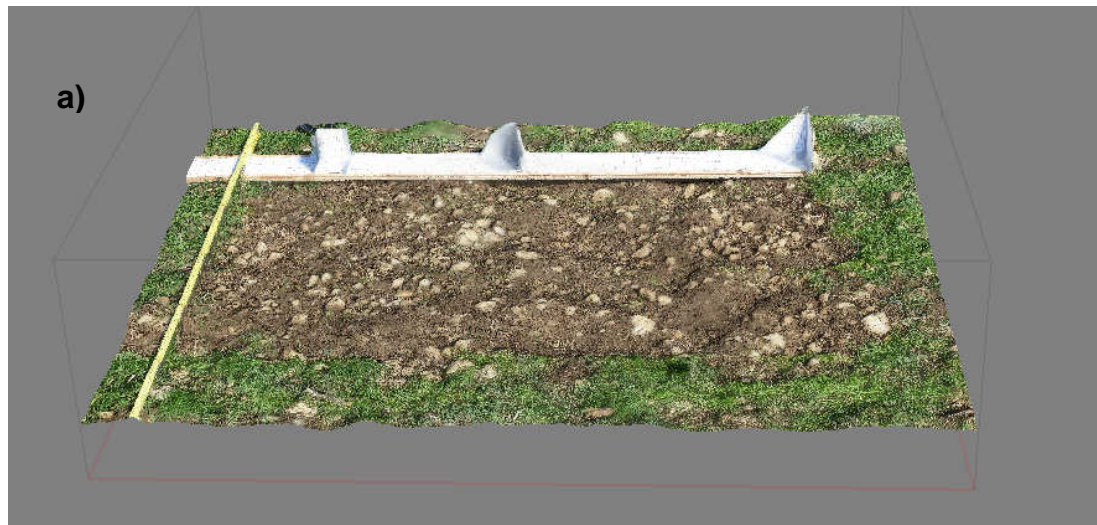
Figure 9-2: a) Cloud of points generated by software of the soil area selected. b) DEM generated of the same area.

Soil roughness, like other natural surfaces, is described by the statistical distribution of the deviation from a certain mean level. The soil roughness of a surface is defined by the RMS (root mean square) height and by the surface correlation length. The RMS height is used to describe the vertical surface roughness and is defined as the standard deviation of the surface height variation in cm as shown in the following equation (9-1).

$$RMS_{height} = \sqrt{\frac{\sum_{i=1}^{n}(z_i - \bar{z})^2}{n-1}} \qquad \text{(9-1)}$$

The surface correlation function $\rho(x)$ and the associated correlation length, ξ, are parameters used for the horizontal description of the surface roughness. In the discrete case, the normalised surface correlation function for a spatial displacement $x' = (j\text{-}1)\Delta x$ is given by.

$$\rho(x') = \frac{\sum_{i=1}^{N+1-j} z_i z_{j+i-1}}{\sum_{i=1}^{N} z_i^2} \qquad \text{(9-2)}$$

Where z_{j+i-1} is a point with the spatial displacement from the point x_i. The surface correlation length is defined as the displacement x' for which $\rho(x')$ between two point inhibits values smaller than 1/e (Eulers's Vale $\approx$ 2.7183).

$$\rho(l) = 1/e \qquad \text{(9-3)}$$

Thus, the surface correlation describes the statistical independence of two points on a surface and increases with the correlation between two neighbouring points. For a perfect smooth surface the value of l is infinite.

The RMS height and the correlation length calculated with the cloud of points obtained on the field are shown in the following two equations.

$$RMS_{height} = 0.0101\ m \qquad \text{(9-4)}$$

$$\xi = 0.12\ m \qquad \text{(9-5)}$$

9.2 Soil moisture

Two hand-held moisture meters have been used to measure the soil moisture of the field every time radar measurements were performed. To get a representative value of the moisture on the field, at least five different measures were done with the moisture meters at random points along the edge of the area imaged without causing disturbance to the crop within it.
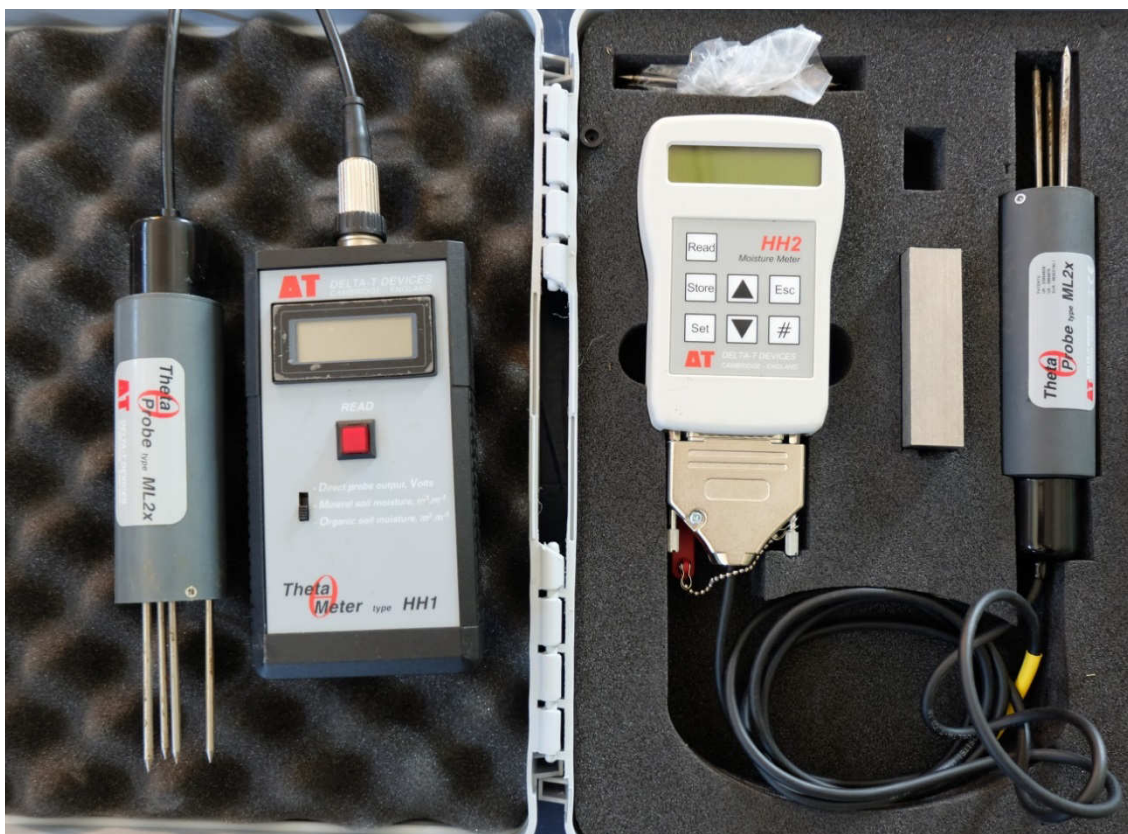
Figure 9-3: HH1 and HH2 moisture meters with ML2x probes of the company Delta-T Devices used to measure the soil moisture.

To measure with these devices, the operator has to set the moisture meters to measure organic soils, then push in the four metal spikes of the probe at the selected point on the soil avoiding rocks, wait for a few seconds to proceed with the measurement and then save the value shown on the screen.

The average soil moisture results during the campaign are presented in the Table 9-1.

Day	Measurements	Average moisture (%)	Standard deviation
15-abr-15	10	27.5	3.3
27-may-15	5	29.1	3.3
04-jun-15	5	24.9	5.4
15-jun-15	6	21.5	6.0
23-jun-15	8	14.2	3.9
29-jun-15	8	14.6	2.0
31-jul-15	6	30.2	6.6

Table 9-1: Average soil moisture.

9.3 Plant moisture

In order to perform a study of the moisture in the vegetation, a representative crop area of 1 m^2 selected randomly was cut each day of the campaign. To select a random area a metallic frame with an internal surface of 1 m^2 was built. This was thrown manually over the crop. The areas selected for this study were chosen outside the region imaged by the radar to avoid any disturbance to the radar images.

Figure 9-4: Selected area to perform the plant moisture study on 27/05/2015.
a) Before collecting the samples. b) Same area after collecting the samples.

Once the plants were cut, they were placed into plastic bags and weighed with a balance. These plants were placed inside an oven at around 60ºC for several days to dry the samples. When dry, the samples were weighed again. The quantity of water inside the plants was obtained by subtracting the weight measured when the samples were completely dried from the weight of the samples after initial cutting on the field.

In addition, a small proportion of the 1 m^2 area selected was separated to perform two more detailed studies on the plants. The first one consisted in separating the leaves and the ears; that is the part of the plant that contains the grains on the top part of the crop in a mature state, of the stalks of at least 25 different plants and weighing the leaves, ears and stalks separately before and after drying them. For the second study, at least another 25 different plants were separated into 10 cm sections from the bottom part of the plants to the top. In the same way, the chopped plants were placed into different bags and

were dried inside the oven. A photograph of each of the separated plant was taken in order to study the size of the plants as explained in the chapter 9.4.

Figure 9-9 shows the state of the crop through the campaign. The clear change in colour can be appreciated, and that indicates visually the moisture change in the plants. The crops changed from a green colour in the first days, to yellow due the loss of moisture in the plants in the last days of the campaign.

Some of these studies were not carried out every day of the campaign because the plants found on the field were still young and their height was too low to perform these studies - leaves and ears that can be clearly distinguished in the senescence, were not present or were making their appearance in these days. Table 9-2 summarizes the studies performed related to plant moisture.

	1 m^2 area	Separation of leaves, stalks and ears in at least 25 plants	Chopped plants each 10 cm
15 April 2015	✓		
27 May 2015	✓	✓	
04 June 2015	✓	✓	✓
15 June 2015	✓	✓	✓
23 June 2015	✓	✓	✓
29 June 2015	✓	✓	✓
31 July 2015	✓		

Table 9-2: Summary of the plant moisture study.

The results of moisture inside the plants in the 1 m^2 study areas can be seen in the Table 9-3, Table 9-4, and Table 9-5.

Day	Samples weight		Water content (g)	Moisture (%)
	Before dry (g)	After dry (g)		
15-Apr-15	692	191	501	72.4
27-May-15	3577	868	2709.0	75.7
04-Jun-15	2966	781	2185	73.7
15-Jun-15	3575	1322	2253.0	63.0
23-Jun-15	3779	1476	2303.0	60.9
29-Jun-15	2919	1373	1546.0	53.0
31-Jul-15	329	203	126.0	38.3

Table 9-3: Table with the moisture of 1 m^2 area measured in the plants.
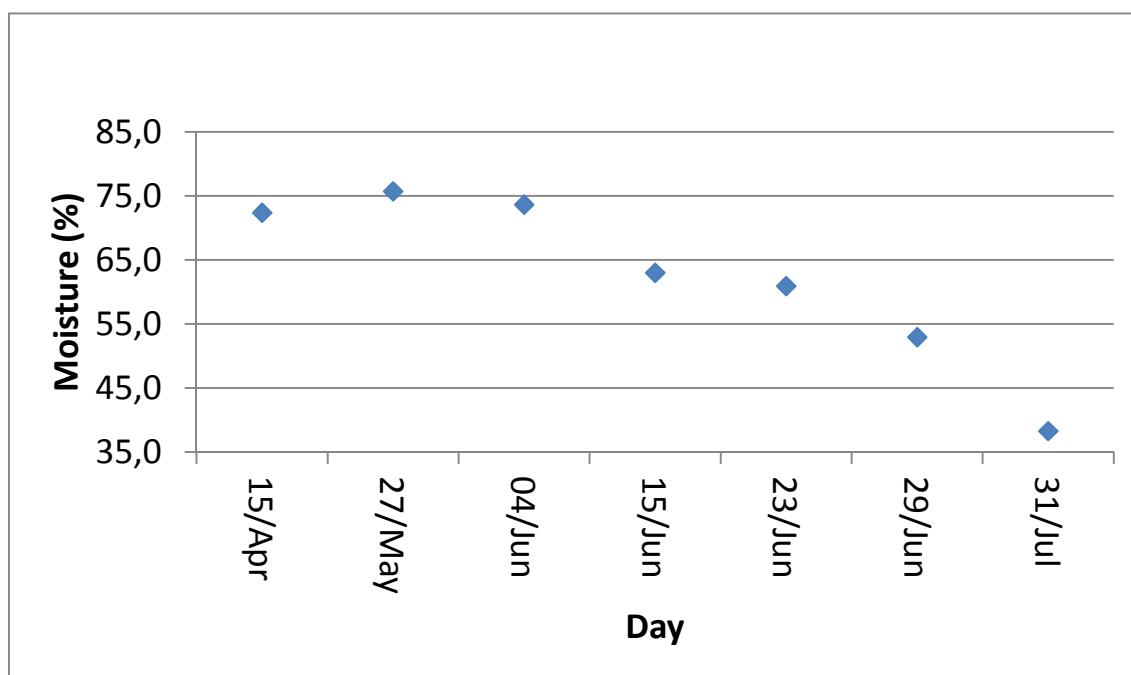
Figure 9-5: Graph of the moisture of 1 m^2 area measured in the plants.

Day	Number of plants	Part of the plant	Samples weight		Water content (g)	Moisture (%)
			Before dry (g)	After dry (g)		
27-May-15	25	Ears	22	8	14	63.6
		Stalks	154	38	116	75.3
04-Jun-15	28	Ears	20	7	13	65.0
		Stalks	67	17	50	74.6
		Leaves	12	4	8	66.7
15-Jun-15	27	Ears	45	16	29.0	64.4
		Stalks	74	29	45	60.8
		Leaves	12	4	8	66.7
23-Jun-15	32	Ears	72	27	45	62.5
		Stalks	80	27	53	66.3
		Leaves	15	4.0	11.0	73.3
29-Jun-15	30	Ears	64	32	32	50.0
		Stalks	44	17	27	61.4
		Leaves	9	5.0	4.0	44.4

Table 9-4: Table with the moisture in the plants by leaves, ears and stalks.
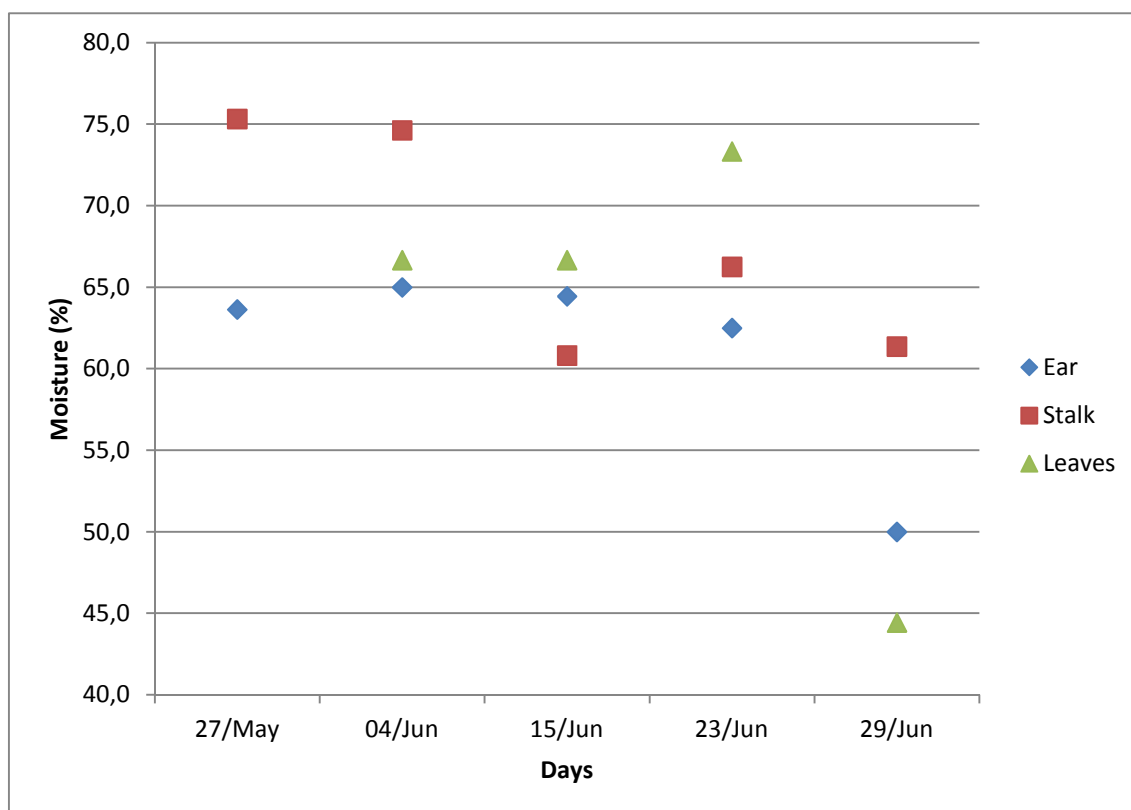
Figure 9-6: Graph with the moisture in the plants by leaves, ears and stalks.

Day	Number of plants	Section	Samples weight		Water content (g)	Moisture (%)
			Before dry (g)	After dry (g)		
04-Jun-15	29	0-10 cm	34	10	24	70.6
		10-20 cm	24	6	18	75.0
		20-30 cm	20	5	15	75.0
		30-40 cm	18	5	13	72.2
		40-50 cm	13	4	9	69.2
		50-60 cm	14	5	9	64.3
		>60 cm	13	4	9	69.2
15-Jun-15	25	0-10 cm	22	9	13	59.1
		10-20 cm	19	8	11	57.9
		20-30 cm	17	7	10	58.8
		30-40 cm	14	6	8	57.1
		40-50 cm	14	6	8	57.1
		50-60 cm	10	4	6	60.0
		>60 cm	44	15	29	65.9
23-Jun-15	26	0-10 cm	23	9	14	60.9
		10-20 cm	17	6	11	64.7
		20-30 cm	15	5	10	66.7
		30-40 cm	14	5	9	64.3
		40-50 cm	14	5	9	64.3
		50-60 cm	12	4	8	66.7
		60-70 cm	16	6	10	62.5
		70-80 cm	37	14	23	62.2
		>80 cm	28	11	17	60.7
29-Jun-15	30	0-10 cm	9	4	5	55.6
		10-20 cm	7	3	4	57.1
		20-30 cm	7	3	4	57.1
		30-40 cm	5	2	3	60.0
		40-50 cm	6	2	4	66.7
		50-60 cm	8	4	4	50.0
		60-70 cm	23	11	12	52.2
		70-80 cm	20	10	10	50.0
		>80 cm	5	3	2	40.0

Table 9-5: Table of the moisture presented in the plants by sections of 10 cm.
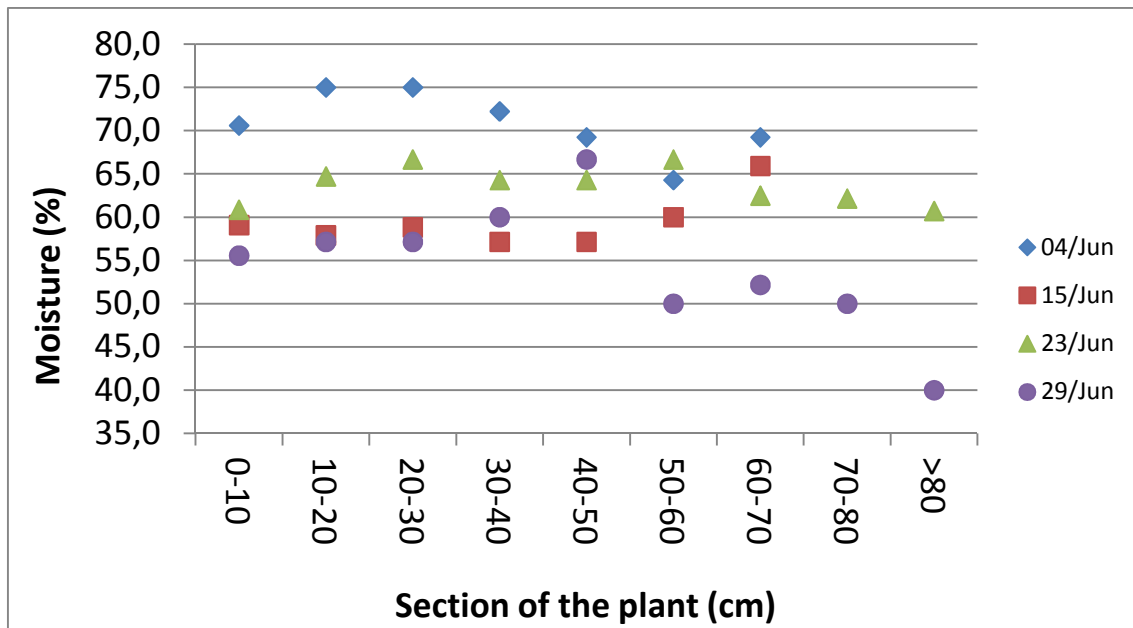
Figure 9-7: Graph of the moisture presented in the plants by sections of 10 cm.

The graph in Figure 9-5 shows a decrease on the moisture of the plants. Around mid-June, a drop of the moisture in the plants was detected coinciding when there are more daily hours of sun per day. In general, according to the data collected and shown in Figure 9-7, the relative distribution of moisture through the plant is constant, except when the plants are in senescence and the moisture level fall in the ears, leaves and the top part or the plants

9.4 Plant size

At the same time that biological samples were collected, a study of the size and characteristics of the crop was performed to see how the radar images change depending on the characteristics and state of the crops every day.

A schematic of the evolution of the crop with its state depending on the date is provided in Figure 9-8. This schematic was useful before starting the campaign and was used as a reference to see the differences in the crops that could be expected in the field.
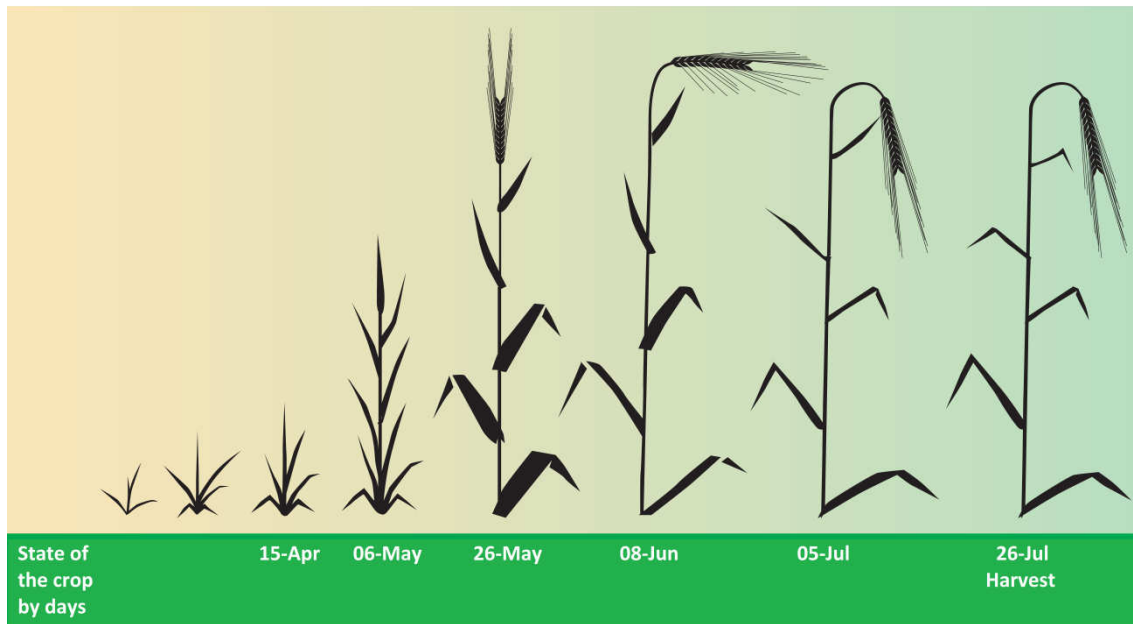
Figure 9-8: Schematic of the state of the crops by dates in UK (image credits: HGCA and SEERAD - Scottish Executive Environment and Rural Affairs Department).

The status of the crops in the previous schematic of Figure 9-8 can be compared with the photographs taken on the field in Figure 9-9, where the different photographs shows the state of the plants each day and the height of the crop with respect to the soil. During the campaign, data was acquired from the first crops on mid-April, when it had the appearance of short grass, to almost its senescence at the end of June when the crop was at its maximum height. The campaign was extended to an additional day at the end of July following a few days after harvesting.
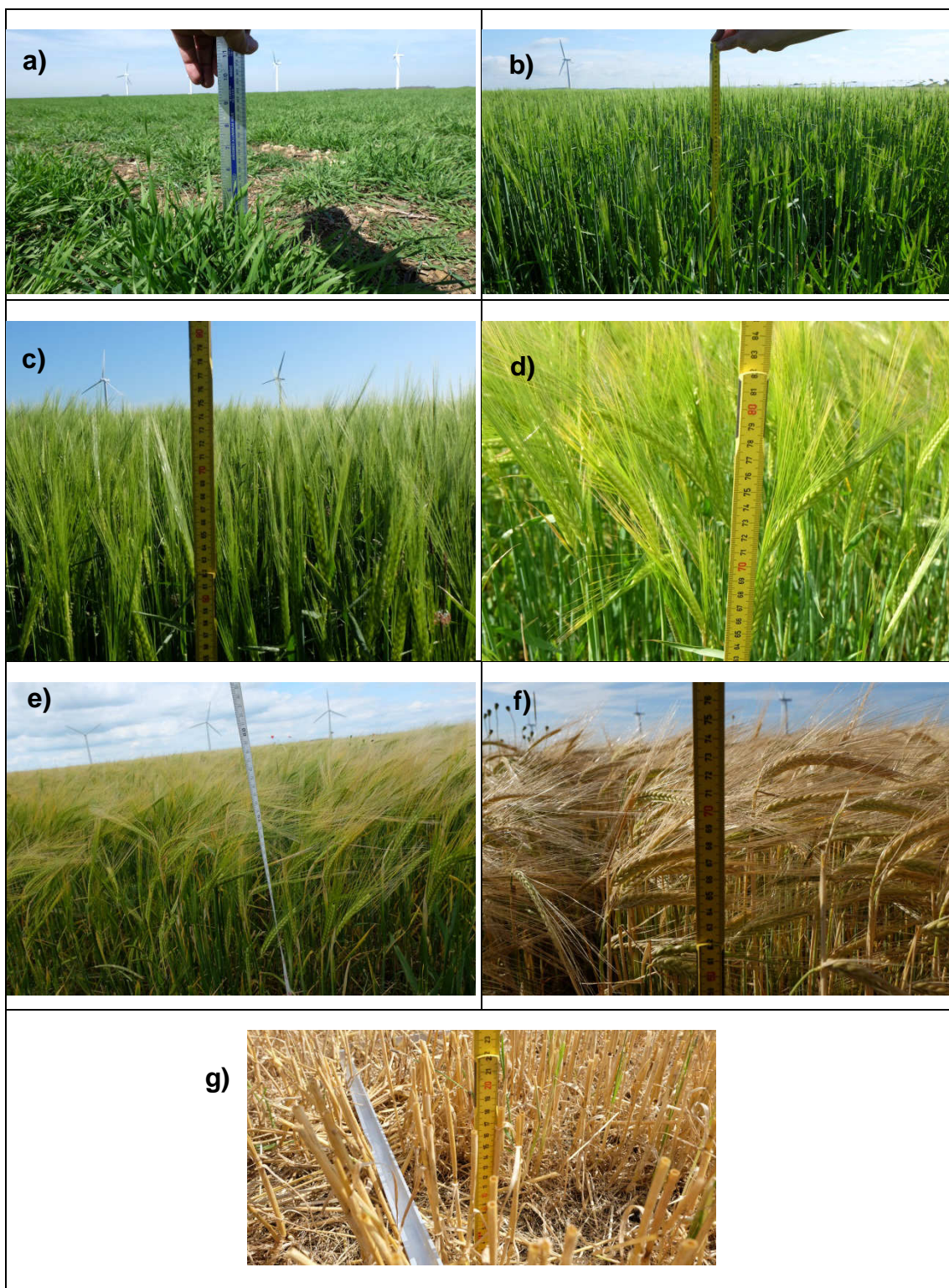
Figure 9-9: Crop heights (from soil to top): a) 15/04/2015 ~10 cm b) 27/05/2015 ~60 cm c) 04/06/2015 ~75 cm d) 15/06/2015 ~80 cm e)23/06/2015 ~73 cm f) 29/06/2015 ~73 cm g) 31/07/2015 ~20 cm.

Multiple photographs of the crops showing their size and shape have been taken. In addition, the sizes of the component parts of the plants were measured each day. Figure 9-10 shows a composite of photographs with the evolution of the plants through the campaign. To obtain a size reference in the photographs, the plants were placed on a paper grid of 1 cm.
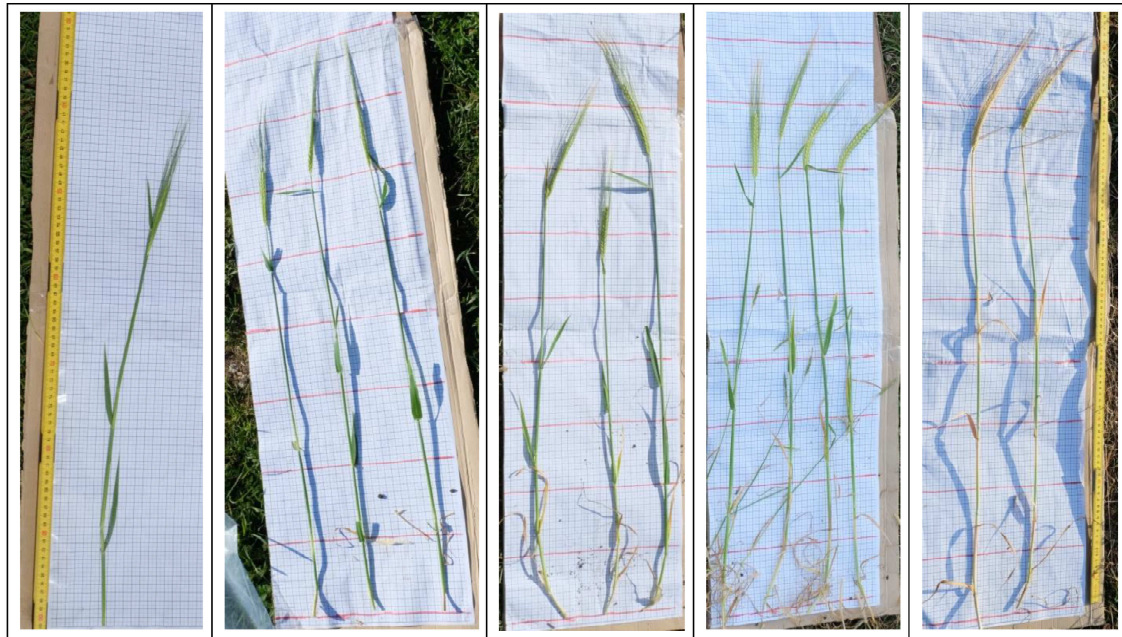
Figure 9-10: Crop shape on a 1 cm grid (pictures are not scaled) a) 27/05/2015 b) 04/06/2015 c) 15/06/2015 d) 23/06/2015 e) 29/06/2015.

When the plants were collected on the different days, noticeable differences in the size and shape of the plants have been found between them. These differences are also visible in Figure 9-10. During the growing period of the plants, while some plants presented a completely formed ear, some other plants presented a clearly shorter ear and size. These differences were also observed through the campaign with noticeable differences regarding the ear, leaf formation and size between individual plants. To see the dimensions of the plants, photographs were taken of at least 25 plants. The following Table 9-6 shows the mean sizes of at least 6 plants on the days measurements were performed.

	15-Apr	27-May	04-Jun	15-Jun	23-Jun	29-Jun	31-Jul
Stalk			57.3 / 4.1	61.6 / 6.3	64.3 / 6.4	70.0 / 4.9	
Stalk + Ear			65.6 / 4.9	71.7 / 7.1	74.4 / 6.0	78.9 / 7.9	
Total	~10	66.2 / 5.1	74.4 / 4.7	80.3 / 7.0	80.5 / 6.3	88.4 / 8.1	20
Soil to top part of the canopy	10	63	73	77	73	75	20

Table 9-6: Plant height (cm).
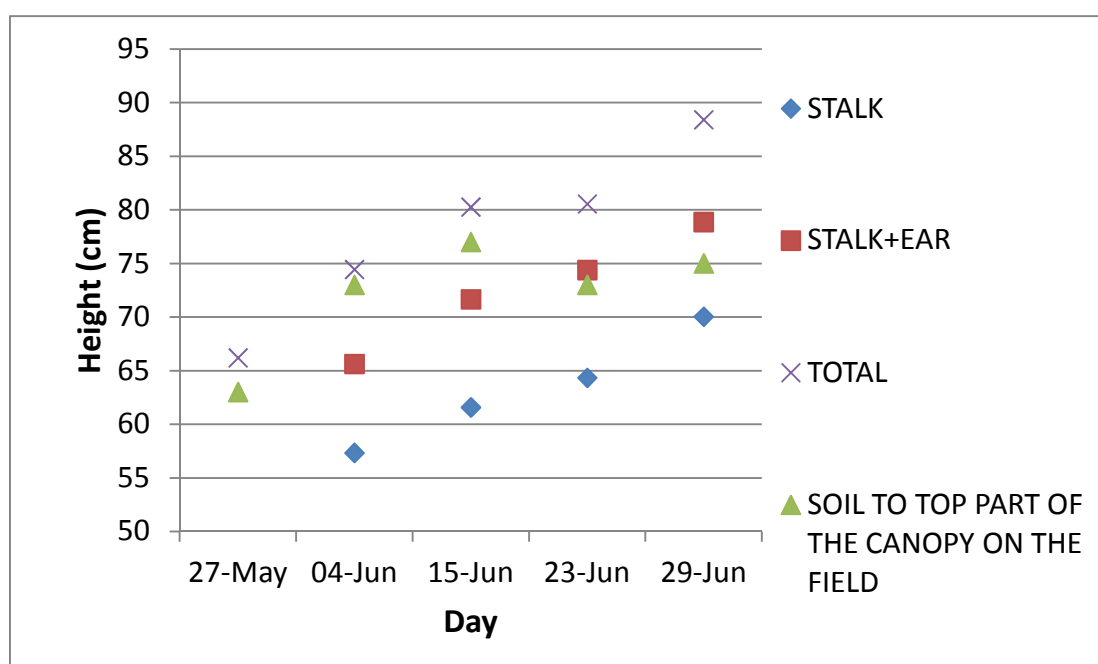
Figure 9-11: Height of the crops measured graph.

The graph in Figure 9-11 shows the height of the plants found on these days from the soil to the ear; the height of the stalk, the height of the stalk plus the ear, the total height of the plant and the height measured from the soil to the top of the plants on the field as shown in Figure 9-9. This division has been done according to the structure of the ear when it is mature, when it presents a distinguishable ear, some larger filaments around it and when the ears are bent depending on their ear formation (see Figure 9-8 and Figure 9-9). Figure 9-12 shows how the different sizes of the plants were measured. On every single day of the campaign, at least 25 plants were placed on a 1 cm grid and were

photographed to obtain the sizes of the different components of the plants. In this way, the mean values of the stalks, ears and the distance from the beginning of the ear to the end of the plant were calculated. This last value is bigger than the ear size because the barley presented some filaments on the ear longer than the ears (see Figure 9-11). Therefore, the *Stalk + Ear* value shown in Table 9-6 and Figure 9-11 represents the dimensions of the stalks plus the ear without these filaments, the *Total* values represents the size of the stalk plus the size from the ear to the end of these filaments and the *Soil to top part of the canopy* represents the values measured with a ruler as from the soil to the top part of the canopy as shown in the photographs shown in Figure 9-9.

Figure 9-12: Example of the length measurements of the components of the plants.

On the column for 27th of May, this graph only presents the value of the total height and the corresponding value measured from the soil to the top of the canopy on the field, this is because the ear wasn't formed yet at that time and in

the majority of the plants the ear was not completely visible, and in addition some of them did not present any ear at all.

Regarding the evolution of the ears, it is worth remarking that their maximum length was reached around the 15th of June, and that after that day the ears did not grow further in size, and started the process of drying. Regarding the evolution of the stalks, a linear growth can be observed in the data collected during the campaign.

Due the complexity and the differences between plants on the same day, it is difficult to obtain mean values of the height on the stalk of the leaves, widths of leaves or angles between the leaves and the stalk.

10 Analysis

In this chapter an analysis of the radar images taking into the account the stages of the plants growth, their biological parameters and soil presented when the measurements were performed is presented.

The analysis in this chapter has been divided in three parts. First, a study with the mean values within the crop canopy is presented. The Second part is a comparison between the first and the last days of the campaign (emerging of the plants and the field after harvesting) because the similarities of the plant height on both days. And a third part that includes the analysis of each day comparing the radar images showing the differences between them.

The next Table 10-1 and the Figure 10-1 shows the mean values obtained within the crop canopy. As it was expected, the VH polarization presents lower intensity values in both frequencies. With co-polarization (HH and VV), the intensity values within the canopy are almost, but with the HH polarization presenting slightly lower intensities than the VV polarization.

		X band			Ku band		
		VV	VH	HH	VV	VH	HH
Day (transect selected to calculate the mean)	15-Apr (165 to 190 cm)	-60.65	-67.99	-61.59	-64.47	-72.65	-67.45
	27-May (90 to 200 cm)	-66.10	-72.96	-68.23	-63.59	-72.66	-64.73
	04-Jun (90 to 200 cm)	-67.60	-74.59	-68.82	-67.40	-75.62	-70.01
	15-Jun (415 to 525 cm)	-81.64	-88.73	-82.25	-77.82	-87.01	-82.15
	23-Jun (275 to 375 cm)	-71.94	-78.49	-73.49	-70.73	-77.35	-72.75
	29-Jun (265 to 370cm)	-70.77	-77.92		-72.34	-79.79	
	31-Jul (325 to 360 cm)	-59.46	-73.90	-60.31			

Table 10-1: Mean values (dB) of the TP images calculated within the canopy of the crops.
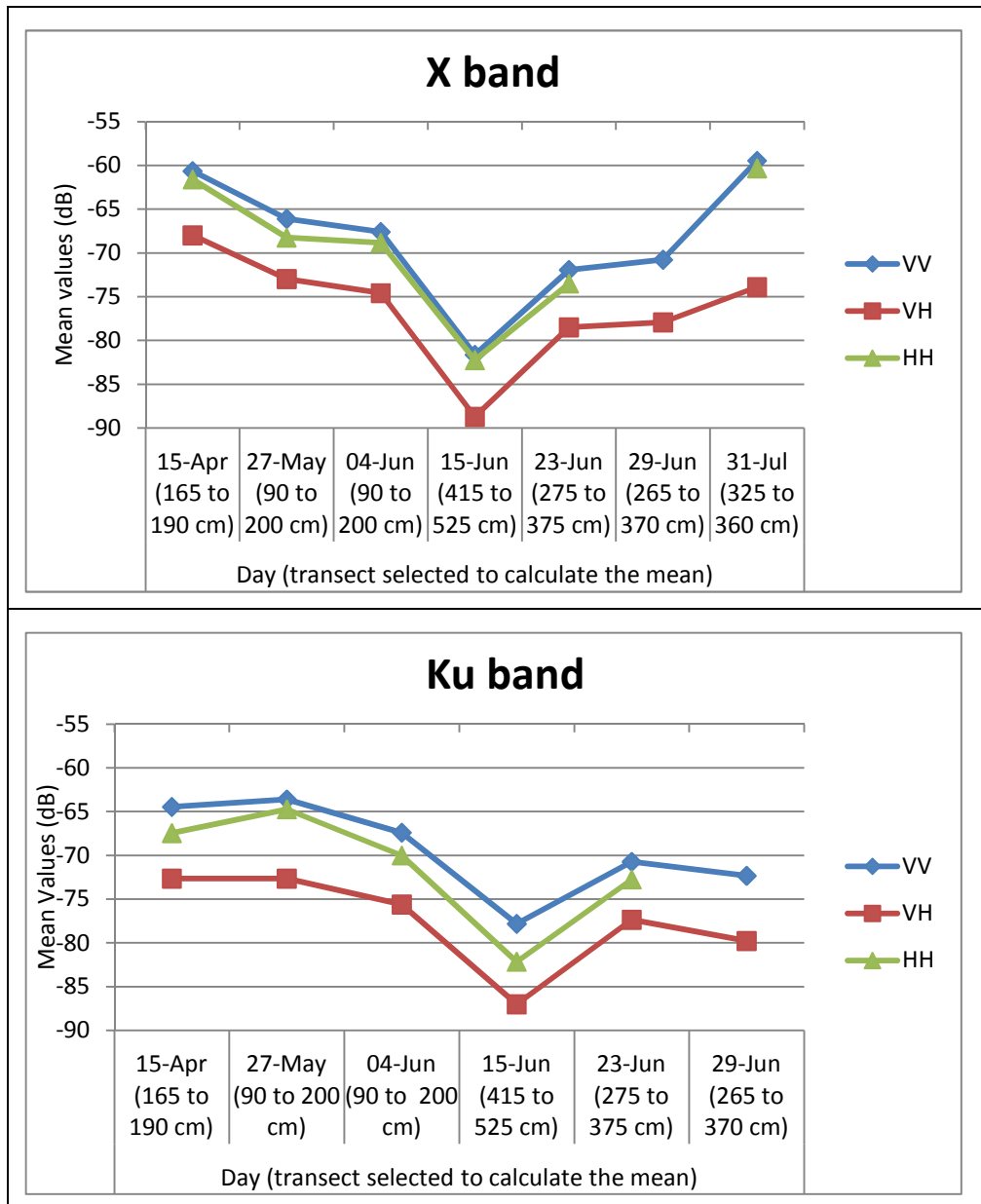
Figure 10-1: Graph with the mean values of the TP images calculated within the canopy of the crops.

Regarding the results obtained with X and Ku band with the same polarization on the different days, the maximum difference between the mean values between both frequencies is about 5.8 dB.

On the first day of the campaign, the barley on the field was young and it was similar to a grass field with a height of around 10 cm from the soil as shown in the Figure 8-9. The antennas were placed at around 1.75 m from the soil where a strong backscattered signal was returned to the antennas. About the

polarizations used to measure, the behaviour of the signals measuring the field is quite it is similar between VV and HH polarizations and for the case of cross-polarization measured; VH, the signal presents a weaker response with respect to co-polarization images. Due the short height of the plants presented on the first day; where the field was covered by grass with a height of around 10 cm as shown in the photograph of the Figure 8-9, and the last day of the campaign; when the field was harvested as shown in Figure 8-34, the main contributor of the backscattered signal from the field was the soil. The main contributor to the image comes from the soil as it can be seen in Figure 8-6, Figure 8-7, and Figure 8-32. The similarities between the backscattered signals measured these two days are also evident looking at the mean values extracted from the TP images (Figure 8-8 and Figure 8-33). The HH and VV polarizations present a similar shape with almost similar signal intensities peak due the soil; the cross-polarization measured, VH, presents a weaker answer respecting the co-polarization images.

The Figure 10-2 has been included in order to show how the comparison of the images has been performed in this analysis. It shows a composition comparing the size of the plants with an X band HH polarization TP image of the plants and with the mean values obtained by height of the three TP images with different polarizations (VV, HH and HV).
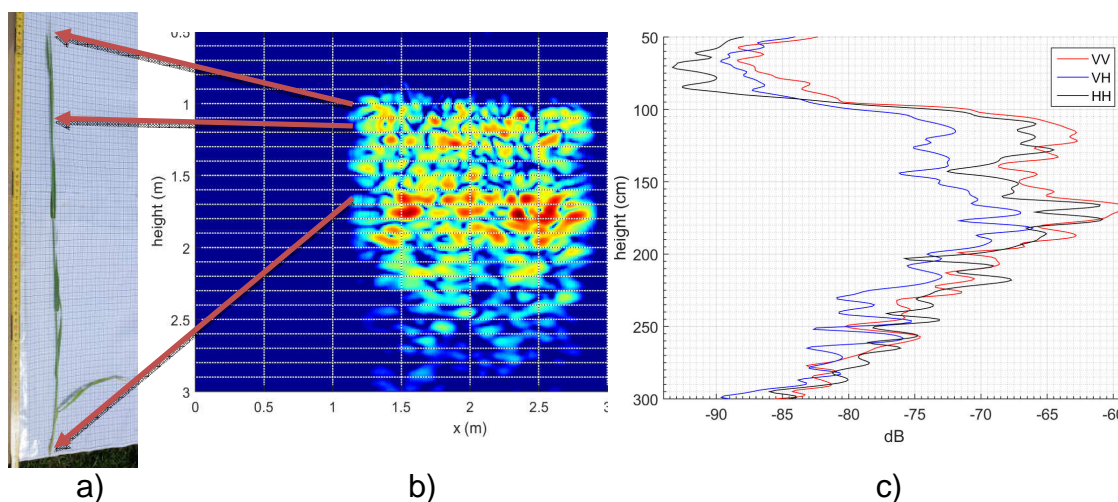
Figure 10-2: Composition of images a) Plant sample collected on the 27th of May. b) Tomographic profiling image – X band – HH pol. c) Average dB values by height.

On the 27 of May, the average plant height was of around 63 cm but the ear in most of the plants were not formed yet and it could be visible only a part of it. The X band TP images (Figure 8-11) show a uniform intensity levels within the canopy of the crops. Brighter spots can be seen at the height of the soil, where a bigger intensity is received on the backscattered signal. The antennas registered the soil and it can be distinguished as a brighter area on these images at around 1.7 m from the antennas. The crop in the VH polarization presents a dimmer intensity compared with the soil than in the VV and HH polarization images.

On the same day but looking at the VV and HH polarization Ku band TP images (Figure 8-12) taken, it can be seen that these images present a uniform intensity through the crops where the intensity level changes when the signal interacts with the soil. As it was mentioned on the previous paragraph, not all the ears appeared on this day and there is not any clear change of intensity between where the ears should be and the stalks. On the other hand, the soil on the Ku band TP image created presents a little bit more intensity creating a red line at the height that the soil was when the measurements were performed with these antennas.

Comparing the mean values calculated from these images (Figure 8-13), it can be seen that the magnitude of the signal and the shape in both frequencies of the VV an HH polarization is almost similar. Seeing the mean values of the VH polarization, it has smaller intensities compared with the other polarizations but the shape that the intensity presents through the canopy is quite similar. This behaviour it has been reproduced using both frequencies.

On the 4th of June of 2015, the antennas were placed almost at the same height from the soil as the previous day, 27th of May. The plants were a little bit higher than the day before and most of the ears emerged from the stalk. The average length from the start of the stalk to the end of the ear was 65.6 cm but the ears of the barley had some filaments that increase their length (Table 9-6). Regarding the X band TP images for this day (Figure 8-16), it can be seen that the intensity through the canopy is almost uniform with a stronger signal at the height of the crops and the soil. In the same way, the soil can be distinguished as the previous day as a brighter line around 1.7 m from the antennas. The HH TP image shows a non identified brighter point on the right side of the image at the same height of the soil if it is compared with the images generated with the rest of polarizations.

About the VV and HH Ku band images (Figure 8-17), the images present a brighter intensity around the ears and the soil. The VH polarization presents almost a uniform values trough the canopy until the signal meet the soil. In this case it cannot be observed any peak intensity around the ears of the plants.

Like the day before, the mean values graph for the 4th of June (Figure 8-18) shows almost the same shape and intensities for the HH and VV polarization with lower intensities for the VH case for both frequencies. The intensity for the VH Ku bands mean graph has the same intensity values through the canopy until the soil, where a peak on the intensity can be observed. For VV and HH polarization, at the height of the ear can be seen a bigger peak that loses intensity through the stalks until the soil, where there is another peak with almost the same intensity presented by the ears. These peaks are bigger compared with the ones measured using X band.

On the 15th of June the crane of the antennas was place at around 5.1 m from the soil. The images produced on this day present lower signal intensities but there is not any biological parameter that should indicate a clear drop on the intensity levels measured comparing the data collected with the rest of the days. In addition, due a non-identified problem during this day, the quality of some of these images is worse compared with other days; in particular the ones obtained with Ku band antennas. Some of them appear with more noise and in the worse case, the HH Ku band image it can be clearly observed a vertical bar where it should not appear any object. The height of the barley shown in the radar images is around 75 cm, almost the same as measured on the field (Table 9-6).

Looking at the X band TP images (Figure 8-20), the only polarization that presents brighter spots around the ears is the VH in contrast of the previous days. A line marked by a bigger intensity can be observed on the soil for the three different polarizations. For VV and HH polarizations, the intensity through the canopy in this band is almost uniform.

Comparing the mean values extracted from the TP images with X band (Figure 8-21), it can be seen a peak of intensity on the ear and soil for the HH. There is not any peak on the intensity due the ears with VV polarization, but this peak appears on the soil with bigger intensity than the rest of polarizations. Equal as the previous days, the VH polarization presents less intensity with peaks of the same intensity around the soil and ears.

On the 23rd of June, the boom of the GB-SAR was extended to half height placing the antennas around 3.5 m from the soil to proceed with the measurements. For the first time during the campaign, the X band TP images (Figure 8-24) present the brighter area around the ears of the crops for VV and HH polarizations. In the case of the VH polarization, the soil and the ears visually show almost the same intensity. In the middle of the stalks, around 3.3 m from the antennas, a small horizontal area seems dimmer than the volume correspondent to the ears and the soil. Due the increment of the weight of the ears, this one was the first day that the ears were totally bended forming almost

a 90º angle with the stalks as show Figure 10-3. The increment of weight and the position of the ears increase the intensity of the signal returned by them to the radar and it also made an apparent decrease of the height of the crops even when the crops were still growing. The near-horizontal orientation of the ears presented a defined layer on the top of the plants that it is visible on the radar images. Equal as the previous days, the backscattered signal from the soil is also visible. There is an obvious bifurcation of the scattering pattern due these two main contributors and the effect is more noticeable in the Ku band TP images.

Figure 10-3: Detail of the ears. The ears on the 23rd of June were bent almost 90º from the stalk.

Over the crops on the left part of the TP images, it can be seen a blurry area with less intensity than the crops. In this day some poppies were observed around the field and in the VV and HH polarization images they are clearly visible. These poppies could have been interpreted as noise in the VH polarization TP images if only this polarization would have been observed. The next Figure 10-4 shows a detail of the poppies with the area marked on a TP

image. These poppies are also visible in the TP Ku band images with VV and HH polarization but with less intensity than in the X band case.
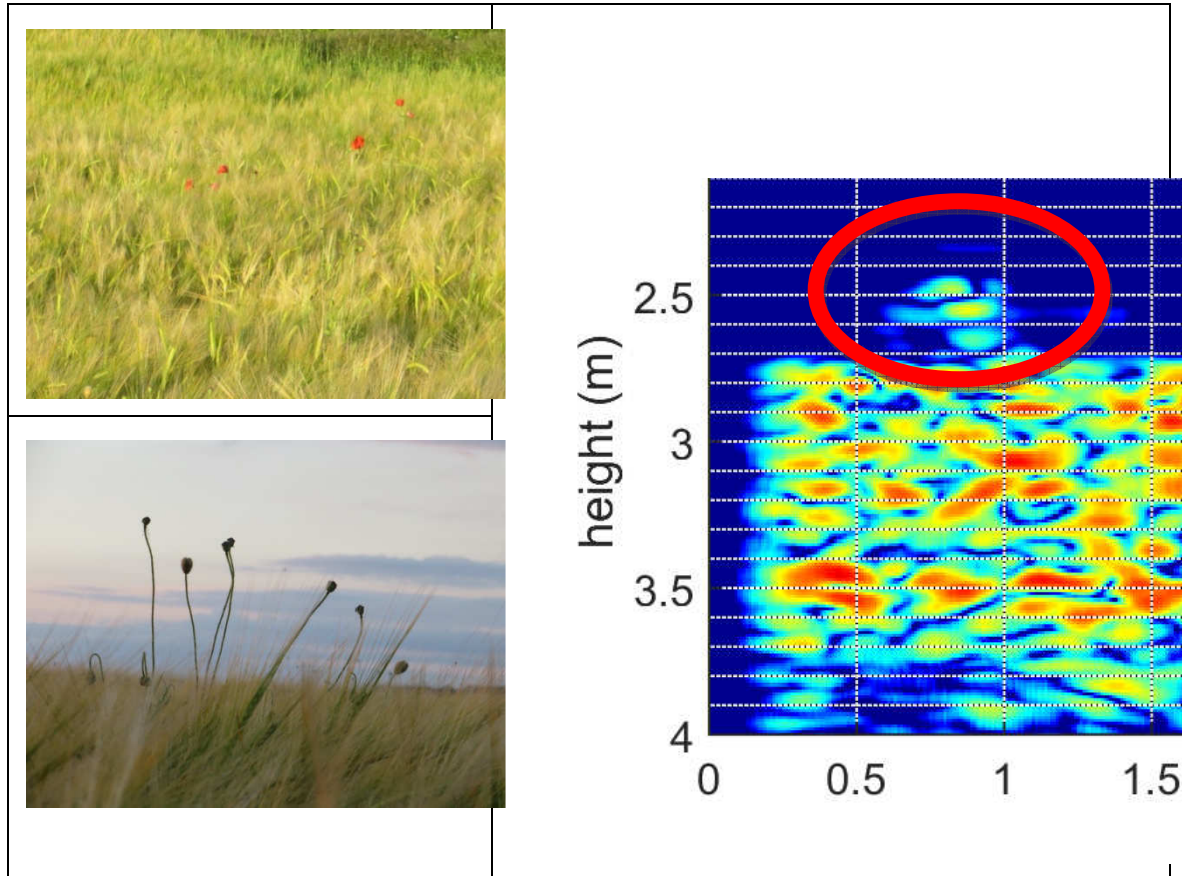
Figure 10-4: On the left, photos the poppies found on the field on the 23/06/2015. On the right, detail of the X band VV TP image with the poppies marked with a red circle.

In the case of Ku band TP images (Figure 8-25), the same effect is observed. In can be distinguished a brighter horizontal line due the crops and a dimmer area trough the canopy, corresponding with the volume occupied by the stalks, until the soil that can be differentiate from the crops.

As expected, the average backscattered signal intensity from the different polarizations show in the Figure 8-26 has similar shapes for all polarizations measured. For the case of the HH and VV polarization, they present almost the same intensity values and for the cross polarization, VH, the signal recorder is weaker than for the co-polarization cases.

Due a problem with the inclinometer of the GB-SAR on the 29th June, it was not possible to level the boom. This effect is visible on the TP images of this day, where it can be seen a difference of height of around 10 cm between the left and the right edges of the image. Only two polarizations were chosen this day to obtain the TP images, VV and HV. It can be also observed that the Ku images present noise and non desired horizontal bars on the images.

The TP images for this day; Figure 8-28 and Figure 8-29, show that the soil and the ears can be distinguished for both frequencies and both polarizations. The crop height on the images is around 75 cm as measured on the field. On this day, a bigger difference between the upper area of the crops and the middle part of crops in the Ku band images have been observed in comparison with the rest of the days.

11 Conclusions and future work

The temporal development of the radar signature of a barley canopy has been studied in this thesis through the growing season of the crop taking into the account the biological properties of the field on each day that the measurements were performed. Different TP images have been provided with all the biological parameters found on each day, seeing in this way the evolution of the crops during the growing season and comparing the results obtained with the biological parameters measured on the field. TP images shows that in an adult state, it is possible to distinguish the backscattering of ears from the stalks, and then from the soil return. In general and excluding the images from the 15th of June, there is a trend that shows that lower signal intensities would be found when the crops and soil presented a lower moisture levels.

A further study of the barley with the SAR images acquired in this campaign is proposed. It will be recommendable to study radar images over any other kind of crop and study its differences with the images acquired over barley. In order to perform a bigger study, it would be good to fix an automatic radar system on a field to measure every day or every few hours during the campaign. This

95

would be complemented by installing sensors around the field to measure the different biological parameters to perform a precise study of the radar images of the plants through the growing season of any crop. In this way it would be possible to compare precisely the images on consecutive days when minimum changes presented on the structure of the plants but with possible big changes on the moisture of the plants and soil due to precipitation.

Although not part of this thesis, it will be important to consider the results obtained from the TP study in relation to the SAR imagery that was obtained concomitantly by the GB-SAR system. SAR only presents a 2D representation of the 3D crop, and so provides no height information. However, this is still the primary method for retrieval of crop and soil parameters, so it is important to understand how the insight gleaned from the TP imagery can be applied to better utilize SAR imagery.

REFERENCES

[1]   E. Koenigher, A. Alakian, P. Borderies, A. Ginestet "SWINTOL: Survey of EM models", technical note of NOVELTIS NOV-7342-NT-4586 Issue. 0 –Rev. 1.

[2]   J.C. Bennett, K. Morrison, A.M. Race, G. Cookmartin, S. Quegan, "The UK NERC fully portable polarimetric ground-based synthetic aperture radar (GB-SAR)" Proceedings of International Geoscience and Remote Sensing Symposium, 2000 (IGARSS 2000), 24-28 July 2000, Vol. 5, pp. 2313 – 2315.

[3]   T. Le Toan, 'SAR image information content Scattering physics', Centre d'Etudes Spatiales de la Biosphère (CESBIO), Toulouse, France, 2005.

[4]   J. C. Curlander and R. N. McDonough, Synthetic Aperture Radar:Systems and Signal Processing. New York: Wiley, 1991.

[5]   Moreira, A.; Prats-Iraola, P.; Younis, M.; Krieger, G.; Hajnsek, I.; Papathanassiou, K.P., "A tutorial on synthetic aperture radar," Geoscience and Remote Sensing Magazine, IEEE , vol.1, no.1, pp.6,43, March 2013.

[6]   Ferretti, A., Monti Guarnieri, A., Prati, C., Rocca, F., Massonnet, D., February 2007. INSAR Principles: Guidelines for SAR Interferometry Processing and Interpretation. ESA Publications, TM-19.

[7]   Bamler, R., Hartl, P., Synthetic Aperture Radar Interferometry, Inverse Problems, vol.14, pp. R1-R54, 1998.

[8]   A. Reigber, R. Scheiber, M. Jäger, P. Prats-Iraola, I. Hajnsek, T. Jagdhuber, K. Papathanassiou, M. Nannini, E. Aguilera, S. Baumgartner, R. Horn, A. Nottensteiner, and A. Moreira, "Very-high-resolution airborne synthetic aperture radar imaging: Signal processing and applications," Proc. IEEE, vol. 101, no. 3, Mar. 2013.

[9]   Werninghaus, R.; Buckreuss, S., "The TerraSAR-X Mission and System Design," Geoscience and Remote Sensing, IEEE Transactions on , vol.48, no.2, pp.606,614, Feb. 2010.

[10] K Krieger, G.; Moreira, A.; Fiedler, H.; Hajnsek, I.; Werner, M.; Younis, M.; Zink, M., "TanDEM-X: A Satellite Formation for High-Resolution SAR

Interferometry," Geoscience and Remote Sensing, IEEE Transactions on, vol.45, no.11, pp.3317,3341, Nov. 2007.

[11] Torre, A.; Capece, P., "COSMO-SkyMed: The advanced SAR instrument," Recent Advances in Space Technologies (RAST), 2011 5th International Conference on , vol., no., pp.865,868, 9-11 June 2011.

[12] Snoeij, P.; Attema, E.; Davidson, M.; Floury, N.; Levrini, G.; Rosich, B.; Rommen, B., "Sentinel-1, the GMES radar mission," Radar Conference, 2008. RADAR '08. IEEE , vol., no., pp.1,5, 26-30 May 2008.

[13] Thompson, Alan A.; Luscombe, Anthony; James, Kenny; Fox, Peter, "RADARSAT-2 Mission Status: Capabilities Demonstrated and Image Quality Achieved," Synthetic Aperture Radar (EUSAR), 2008 7th European Conference on , vol., no., pp.1,4, 2-5 June 2008.

[14] Kankaku, Y.; Suzuki, S.; Osawa, Y., "ALOS-2 mission and development status," Geoscience and Remote Sensing Symposium (IGARSS), 2013 IEEE International , vol., no., pp.2396,2399, 21-26 July 2013.

[15] Arcioni, M.; Bensi, P.; Fehringer, M.; Fois, F.; Heliere, F.; Lin, C.-C.; Scipal, K., "The Biomass mission, status of the satellite system," Geoscience and Remote Sensing Symposium (IGARSS), 2014 IEEE International , vol., no., pp.1413,1416, 13-18 July 2014.

[16] Morrison, K.; Bennett, J., "Tomographic Profiling—A Technique for Multi-Incidence-Angle Retrieval of the Vertical SAR Backscattering Profiles of Biogeophysical Targets," Geoscience and Remote Sensing, IEEE Transactions on , vol.52, no.2, pp.1350,1355, Feb. 2014.

[17] Ulaby F.T., Elachi C., Radar Polarimetry for Geoscience Applications. Artech House,Norwood,MA,1990.

[18] Jester, W. & Klik, A. 2005. Soil surface roughness measurement - methods, applicability, and surface representation. Catena, 64, 174-192.

[19] Thomsen, L. M., Baartman, J. E. M., Barneveld, R. J., Starkloff, T., and Stolte, J.: Soil surface roughness: comparing old and new measuring methods and application in a soil erosion model, SOIL, 1, 399-410, doi:10.5194/soil-1-399-2015,2015.

[20] Snapir B, Hobbs S & Waine TW (2014) Roughness measurements over an agricultural soil surface with Structure from Motion, Isprs Journal of Photogrammetry and Remote Sensing, 96 210-223.

[21] S. C. M. Brown, S. Quegan, K. Morrison, J. C. Bennett and G. Cookmartin, "High resolution measurements of scattering in wheat canopies – implications for crop retrieval. IEEE Transactions of Geoscience and Remote Sensing, 41, p1602-1610 (2003).

[22] K. Morrison, J. C. Bennett, G. Cookmartin, A. J. McDonald, A. Race and S. Quegan "Three-dimensional X-band SAR imaging of a small conifer tree", Int. J. Remote Sens., 22, p705 (2001).

[23] J. C. V. Jakowatz, D. E. Wahl, P. H. Eichel, D. C. Ghiglia and P. A. Thompson. Spotlightmode synthetic aperture radar: A signal processing approach. Kluwer Academic Publishers, P. O. Box 17, 3300 AA Dordrecht, The Netherlands, 1996.

[24] A. Reigber and A. Moreira, "First demonstration of airborne SAR tomography using multibaseline L-band data," IEEE Trans.Geosci. Remote Sensing, vol. 38, no. 5, pp. 2142–2152, Sept. 2000.

[25] P. A. Rosen, S. Hensley, I. R. Joughin, F. K. Li, S. N. Madsen, E. Rodriguez, and R. M. Goldstein, "Synthetic aperture radar interferometry," Proc. IEEE, vol. 88, no. 3, pp. 333–382, Mar. 2000.

[26] Brown, S.C.M.; Quegan, S.; Morrison, K.; Bennett, J.C.; Cookmartin, G., "High-resolution measurements of scattering in wheat canopies-implications for crop parameter retrieval," in Geoscience and Remote Sensing, IEEE Transactions on , vol.41, no.7, pp.1602-1610, July 2003.

APPENDICES

[INTENTIONALLY BLANK AT THIS TIME]

[INTENTIONALLY BLANK AT THIS TIME]